Master Thesis

NO$_x$ Emissions Estimations of Swirl Stabilised Combustion using Chemical Reactor Networks.

AE 5211

S.E. Lubach

Delft University of Technology

Master Thesis

NO_x Emissions Estimations of Swirl Stabilised Combustion using Chemical Reactor Networks.

by

S.E. Lubach

Student Number: 4788095

Supervisor:	Prof. Dr. A. Gangoli Rao
Daily Supervisor:	ir. Turhan Eker
Project Duration:	November, 2024 - June, 2026
Faculty:	Faculty of Aerospace Engineering, Delft

Cover: Official KLM image of KLM 777-300ER Orange Pride.

TUDelft

Abstract

Hydrogen–hydrocarbon dual-fuel combustion offers a potential pathway towards hydrogen-powered aviation while reducing near-term CO_2 emissions. Methane–hydrogen combustion experiments were conducted at TU Delft to investigate this concept. Whilst CFD simulations can be used to analyse the combustor flow fields for different configurations, accurately estimating emissions of minor species, such as NO, is labour-intensive and computationally expensive. Therefore, in this thesis, Chemical Reactor Networks (CRN) are used to simulate the NO emissions of the experimental combustion setup. The CRN are created using a CFD-CRN programme that clusters CFD cells based on user-defined criteria, so they can be represented by a perfectly stirred reactor. Because only a single CFD solution for pure methane combustion was available, the resulting CRN were used to investigate both pure methane operation and the sensitivity of NO emissions to temperature, density, equivalence ratio, and hydrogen addition in the fuel stream. For pure methane combustion, the CRN predicted NO emissions of around 20 ppm, depending on CRN size and clustering approach. The predicted NO concentration was substantially closer to the experimental value of approximately 5 ppm than the 1000 ppm estimated by the CFD approach. The sensitivity studies predicted decreases in overall NO production for an increase in density, equivalence ratio, and hydrogen mole fraction. Increasing temperature resulted in higher NO emissions. Although the CRN did not reproduce the experimentally observed increase in NO emissions with hydrogen addition, the predictions of NO for pure methane combustion were promising, offering a foundation for future work.

Contents

List of Figures

List of Tables

Nomenclature

Acronyms

AAI	Axial Air Injection
AGNES	Automatic Generation of Networks for Emission Simulation
APPU	Advanced Propulsion and Power Unit
CFD	Computational Fluid Dynamics
CORSIA	Carbon Offsetting and Reduction Scheme for International Aviation
CRN	Chemical Reactor Networks
CV	Control Volume
GRI	Gas Research Institute
ICAO	International Civil Aviation Organization
LHV	Lower Heating Value
PFR	Plug-Flow Reactor
PLIF	Planar Laser-Induced Fluorescence
PSR	Perfectly Stirred Reactor
RANS	Reynolds-Averaged Navier–Stokes
SAF	Sustainable Aviation Fuels
TCI	Turbulence–Chemistry Interaction

Greek Symbols

ε	Residual Norm
μ_t	Turbulent viscosity
ρ	Density $[\mathrm{kg\,m^{-3}}]$
σ	Relative tolerance
φ	Equivalence ratio
$\dot{\omega}$	Species production rate $[\mathrm{mol\,s^{-1}\,m^{-3}}]$

Roman Symbols

A	Frequency factor [various]
b	Temperature exponent
C_p	Specific heat at constant pressure $[\mathrm{J\,kg^{-1}\,K^{-1}}]$
d	Diameter $[\mathrm{m}]$
E_A	Activation energy $[\mathrm{J\,mol^{-1}}]$
$\bar{f}$	Mean mixture fraction
h	Enthalpy $[\mathrm{J\,kg^{-1}}]$
k	Reaction rate coefficient [various]
L	Characteristic Length $[\mathrm{m}]$
l	Length $[\mathrm{m}]$
$\dot{m}$	Mass flow $[\mathrm{kg\,s^{-1}}]$
$\dot{m}'''$	Volumetric mass production $[\mathrm{kg\,s^{-1}\,m^{-3}}]$
MW	Molar weight $[\mathrm{kg\,mol^{-1}}]$
N_E	Number of equations
N_M	Number of measurements
N_P	Number of processes
N_R	Number of reactors
N_S	Number of species
P	Power $[\mathrm{W}]$
q	Clustering variable [various]
$\dot{Q}$	Heat transfer rate $[\mathrm{W}]$
R	Universal gas constant $[\mathrm{J\,mol^{-1}\,K^{-1}}]$
S	Surface Area $[\mathrm{m^2}]$
t	Time $[\mathrm{s}]$
T	Temperature $[\mathrm{K}]$
U_b	Bulk velocity $[\mathrm{m\,s^{-1}}]$
V	Volume $[\mathrm{m^3}]$
X	Mole fraction.
Y	Mass fraction

Super / Subscripts

act	Active Cluster
ad	Adiabatic
CC	Combustion chamber
i	Species index
in	Inlet value
ins	Inspected Cluster
MT	Mixing Tube
out	Outlet value

1

Introduction

An estimated 2.5% of the greenhouse gases emitted, stem from the aviation sector [1]. Despite increasing fuel efficiency, Airbus still forecasts a 2.1% increase in total fuel consumption per year [2]. If no additional mitigating steps are taken, it is estimated that aviation will contribute around $160\,\mathrm{mK}$ to global warming in 2100 [3]. That is 8% of the $2\,\mathrm{K}$ goal stipulated in the Paris Agreement [4]. The International Civil Aviation Organisation (ICAO) and the European Union (EU) have set their own ambitious goals to correct the path of the aviation sector [5, 6]. Namely, the Carbon Offsetting and Reduction Scheme for International Aviation (CORSIA) for ICAO and Flightpath 2050 for the EU.

Sustainable aviation fuels (SAF) will be essential for achieving the goals of the EU and ICAO. However, they are not suitable as a long term solution for carbon neutral aviation. This is because SAF only have a life cycle CO_2 reduction of 80% compared to kerosene [1]. A promising alternative fuel source is hydrogen. If produced renewably, its carbon free combustion would make it a carbon neutral fuel. Whilst promising, hydrogen combustion is not without its issues. One issue is its propensity for higher NO_x emissions, due to higher combustion temperatures. The production of green hydrogen and the accompanying infrastructure for its transport and storage are also not yet equipped to meet the demand of the aviation sector [7]. Dual-fuel combustion with hydrogen and a hydrocarbon is an attractive intermediate solution. It allows for a decrease in CO_2 emissions whilst incentivising the growth of green hydrogen production. Therefore, it is of interest to study not only the emissions of pure hydrogen combustion, but also the emissions in a dual-fuel configuration.

In Section 1.1, the dual-fuel combustion experiments performed at TU Delft are discussed. The numerical investigation of the experimental set-up forms the basis of this research. Common approaches for the numerical investigations of emissions are introduced in Section 1.2. Section 1.3 introduces an experiment that will be used to verify the correct working of the solver. An outline of the research is given in Section 1.4. Finally, an overview of the following chapters is given in Section 1.5.

1.1. Background

As part of the Advanced Propulsion and Power Unit (APPU) project, experiments with dual-fuel combustion technology were carried out at TU Delft using a swirler-stabilised combustor [8]. A schematic of the APPU combustor and the corresponding dimensions can be found in Figure 1.1 and Table 1.1, respectively. Here d_{CC} and d_{MT} are the diameters of the combustion chamber and mixing tube, respectively. Likewise, l_{CC} and l_{MT} are the lengths of the combustion chamber and mixing tube, respectively.

The combustor has two main air inlets in the mixing tube. One consists of four radially placed inlets that force the air through a swirler. The other inlet, aptly named axial air injection (AAI), bypasses the swirler entirely, allowing for an increased axial flow velocity when used. This is required for higher mole fractions of hydrogen due to its higher flame speed. Just aft of the swirler, the fuel mixture is introduced using four radial inlets. The fuel mixture can range from 100% CH_4 to 100% H_2. After the fuel injection, the flow is allowed to mix in the remainder of the mixing tube before entering the combustion chamber, resulting in partially premixed combustion.

Various operating conditions were tested during the experiments. The operating conditions could be varied by changing the swirl number of the swirler, varying the AAI flow, and adjusting the power of the flame. For a given operating condition, six different fuel compositions, see Table 1.2, were tested. The power of the flame and the air mass flow were kept constant for the different fuel mixtures. As a result, the adiabatic temperature, T_{ad}, and equivalence ratio, φ, decrease with an increase in hydrogen mole fraction, X_{H_2}, as shown for the $12\,\mathrm{kW}$ case in Table 1.2. Furthermore, due to the lower density of hydrogen, the bulk velocity, U_b, increases with increasing X_{H_2}. The emissions were measured at the end of the combustion chamber using a gas analyser, as shown in Figure 1.1. The other measurements were used to investigate the flow field and the flame shape. NO emissions were also investigated using planar laser-induced fluorescence (PLIF) [9].

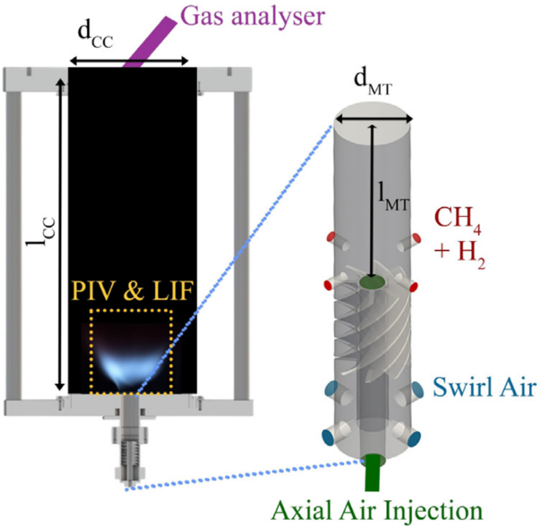

Figure 1.1: Schematic of the TU Delft swirler-stabilised combustor. [9]

Table 1.1: Dimensions mentioned in Figure 1.1.

d_{CC}	150 mm	l_{CC}	400 mm
d_{MT}	24 mm	l_{MT}	60 mm

Table 1.2: Design Points for P = 12 kW and $\dot{m}_{air}$ = 5.1 g s^{-1}

X_{CH_4}	X_{H_2}	U_b [m s^{-1}]	φ	T_{ad} [K]
1.0	0.00	10.45	0.75	1942
0.75	0.25	10.62	0.74	1930
0.60	0.40	10.75	0.73	1921
0.40	0.60	11.01	0.71	1908
0.20	0.80	11.44	0.68	1895
0.00	1.0	12.26	0.62	1858

1.2. Numerical Emissions Modelling

Since physical combustion experiments are a resource intensive endeavour, it is of interest to model combustion and investigate emissions numerically. A commonly used approach is to model combustion with the use of computational fluid dynamics (CFD). It has the advantage that it can model the fluid dynamics and the chemistry simultaneously. This allows it to model the effects of the flow on the chemistry and vice versa. However, that is also its largest drawback, computationally speaking. Typically, the chemical timescale is much smaller than the relevant timescale of the flow, resulting in very stiff systems of equations [10]. As a result, the modelling of detailed chemistry, required for accurate predictions of minor species such as NO_x, comes at a steep computational costs. To mitigate the computational costs associated with modelling chemistry in CFD, optimised models are used for the chemistry and the interaction between turbulence and chemistry. The chemistry models used often focus on the species most relevant to the fluid dynamics, meaning the species with non-negligible mass fractions, to reduce computational cost. As a result, minor species are often not modelled. While it is possible to model them, the set-up and computational costs of simulating minor species using CFD are significant.

A commonly used approach to model detailed emissions, including minor species such as NO, is through the use of chemical reactor networks (CRN). CRN consist of a collection of interlinked idealised control volumes (CV), represented by 0-dimensional reactors. The linked reactors can share mass and energy with one another, thus simulating flow from one CV to another. Using strong assumptions to simplify the physics and a chemical mechanism, see Section 2.1, reactors can estimate the temperature and the species concentrations in their CV. The advantage of using a CRN over a CFD approach for emissions modelling is that the chemistry is decoupled from the fluid dynamics. This allows for larger CVs and simpler equations. For the same domain, the number of equations is orders of magnitude smaller in a CRN than in a CFD simulation. This also allows for more complex reaction mechanisms to be used in a CRN. The computational cost of solving a CRN is much smaller than solving the flow and chemistry in CFD.

To achieve acceptable results using a CRN, the placement of the individual reactors is paramount. For proper placement, an understanding of the flow and physical properties in the domain is required. Hence, CRN are frequently constructed using CFD results of reacting flows. Since the detailed chemistry is done in the CRN, the CFD simulation can use a simple chemistry model for the major species. This approach assumes that the minor species have a negligible effect on the flow field. The most commonly used reactor type is the perfectly stirred reactor (PSR), see Section 2.3, but other reactor types, such as a plug-flow reactor (PFR) or partially-stirred reactor, can also be used.

CRN are frequently constructed based on CFD results. This is usually referred to as a CFD-CRN approach. It is also possible to construct a CRN without a CFD simulation, as is done in the component modelling approach. That approach is typically used in conceptual studies where the flow field is unknown. In the CFD-CRN approach, CFD cells that have similar properties can be grouped together (clustered) and represented by a reactor. In CFD-CRN mostly reacting flows are used to construct the CRN. This is because, in reacting flows, CFD models the effect of combustion on the flow field. Since the emissions are modelled in CRN, the CFD simulations can use reduced reaction mechanisms for only the large species [11]. The small species, such as NO_x, are assumed to have a negligible impact on the flow field. The assignment of CFD cells to a reactor can either be done manually or automatically, as discussed below.

In the manual CFD-CRN approach, the combustor is divided into zones based on the flow. An example of a manual approach used by Trespi et al. [12] can be seen in Figure 1.2. The figure shows the temperature profile and the streamlines of the oxy-fuel burner developed at TU Darmstadt. The streamlines, obtained from a CFD simulation, are used to divide the domain into zones. The zones A, D, E, and F are chosen to represent the individual recirculation zones present in the domain. Zone B was chosen to capture the flame front. Finally, zone C was chosen to capture the parallel streamlines that indicate quasi-one-dimensional flow.

A zone can be represented by one or more reactors in series, in parallel, or both. As discussed in Section 2.3, regions with high degrees of mixing, such as zone F, are represented by PSRs. Regions with (quasi-) one dimensional flow are best represented by a PFR. In the case of zone *D*, which exhibits both high mixing and one dimensional flow, Trespi et al. [12] elected to use a PSR and PFR in parallel. The temperature of the reactors can be taken as the average temperature of the region in the CFD simulation. Using temperatures from CFD results can significantly improve results compared to estimating the temperature in the CRN [13]. While Trespi et al. [12] use experimental values to determine the mass flow in the reactors, the mass flow is usually extracted from the CFD results, as was done by Chaturvedi et al. [14].

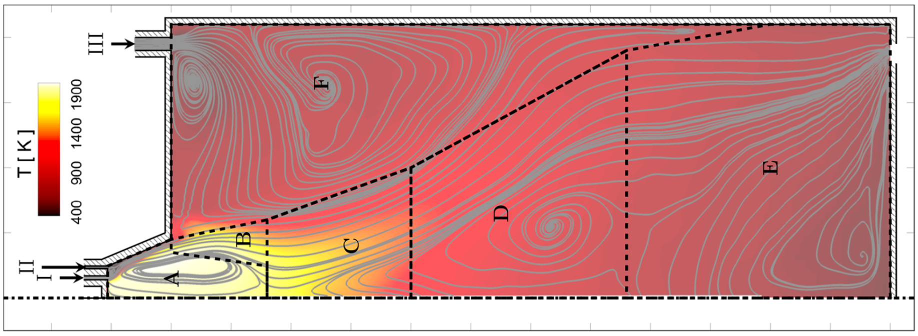

Figure 1.2: Example of manual zoning of a CFD simulation.[12]

In automatic CFD-CRN, the placement of the reactors is done by an algorithm. The grouping, or clustering, of similar CFD cells is done automatically based on user defined criteria. The temperature and mass flow of the reactors can also be automatically obtained from the CFD results. An advantage of this approach is the ability to place significantly more reactors than in the manual approach. It also simplifies changing the structure of the CRN compared to the manual approach. Usually, only PSRs are used in this approach.

An example of a CFD-CRN algorithm is given by Monaghan et al. [15] using Sandia Flame D, see Section 1.3, as a reference case. They divided the domain into zones using upper and lower bounds on axial locations, mixture fraction, and temperature. The zones are shown in Figure 1.3, with the colours indicating their mass-averaged temperature. Within these zones, the algorithm had zone specific clustering criteria for the cells, also based on temperature, mixture fraction, and axial location. These clustering criteria will be revisited in Chapter 4. The clustering of cells was done with user-defined functions in *Ansys Fluent* [16]. The CRN was solved using the kinetic post-processor (KPP) developed by Cuoci et al. [17].

An automatic CFD-CRN algorithm was also developed at Delft University of Technology. The Automatic Generation of Networks for Emission Simulation (AGNES) algorithm, written in *Python*, was initially developed by Sampat [18]. It was based on work that led to KPPSMOKE [19], the successor to the aforementioned KPP [17]. Sampat [18] initially created AGNES to study how clustering criteria

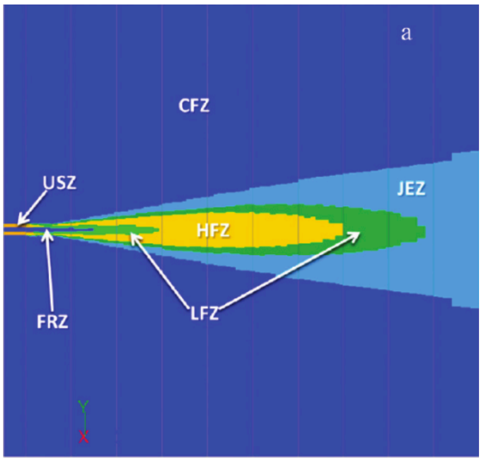

Figure 1.3: Zoning used by Monaghan et al. [15].

affected emissions predictions in CFD-CRN. Subsequently, De Wit [20] incorporated the heat equation into AGNES, which allowed the CRN to also solve for temperature. They investigated whether solving the heat equation improved the accuracy of the emissions results and how solving the heat equation affects computational cost. Lastly, Sutar [21] investigated the performance of different solver architectures. Both De Wit [20] and Sutar [21] also used Sandia Flame D as a reference case. The four sequential steps in the CFD-CRN algorithm: CFD output processing, clustering, generating the CRN, and solving the CRN are discussed in more detail in Chapter 3.

1.3. Sandia Flame D

The *Sandia Flames* are a series of experiments conducted on six different piloted jet flames burning methane and air [22]. The aim was to investigate the turbulent methane flame structure. As a result, the flames have the same methane air mixture at different Reynolds numbers. The flames are named A through F and are typically referred to by their letters. The experiment used various techniques to measure the mass fraction of both major and minor species, the mixture fraction, and the temperature. At multiple streamwise locations, radial measurements were taken, and the data for the turbulent flames (C,D,E,F) are readily available [23], making them popular reference cases for computational models. The simulations performed by Sutar [21] used Sandia Flame D as a reference case, citing its high Reynolds number and the availability of experimental data as the key reasons for its selection.

The geometry of the burner is shown from above in Figure 1.4 [23]. The burner exit was placed above a wind tunnel exit with a square cross-section and sides of $30\,\mathrm{cm}$. This wind tunnel provided a co-flow of air around the flame. Both the streamwise and radial data are given in coordinates relative to the inner diameter of the jet, d_{jet}. This can be seen in Table 1.3, which provides an overview of the available radial data for Sandia Flame D . Here, x is the streamwise coordinate and r is the radial coordinate. The number of measurements points for each radial profile is given by N_M.

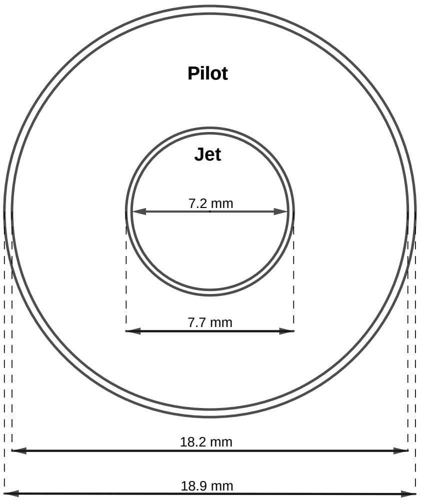

Figure 1.4: Top-down view of the geometry of the burner used for the Sandia Experiments.

Table 1.3: Overview of radial measurement data for Sandia Flame D.

x/d_{jet}	$(r/d_{jet})_{min}$	$(r/d_{jet})_{max}$	N_M
1	-0.6	1.9	19
2	-0.67	1.9	21
3	-0.74	2.18	20
7.5	-2.78	2.22	19
15	-0.56	3.06	15
30	-0.83	5.83	15
45	-1.11	7.78	14
60	-1.39	9.72	13
75	-1.39	11.11	12

1.4. Research Outline

In this research, an automatic CFD-CRN approach is used to investigate how the NO emissions of the APPU burner behave under different operating conditions. The CRN is based on a previously performed CFD simulation and is generated using AGNES. For this research, a new solver has been developed, the correct functioning of which is also verified in this work. The CRN are then modified to change individual operating conditions to isolate their effects on the NO emissions. The operating conditions of interest are the equivalence ratio, φ, the temperature, T, the density ρ, and the fuel composition. For the fuel composition, hydrogen is introduced into the fuel stream. Since experimental data on the emissions is available, the numerical results are compared to them, where possible. This leads to the research question and sub-question below.

How do variations in the operating conditions affect the NO emissions of the APPU burner?

1. What is the effect of the operating conditions on the NO pathways?
2. How does the introduction of hydrogen affect NO emissions?
3. How do the predicted NO emissions compare to experimental results?
4. How are NO trends affected by the clustering criteria?

1.5. Overview

In Chapter 2 the underlying theory of chemical reactor networks is discussed. Chapter 3 introduces the automatic CFD-CRN methodology, AGNES, used to study emissions. The verification of the current solver is performed in Chapter 4. The methodology used to investigate the APPU burner and the results of the baseline case are discussed in Chapter 5. Finally, the results of the sensitivity study are presented and discussed in Chapter 6.

2
Theory

This chapter presents the theoretical background required to understand the subsequent chapters. Section 2.1 introduces the concept of chemical kinetics, which forms the basis of numerical emissions modelling. Section 2.2 discusses the different pathways that can lead to NO formation. Section 2.3 introduces the mathematical model of a PSR, which is the foundation of the CRN approach discussed in Chapter 3.

2.1. Chemical Kinetics

Chemical kinetics is the foundation of numerical emissions modelling. Instead of considering the global reaction, chemical kinetics considers the intermediate reactions that convert the reactants into the products. The intermediate reactions are often referred to as elementary reactions. A collection of such elementary reactions that can be used to describe a global reaction is called a reaction mechanism. Subsection 2.1.1 discusses how elementary reactions can be used to model a reaction. Subsection 2.1.2 introduces the reaction mechanism that will be used.

2.1.1. Theory

An example of the aforementioned elementary reactions can be seen in Equation 2.1 [24]. The shown reactions are a subset of a reaction mechanism that describes hydrogen. An elementary reaction usually describes a collision between molecules, *bimolecular* or *termolecular*, but can also describe the disintegration of a molecule, *unimolecular*, as discussed in more detail below.

$$\begin{aligned} \mathrm{H_2 + O_2} &\rightleftharpoons \mathrm{HO_2 + H} \\ \mathrm{H + O_2} &\rightleftharpoons \mathrm{OH + O} \\ \mathrm{OH + H_2} &\rightleftharpoons \mathrm{H_2O + H} \\ \mathrm{H + O_2} &\rightleftharpoons \mathrm{HO_2 + M} \end{aligned} \tag{2.1}$$

As the name suggests, unimolecular reactions have one reactant species. There are two types of unimolecular elementary reactions, shown in Equation 2.2 and Equation 2.3. In the case of Equation 2.2, the reactant only changes its molecular structure. The reactant (A) and product (B) are thus isomers. The reactant can also decompose, as shown in Equation 2.3. At higher pressures, the reaction rate of A is given by Equation 2.4. Here, [A] is the molar concentration and k_{uni} is the first-order rate coefficient. At lower pressures, the reaction rate can become dependent on the molar concentration of another molecule M. The reaction rate is then given by Equation 2.5, where k_{bi} is the second-order rate coefficient. [24]

$$\mathrm{A \rightarrow B} \tag{2.2}$$

$$\mathrm{A \rightarrow B + C} \tag{2.3}$$

$$\frac{d[\mathrm{A}]}{dt} = -k_{uni}[\mathrm{A}] \tag{2.4}$$

$$\frac{d[\mathrm{A}]}{dt} = -k_{bi}[\mathrm{A}][\mathrm{M}] \tag{2.5}$$

Unsurprisingly, an elementary reaction with two reactants is referred to as a bimolecular reaction. The general form of a bimolecular reaction is shown in Equation 2.6. The reaction rate of species A is given by Equation 2.7. The same can also be done for species B. Again, k_{bi} is the second-order rate coefficient, and [A] and [B] are molar concentrations. [24]

$$\mathrm{A + B \rightarrow C + D} \tag{2.6}$$

$$\frac{d[\mathrm{A}]}{dt} = -k_{bi}[\mathrm{A}][\mathrm{B}] \tag{2.7}$$

Finally, reactions involving three reactant species are called termolecular. Equation 2.8 shows the generalised form of a termolecular reaction. Here, A and B are the main reactants, and C is the product. The molecule M is referred to as a third-body. It is a molecule of any kind that stabilises the reaction by absorbing energy from the newly formed C molecule during the collision. Without a third body present, C would decompose, making termolecular reactions the reverse of the unimolecular reaction shown in Equation 2.3. The reaction rate is given by Equation 2.9, where k_{ter} is the third-order reaction rate. [24]

$$\mathrm{A} + \mathrm{B} + \mathrm{M} \rightarrow \mathrm{C} + \mathrm{M} \tag{2.8}$$

$$\frac{d[\mathrm{A}]}{dt} = -k_{ter}[\mathrm{A}][\mathrm{B}][\mathrm{M}] \tag{2.9}$$

The first-, second-, and third-order reaction rates used in Equation 2.4, Equation 2.7, and Equation 2.9 can be found using the Arrhenius equation, shown in Equation 2.10. The equation uses experimentally determined values for the frequency factor, A, the activation energy, E_A, and the temperature exponent, b. Furthermore, it uses the universal gas constant, R, and the absolute temperature, T. Typically, the experimental values are only given for one direction of the reaction. The reverse rate is then calculated using the equilibrium constant, which relates the forward and reverse rates, as shown in Equation 2.11. For bimolecular reactions, the equilibrium constant can be calculated from the Gibbs free energy. [24]

$$k = A T^{(b)} e^{-E_A/RT} \tag{2.10}$$

$$\frac{k_f(T)}{k_r(T)} = K_{eq}(T) \tag{2.11}$$

The net production rate of a species can be calculated by considering all elementary reactions in the reaction mechanism that include said species as a product or reactant. The net production rate is found by adding the individual production rates of the elementary reactions given by Equation 2.4, Equation 2.7, or Equation 2.9. As shown in Equation 2.12 for the case of hydrogen radicals [24]. Here, the *f* and *r* subscripts denote the forward and reverse reaction rates, respectively. Analogous equations can be set up for all species found in the reaction mechanism. This set of differential equations can then be numerically solved in combination with the conservation laws. As a result, one can estimate incomplete combustion and emissions such as $\mathrm{NO_x}$.

$$\begin{aligned}\frac{d[\mathrm{H}]}{dt} =& k_{f1}\,[\mathrm{H_2}]\,[\mathrm{O_2}] + k_{r2}[\mathrm{OH}][\mathrm{O}] \\ &+ k_{f3}[\mathrm{OH}]\,[\mathrm{H_2}] + k_{r4}\,[\mathrm{HO_2}]\,[\mathrm{M}] + \ldots \\ &- k_{r1}\,[\mathrm{HO_2}]\,[\mathrm{H}] - k_{f2}[\mathrm{H}]\,[\mathrm{O_2}] \\ &- k_{r3}\,[\mathrm{H_2O}]\,[\mathrm{H}] - k_{f4}[\mathrm{H}]\,[\mathrm{O_2}]\,[\mathrm{M}] - \ldots\end{aligned} \tag{2.12}$$

2.1.2. GRI-Mech 3.0

The reaction mechanism that will be used is the Gas Research Institute mechanism, GRI-Mech 3.0 [25]. GRI-Mech 3.0 is specifically designed for methane combustion, unlike many other mechanisms that are generalised for small hydrocarbons. As a result, it consists of fewer elementary reactions, which is beneficial for computational resources. While smaller mechanisms exist, they usually do not include the $\mathrm{NO_x}$ chemistry, which is included in GRI-Mech 3.0.

While more modern mechanisms are available, such as the San Diego [26] and FFCM-I [27] mechanisms, GRI-Mech 3.0 is chosen due to its completeness. Unlike the other mechanisms, GRI-Mech 3.0 was optimised with both hydrogen and nitrogen oxide chemistry included. This makes it suitable for the emissions investigation of hydrogen-methane dual-fuel combustion. Furthermore, GRI methane mechanisms have been used extensively in literature, thus decreasing the likelihood of encountering novel issues.

2.2. Formation of NO_x

The production of NO can typically be attributed to a subset of the overall NO chemistry. These subsets, or mechanisms, are more or less relevant depending on the operating conditions of the combustion. The relevant operating conditions and the associated reactions of the different NO mechanisms are discussed in Subsection 2.2.1, Subsection 2.2.2, Subsection 2.2.3,Subsection 2.2.4. The formation of NO_2 is discussed in Subsection 2.2.5.

2.2.1. Thermal Mechanism

The thermal NO mechanism is the largest NO_x source in high-temperature combustion [28]. At lower combustion temperatures, its contributions are less significant, as the activation energy of the initial reaction, Equation 2.13, is relatively high [28]. Due to its high activation energy, Equation 2.13 is also the rate limiting step in the thermal mechanism. The initial reaction is also relatively slow. As a result, thermal NO production depends on the residence time and usually forms in the post-flame zone [29]. After the initial reaction, the nitrogen radical quickly oxidises by colliding with either hydroxide or oxygen, as shown in Equation 2.14 and Equation 2.15 [28].

$$\mathrm{O + N_2 \rightleftharpoons NO + N} \tag{2.13}$$

$$\mathrm{N + OH \rightleftharpoons NO + H} \tag{2.14}$$

$$\mathrm{N + O_2 \rightleftharpoons NO + O} \tag{2.15}$$

2.2.2. Prompt Mechanism

The prompt NO mechanism is an important NO_x source in hydrocarbon combustion. The mechanism describes NO_x that originates from collisions between N_2 and CH_n radicals. This means that prompt NO is more relevant in fuel-rich conditions and turbulent diffusion flames. These conditions increase incomplete combustion and thus the availability of CH_n radicals. Prompt NO is thought to have two important initial reactions, shown in Equation 2.16 and Equation 2.17, with Equation 2.16 being the main starting point. In lean and slightly rich conditions, the formed NCN radical usually follows the reaction sequence given by Equation 2.18, Equation 2.19, Equation 2.20, and Equation 2.21. It can also react with O, O_2, or OH and form NO directly or through subsequent reactions. [28]

$$\mathrm{CH + N_2 \rightleftharpoons NCN + H} \tag{2.16}$$

$$\mathrm{C + N_2 + M \rightleftharpoons NCN + M} \tag{2.17}$$

$$\mathrm{NCN + H \rightleftharpoons HCN + N} \tag{2.18}$$

$$\mathrm{HCN + O \rightleftharpoons NCO + H} \tag{2.19}$$

$$\mathrm{NCO + H \rightleftharpoons NH + CO} \tag{2.20}$$

$$\mathrm{NH + H \rightleftharpoons N + H_2} \tag{2.21}$$

2.2.3. N_2O Mechanism

The N_2O mechanism is thought to be relevant in high pressure, moderate temperature, lean conditions. The initial step is shown in Equation 2.22. The N_2O can then react with H or O as shown in Equation 2.23 and Equation 2.24, respectively. In the case of Equation 2.23, the NH radical can also further react to form NO. [28]

$$\mathrm{O + N_2 + M \rightleftharpoons N_2O + M} \tag{2.22}$$

$$\mathrm{N_2O + H \rightleftharpoons NO + NH} \tag{2.23}$$

$$\mathrm{N_2O + O \rightleftharpoons 2NO} \tag{2.24}$$

2.2.4. NNH Mechanism

The NNH mechanism can be relevant at elevated temperatures and slightly fuel rich conditions. The initial step is shown in Equation 2.25. The formed NNH can then react as shown in Equation 2.26. The formed NH can then also react as previously shown in Equation 2.21. [28]

$$\mathrm{H + N_2 + M \rightleftharpoons NNH + M} \tag{2.25}$$

$$\mathrm{NNH + O \rightleftharpoons NO + NH} \tag{2.26}$$

2.2.5. Formation of NO_2

The NO formed through the discussed mechanisms usually forms NO_2 in the atmosphere. However, NO_2 can also form within the combustion environment through Equation 2.27. This reaction typically occurs in colder combustion regions, since HO_2 forms at temperatures lower than combustion temperatures. Furthermore, NO_2 usually forms NO at higher temperatures through Equation 2.28 and Equation 2.29. Therefore, NO_2 is only formed in lower-temperature regions within the combustor. [24]

$$\mathrm{NO} + \mathrm{HO_2} \rightleftharpoons \mathrm{NO_2} + \mathrm{OH} \tag{2.27}$$

$$\mathrm{NO_2} + \mathrm{H} \rightleftharpoons \mathrm{NO} + \mathrm{OH} \tag{2.28}$$

$$\mathrm{NO_2} + \mathrm{O} \rightleftharpoons \mathrm{NO} + \mathrm{O_2} \tag{2.29}$$

2.3. Perfectly Stirred Reactor

A PSR assumes that the CV is homogeneous. This assumption is applicable when the Damköhler number is very small [30]. The Damköhler number, shown in Equation 2.30, relates the chemical timescale to the flow timescale. The governing equations of a PSR are also assumed to be in steady-state. Thus, for a species i in the CV, the conservation of mass can be formulated as shown in Equation 2.31. Where $\dot{m}$ are the mass flows entering and leaving the CV, $\dot{m}'''$ is the volumetric mass production, and V is the volume of the CV. [24]

$$\mathrm{Da} = \frac{\tau_{flow}}{\tau_{chem}} \tag{2.30}$$

$$\dot{m}_{i,\,out} = \dot{m}_{i,\,in} + \dot{m}_i'''V \tag{2.31}$$

The volumetric mass production is defined as shown in Equation 2.32. It captures the net mass production of the species inside the CV. As shown in Equation 2.32, it is the product of the production rate ($\dot{\omega}$) and the molecular weight (MW) of the species. As discussed in Section 2.1, $\dot{\omega}$ is a function of the temperature of the CV through Equation 2.10 and mass fraction of the species in question through Equation 2.12. It should be noted that $Y_{i,\,out}$ is just the mass fraction of the species in the CV, since the CV is assumed to be perfectly stirred. Assuming no diffusional flux, the mass flow of a species is simply the product of its mass fraction and the total mass flow entering or leaving the CV. Using Equation 2.32, Equation 2.31 can be rewritten as shown in Equation 2.33

$$\dot{m}_i''' = \dot{\omega}_i(Y_{i,\,out}\,,\, T) \cdot MW_i \tag{2.32}$$

$$\dot{\omega}_i\, MW_i\, V + \dot{m} \cdot (Y_{i,\,in} - Y_{i,\,out}) = 0 \tag{2.33}$$

The temperature of the CV is often taken from CFD results. If that is not possible or desirable, using Equation 2.33 leads to an underdetermined system of equations. For N species, there will N+1 variables. To remedy this, the conservation of energy equation, see Equation 2.34, is used. With h_i being the enthalpy of the species and $\dot{Q}$ being the heat transfer into the CV. The heat transfer can come from other reactors through mass exchange or from the walls of the reactor.

$$\dot{Q} = \dot{m} \cdot \left(\sum_{i=1}^{\mathrm{N}} Y_{i,\,out}\, h_i(T) - \sum_{i=1}^{\mathrm{N}} Y_{i,\,in}\, h_i(T_{in})\right) \tag{2.34}$$

3

CFD-CRN Algorithm

This chapter discusses how the CRNs used in subsequent chapters are generated from a CFD solution and how they are solved. Section 3.1 discusses the generation of the CRN and Section 3.2 discusses the solving approach.

3.1. CRN Generation (AGNES)

In this section, the generation of CRN in AGNES is discussed. The approach to generate CRN in AGNES has largely remained the same as in the original version of Sampat [18]. Small alterations have been made, as discussed below. Subsection 3.1.1 describes how the CFD mesh solution data are used. Subsection 3.1.2 discusses how cells are clustered into control volumes that can be used as PSRs. Subsection 3.1.3 explains how the formed CVs are transformed into PSRs.

3.1.1. CFD Data

Currently, AGNES can only generate CRNs from *Ansys Fluent* case and data files. However, there is no inherent incompatibility with CFD results in other formats, aside from the parsing of the files, as long as the required information discussed below can be provided. The case file contains information on the mesh, such as the coordinates of the nodes and the composition of faces. Nodes are essentially vertices, and faces are the lines or planes connecting the nodes. The data file contains the solution data, the final state of cells and faces, from the CFD simulation. The format of the case and data file can be found in the *Ansys Fluent User's Guide* [31].

In order to cluster cells and generate a CRN from those clusters, cells are structured in the following way. A cell contains the IDs of adjacent cells, the IDs of the faces and nodes that define the cell, the zone in which the cell is located, and the cell ID itself. With Cell IDs simply being unique identifiers. Aside from the cell zone, all the required information for the cells is found in the definition of the faces. In the case file, each face is defined by the nodes that define its shape and the cells that use that face. This information is used to determine the connectivity of the cells and to identify which nodes and faces define a cell. In addition to the cell information, the types of boundary conditions applied to the faces are also required for the generation of the CRN.

3.1.2. Clustering

The initial step in clustering is converting all the CFD cells into clusters containing one cell. In practice, this step is mostly semantic since clusters and cells are defined in the same way. A cluster contains the IDs of adjacent clusters, the IDs of the faces and nodes that define the cluster, and the IDs of the cells that are in the cluster. The clustering of the individual clusters is performed using a Breadth First Search [32] approach, which makes use of the information on adjacent clusters. The aim of the algorithm is to reduce the number of clusters from the number of cells in the CFD mesh to the desired number of reactors, N_R. It is run for every iteration of the clustering process.

A flowchart of the clustering algorithm can be seen in Figure 3.1. It starts by choosing an arbitrary starting cluster and adding its adjacent cells (neighbours) to a queue. The starting cluster is now the active cluster, and the algorithm inspects a cluster from the queue. The neighbours from the inspected cluster are then also added to the queue if they have not been added previously. This approach makes it likely that the active and inspected clusters lie close to each other. This increases the probability that the active and inspected cluster have similar physical properties, increasing the likelihood of clustering. It also ensures that every cluster in the domain is visited during an iteration. However, this approach can also lead to encounters between non-adjacent clusters.

As a result, active and inspected clusters are subjected to a fitness check. In the fitness check, the geometrical connection of the clusters is verified, and the user defined clustering criteria are applied. If an inspected cluster fails the fitness check, it becomes the new active cluster. The former active

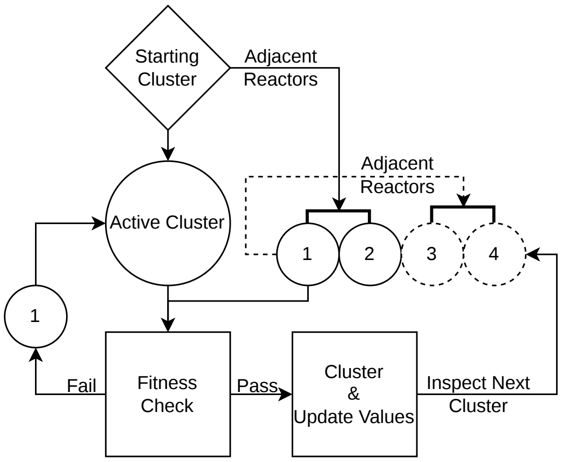

Figure 3.1: A flow chart of a single iteration of the clustering algorithm.

cluster is idle until the next iteration. If the neighbour passes the fitness check, the active cluster and the inspected cluster are clustered together. This entails adding their individual volumes together and mass averaging their physical properties where appropriate. The temperature, for example, is not mass averaged but is calculated to conserve enthalpy. The faces of the clusters are also combined, except for the faces they shared, since these faces are now in the interior of the cluster. Finally, the interconnectivity of the cluster is updated. The new cluster remains the active cluster.

3.1.3. CRN Generation

The generation of the CRN is the conversion of the clusters into interconnected PSRs. There are three main steps that need to be taken. Namely, quantifying the interconnectivity of the reactor through mass flows, identifying reactors with boundary conditions, and performing a mass flow correction. These steps are discussed in more detail below. It should be noted that the clusters from Subsection 3.1.2 are referred to as reactors below.

Mass Flows

The interconnectivity of the reactors is described using a matrix of size N_R *x* N_R. An example of such a matrix is shown in Equation 3.1. The O_r on the diagonal of the matrix represents the total mass outflow of the reactor. The $-\mathrm{I}_{\mathrm{a}\leftarrow\mathrm{b}}$ represents the mass flow from reactor b into reactor a. The mass flows are calculated using CFD data for the cell faces. They can be calculated from the mass flux passing through the faces that make up the boundary of the reactor. When two reactors share a face, the mass flux through that face is added to the mass flow exchange between the reactors. Depending on the direction of the mass flux, it is either added to $-\mathrm{I}_{\mathrm{a}\leftarrow\mathrm{b}}$ and O_b or to $-\mathrm{I}_{\mathrm{b}\leftarrow\mathrm{a}}$ and O_a.

$$\mathbf{C} = \begin{bmatrix} \mathrm{O}_1 & \cdots & -\mathrm{I}_{1\leftarrow\mathrm{N_R}} \\ \vdots & \ddots & \vdots \\ -\mathrm{I}_{\mathrm{N_R}\leftarrow 1} & \cdots & \mathrm{O}_{\mathrm{N_R}} \end{bmatrix} \tag{3.1}$$

In addition to the mass flows calculated from the CFD data, De Wit [20] also added an optional model for turbulent diffusive mass flows between reactors. They argued that the absence of recirculation zones in Sandia Flame D means that turbulent diffusion contributes significantly to species mixing. The mass flow due to turbulent diffusion is calculated using Equation 3.2. It is derived from Equation 3.3 and Equation 3.4, definitions of the Peclet and Schmidt numbers, respectively. Here, μ_t is the turbulent viscosity, $\mathrm{D}_{\mathrm{m,t}}$ is the turbulent mass diffusivity, and L is a characteristic length. The value for the Schmidt number is assumed to be 0.7. The characteristic length is taken to be the cube root of the reactor. The surface area S refers to the area of the face that connects the two reactors. The additional mass flow due to turbulent diffusivity is added to Equation 3.1.

$$\dot{m}_{diff,\,t} = \frac{S\,\mu_t}{L\,\mathrm{Sc}} \tag{3.2}$$

$$\mathrm{Pe} = \frac{\dot{m}_{\mathrm{adv}}}{\dot{m}_{diff,\,t}} = \frac{v\,L}{D_{m,\,t}} \tag{3.3}$$

$$\mathrm{Sc} = \frac{\mu_t}{\rho\,D_{m,\,t}} \tag{3.4}$$

Boundary Conditions

The boundary conditions from the CFD simulation also have to be applied to the relevant reactors in the CRN. In the CFD mesh, the boundary conditions are applied to the faces of the cells. Thus, by cross-referencing the faces of a reactor with the indices of the boundary condition faces, the required boundary conditions for a reactor can be found. The three boundary conditions of interest for the current work are the inlet, outlet, and periodic boundary conditions. These boundary conditions are all based on mass flows. Again, the mass flows to or from a reactor can be calculated from the mass flux through the relevant faces. The compositions of the gases flowing through the boundary faces are set by the user at a later stage.

The mass flows from inlet boundary conditions are stored in a vector of size N_R, as shown in Equation 3.5. The value for f_r is zero if a reactor is not connected to an inlet. If a reactor is attached to an outlet, the mass flow is added to the diagonal term in Equation 3.1. Finally, the periodic mass flow is also tracked in Equation 3.1. It is handled as normal mass flow from reactor *b* into reactor *a* or vice versa. An exception to this is when the periodic mass flow is circular. Due to the clustering of the cells, it can occur that both the periodic face and the periodic shadow face are part of the same reactor. This can cause issues with the mass flow correction, discussed below. Therefore, circular periodic flow is also stored in a vector, as shown in Equation 3.6.

$$\vec{f} = \begin{bmatrix} \dot{m}_1 \\ \vdots \\ \dot{m}_{N_R} \end{bmatrix} \tag{3.5}$$

$$\vec{o} = \begin{bmatrix} \dot{m}_1 \\ \vdots \\ \dot{m}_{N_R} \end{bmatrix} \tag{3.6}$$

Mass Flow Correction

The mass flow correction is a necessary step due to tolerances in the conservation of mass in CFD cells. These tolerances accumulate during clustering and can lead to significant mass flow imbalances. The mass flow correction is performed after the mass flow matrix from Equation 3.1 is complete, including the boundary conditions. It uses the underlying principle that, in general, the net mass flow of a reactor should be zero. This means that the mass outflow of a reactor should be equal to the mass inflow from its neighbouring reactors. The exceptions to this are if a reactor is connected to an inlet or if it has circular periodic flow. In this case, the net mass flow is equal to the mass flow from the inlet plus the circular mass flow. This yields Equation 3.7, where $\vec{x}$ is a vector containing the mass outflows of the reactors. The matrix **A**, shown in Equation 3.8, is created by dividing the columns of matrix **C** by the diagonal value in the column. This turns the mass flows in Equation 3.1 into coefficients of the mass outflows of the reactors. With the solution $\vec{x}$ and the coefficient matrix **A**, a new mass flow matrix **C** can be created.

$$\mathbf{A}\vec{x} = \vec{f} + \vec{o} \tag{3.7}$$

$$\mathbf{A} = \begin{bmatrix} 1 & \cdots & -c_{1\leftarrow N_R} \\ \vdots & \ddots & \vdots \\ -c_{N_R\leftarrow 1} & \cdots & 1 \end{bmatrix} \tag{3.8}$$

3.2. CRN Solver

Attempts to use the solver architectures employed by Sampat [18], De Wit [20], and Sutar [21] were unsuccessful. Therefore, a new solver architecture had to be developed. The current solver is based on the work of Cuoci et al. [17]. The current solver is not able to solve for temperature, which was possible with the solver developed by De Wit [20]. In Subsection 3.2.1, the architecture of the current solver is discussed. The objective function that the solver minimises is introduced in Subsection 3.2.2. The solving strategy used to minimise the objective function is discussed in Subsection 3.2.3.

3.2.1. Solver Overview

A schematic of the solver architecture is shown in Figure 3.2. The schematic shows the required inputs for the solver and the different steps in the solving process. The solver uses the reactors that are created based on the clustering and the mass flow matrix described in Section 3.1. It also requires the reaction mechanism and the boundary conditions of the system. The reaction mechanism can be freely chosen by the user, as long as the format is compatible with the *Cantera IdealGasReactor*, discussed below. The boundary conditions are also user defined. While the mass flows into the domain are determined from the CFD mesh, as discussed in Equation 3.1.3, the composition of the inflowing mass is set by the user.

The aforementioned *IdealGasReactor* from the *Cantera* [33] library handles the chemistry aspect of the solver. It describes a CV using volume, temperature, density, and mass fractions of species. These properties are taken from the CFD results. As the name suggests, it assumes an ideal gas. As such, other ideal gas properties, besides the ones mentioned, can also be used to describe the CV. By inserting a *Cantera Solution* object into the reactor, a *ThermoPhase* object is created that represents the gas as an ideal gas. Furthermore, a *Kinetics* object is created that handles the chemical kinetics as described in Section 2.1. It is used to compute the net production rates and the forward and reverse production rates during the solving process. It does this in accordance with the user defined reaction mechanism.

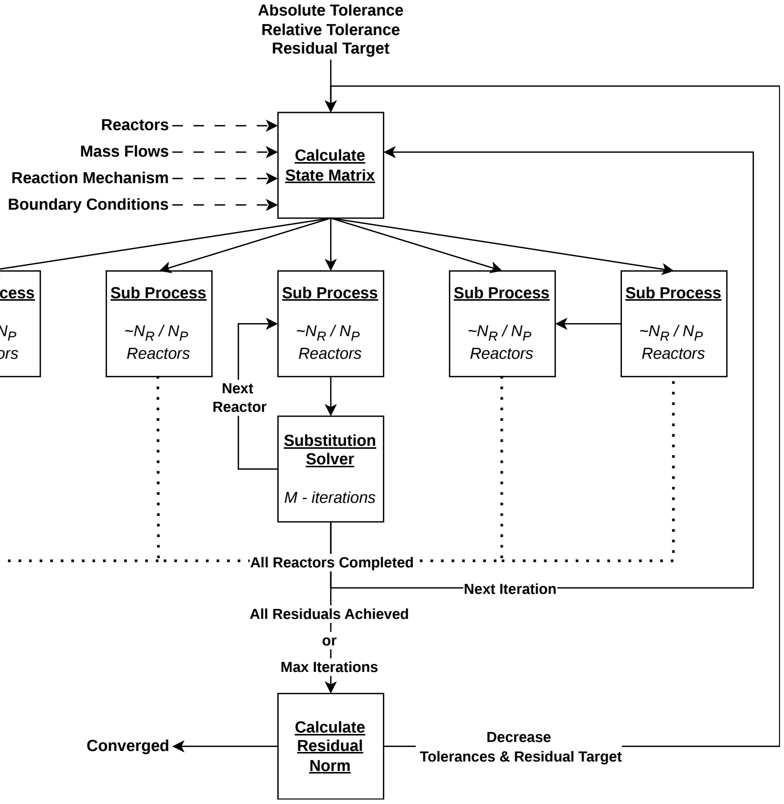

Figure 3.2: Schematic of the current solver architecture employed.

The first step of the solver is to cast the gas compositions of the reactors into a state matrix of shape $N_R \times N_S$, the number of reactors and species, respectively. The reactors are then divided evenly, if possible, amongst the user defined number of parallel processes. In each sub-process, a single *Cantera IdealGasReactor* object is created. The N_R/N_P reactors in a sub-process are iterated through sequentially as follows. First, the state of the reactor is transferred to the *IdealGasReactor* object. Then, the initial residual of the reactor is checked. Here, the residual refers to the L1 norm of the residuals obtained from the objective function. If the residual is larger than the target residual, the substitution solver is used. Otherwise, the next reactor is loaded. The substitution solver either completes its iterations or terminates early if the desired residual is achieved. When all reactors have been iterated through, it is checked whether they have all achieved the target residual. If not, the next iteration is started.

If all reactors have converged sufficiently, or if the solver has reached its maximum number of iterations, the residual of the entire CRN is calculated. The CRN is considered converged if the residual is sufficiently small. If the CRN has not converged, the absolute and relative tolerances of the substitution solver and the target residual for the local solver are decreased. The tolerances and local residual target scale with the global residual of the CRN. As it decreases, so do they. The absolute and relative tolerances do have a lower limit beyond which they cannot decrease. The approach of decreasing the local residual target in steps was chosen because it leads to faster convergence. The idea being, that the solver focusses on high residual reactors, whilst gradually decreasing the residual of the entire CRN.

3.2.2. Objective Function

The objective function that the solver tries to minimise is essentially the same as Equation 2.31, which is restated in a rearranged form below, for convenience. The general objective function for the whole CRN is given in Equation 3.9. Here $\vec{\mathrm{f}}$ is the inlet boundary condition vector, now of size $\mathrm{N_E}$. It now contains the inlet mass flow of the individual species per reactor instead of just the total inlet mass flow. Similarly, **C** is the mass flow matrix, now of size $\mathrm{N_E}$ *x* $\mathrm{N_E}$. $\mathrm{N_E}$ is simply the total number of equations that describe the CRN, which is the product of $\mathrm{N_R}$ and $\mathrm{N_S}$. The mass fractions of the $\mathrm{N_E}$ species are contained in $\vec{\omega}$. The net production rates of the $\mathrm{N_E}$ species for the current state is given by $\mathrm{R}(\vec{\omega})$. When the objective function is zero, it means that for all species in all reactors, the net mass flow and mass production rate are in balance. The non-zero values of $\mathrm{g}(\vec{\omega})$ are considered the residuals of the optimisation and have the units $\mathrm{kg\,s^{-1}}$.

$$\underbrace{\dot{m}_{i,\,out} - \dot{m}_{i,\,in}}_{net\ mass\ flow} = \underbrace{\dot{m}_i'''\,V}_{mass\ production} \tag{2.31}$$

$$\mathrm{g}(\vec{\omega}) = \underbrace{\vec{\mathrm{f}} - \mathbf{C}\vec{\omega}}_{net\ mass\ flow} + \underbrace{\mathrm{R}(\vec{\omega})}_{mass\ production} = 0 \tag{3.9}$$

Since the solver does not solve the entire CRN simultaneously but rather solves individual reactors, a slightly modified objective function is used. The modified objective function is shown in Equation 3.10. Here, $\mathbf{\Omega}$ is the aforementioned state matrix of size $\mathrm{N_R}$ *x* $\mathrm{N_S}$ and $\vec{\mathbf{\Omega}}_r$ is the section of the state matrix that refers to the reactor in question. Analogously, $\vec{\mathbf{C}}_r$ is the section of the mass flow matrix corresponding to the reactor. Finally, $\vec{\mathrm{f}}_r$ is the inlet boundary condition vector for the reactor, with size $\mathrm{N_S}$.

$$\mathrm{g}_r(\mathbf{\Omega}) = \vec{\mathrm{f}}_r - \vec{\mathbf{C}}_r\mathbf{\Omega} + \mathrm{R}(\vec{\mathbf{\Omega}}_r) = 0 \tag{3.10}$$

The Jacobian of the objective function is given by Equation 3.11. Here, the first term on the right hand side captures the change in net production rate with changing species mass fractions. A description of its analytical evaluation is given by Sampat [18]. The second term describes the change in mass outflow of a species with changing mass fractions. For a species, this term is linearly related to its mass fraction and is unrelated to the mass fractions of other species. Hence, this term contains the identity matrix I. The mass inflows from other reactors and the boundary conditions are not found in the Jacobian since they are unaffected by the species concentrations in the reactor of interest.

$$\mathbf{J} = \frac{\partial \mathrm{g}_r}{\partial \vec{\mathbf{\Omega}}_r} = \frac{\partial \mathrm{R}}{\partial \vec{\mathbf{\Omega}}_r} - M_r\mathrm{I} \tag{3.11}$$

3.2.3. Substitution Solver

To minimise the objective function of a reactor, a so-called false transient method is used, where Equation 3.10 is converted into an ODE, as shown in Equation 3.12. Since the objective function of a reactor gives the net mass flow rates of the species for the current state, integrating it over a given time interval yields their net mass accumulations. By dividing the objective function by the mass of the reactor, m_r, the integration yields a vector of mass fractions. By scaling this vector so that the sum of the mass fractions is one, it can be used to represent a reactor state. That is also the working principle of this solver. The initial state of the reactor is substituted with the scaled solution to Equation 3.12.

$$\frac{d\vec{\mathbf{\Omega}}_r}{dt} = \frac{\mathrm{g}_r(\mathbf{\Omega})}{m_r} \tag{3.12}$$

The solution to Equation 3.12 is found using the Backward Differentiation Formulas (BDF) method from *SciPy* [34], which is based on the work of Byrne and Hindmarsh [35]. This method uses BDF of order one to five and was chosen because it is suitable for stiff initial value problems. The initial value for the solver is taken as the end state of the last iteration or from the CFD results at the start of the simulation.

Importantly, it was decided to use a finite difference Jacobian rather than Equation 3.11. The time to convergence was substantially slower when using Equation 3.11.

4
Solver Verification

Since the last research using AGNES, the CRN generation code has been modified, and a new solver architecture is being employed. It is therefore necessary to verify that the CRN generation and solver work as intended. This is done by comparing the results of the current solver to the results obtained by Sutar [21]. In their research, they used a CFD simulation of Sandia Flame D [23] to perform CRN simulations. The results of these CRN simulations and the CFD simulation are still available, making their work a convenient choice for verification. In Section 4.1 the CFD simulation that forms the basis for the CRN used for the verification is discussed. Section 4.2 discusses the clustering approach that was used to generate the CRN and the boundary conditions that were used for the simulation. The verification of the current solver is performed in Section 4.3.

4.1. CFD Simulation

The CRN is created using the results of an *ANSYS Fluent* CFD simulation performed by Perpignan [36]. The simulation uses the Reynolds averaged Navier-Stokes (RANS) approach. The domain is two-dimensional and contains 24278 cells. Turbulence is modelled using the Reynolds Stress turbulence model, and radiative transport is modelled using the Discrete Ordinate model. Finally, the turbulence–chemistry interaction (TCI) is modelled using the Flamelet Generated Manifold (FGM) model. [21]

A visualisation of the CFD simulation can be seen in Figure 4.1. In these plots, the temperature is used for the colour map. It can be seen that the grid coarsens with an increase in streamwise and radial coordinates. Furthermore, it can be seen that the domain only captures the positive radial coordinates. In the radial direction, the domain is significantly larger than the burner dimension, as shown in Figure 1.4. This is done to capture the effect of the co-flow. One can also observe the low temperatures as the jet enters the domain but has not yet ignited. Figure 4.1b shows the experimental measurement locations mentioned in Table 1.3, with the exception of the negative radial measurements. As can be seen, the spacing of the radial measurements increases in the streamwise direction. As a result, the radial locations of the measurements correspond quite nicely to the areas of elevated temperature in the CFD simulation.

4.2. CRN Set-Up

Setting up a CRN in AGNES involves establishing the clustering criteria for the generation of the CRN and choosing whether to use the model for turbulent diffusive mass flows in the interconnectivity matrix. In this case, the turbulent diffusive mass flow model is used. The clustering approach used by Sutar [21] is summarised Table 4.1. It shows the temperature, T, and mean mixture fraction, $\bar{f}$, limits for the zones shown and the clustering criteria within each zone.

As discussed in Section 1.2, this approach was originally developed by Monaghan et al. [15] specifically for a CFD-CRN approach investigating Sandia Flame D. Here, the CFD domain is split into different zones, as shown in Figure 1.3, using the mean mixture fraction and the temperature. Within these zones, clustering limits are applied. For example, for a mean mixture fraction of zero, two cells can be clustered if the difference in x-coordinate is smaller than $0.2\,\mathrm{m}$. It should be noted that the CRNs created by Sutar [21] are still available. Thus, the clustering was not performed again for the verification of the solver. An example of a CRN with 500 reactors that was clustered using these criteria can be seen in Figure 4.2.

The solver requires the user to define the composition of the boundary conditions and the reaction mechanism. The boundary conditions that need to be defined for the Sandia Flame D simulation are the jet flow, the pilot flow, and the co-flow. The boundary conditions that were used by both Sutar [21] and De Wit [20] are shown in Table 4.2. It shows the species mass fractions for the three inlet boundary conditions. The co-flow uses a simplified composition for air, and the jet composition targets the Sandia

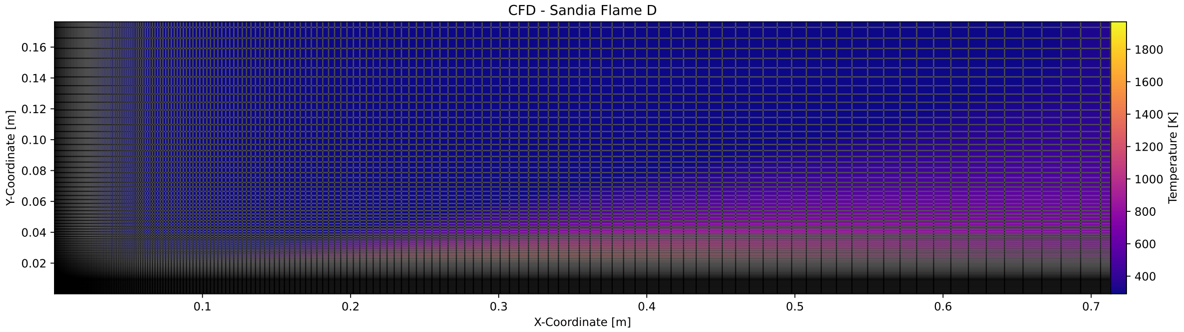

(a) Visualisation of the CFD domain for Sandia Flame D.

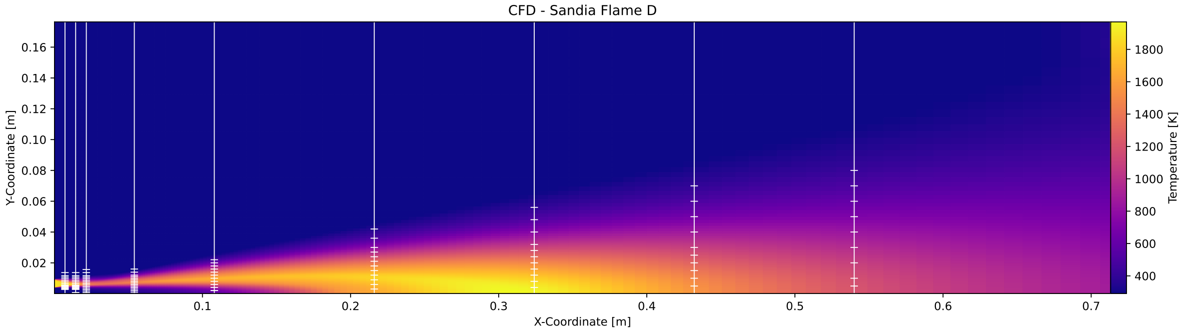

(b) Visualisation of the CFD domain for Sandia Flame D including the locations of the experimental measurements.

Figure 4.1: Visualisations of the Sandia Flame D CFD simulation using a colour map based on the cell temperatures.

specifications of 25% CH_4 and 75% dry air by volume [23]. The pilot composition is supposed to be that of a methane/air flame at $\varphi = 0.77$. However, the values differ significantly from the values in the Sandia documentation [23]. It is uncertain where the composition of the pilot stems from. Since the aim is to verify that the solver works as intended, the same boundary conditions are still used in this work.

Table 4.1: Clustering Criteria used by Sutar [21] based on the clustering criteria employed by Monaghan et al. [15].

Zone limits		Clustering limits
$0 \leq \bar{f} \leq .01$		$\Delta \mathrm{x} = 0.2$ m
$.01 < \bar{f} \leq 0.1$		$\Delta \mathrm{T} = 100$ K
$0.1 < \bar{f} \leq 0.9,$	$\mathrm{T} \leq 1800$ K	$\Delta \mathrm{T} = 100$ K
$0.1 < \bar{f} \leq 0.9,$	$1800 < \mathrm{T} \leq 2000$ K	$\Delta \mathrm{T} = 50$ K
$0.1 < \bar{f} \leq 0.9,$	$\mathrm{T} > 2000$ K	$\Delta \mathrm{T} = 2$ K
$0.9 < \bar{f} \leq 1.0$		$\Delta \bar{f} = 0.01$ & $\Delta \mathrm{x} = 0.01$ m

Table 4.2: Species mass fractions for the boundary conditions of Sandia Flame D.

Species	Co-Flow	Jet	Pilot
CH_4	–	0.16	–
O_2	0.23	0.19	0.059
N_2	0.77	0.65	0.735
H_2O	–	–	0.091
CO_2	–	–	0.111
OH	–	–	0.001
NO	–	–	0.003

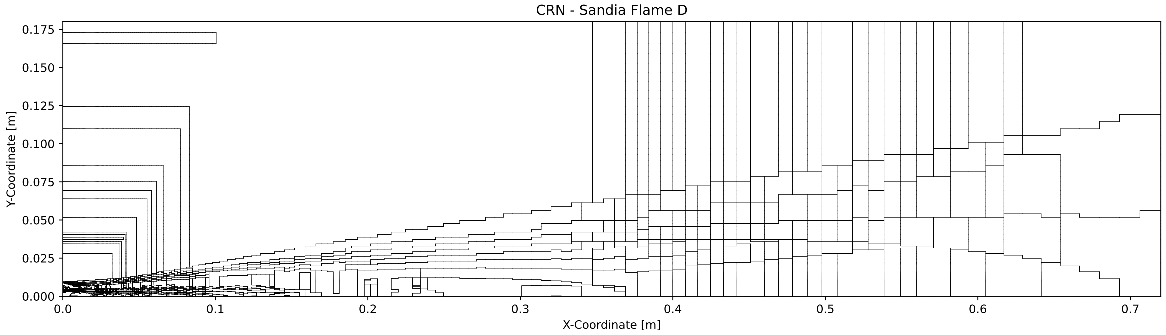

Figure 4.2: An example of a 500 reactor CRN structure for Sandia Flame D using the clustering criteria in Table 4.1.

4.3. Results

Since the original clusters are still available for the simulations performed by Sutar [21], only the CRN generation from the clusters and the solving of the CRN can be verified in this step. The clustering approach they employed is not used in this work and is therefore not verified in a separate step. The appropriate functioning of both the CRN generation and the solver can be verified by comparing the solutions obtained by Sutar [21] and the solutions obtained by the solver described in Chapter 3. Any differences in the CRN generation would inevitably result in discrepancies between the solutions.

Radial plots of the major species concentrations at axial locations $x/d = 15$ can be found in Figure A.11, Figure A.12, Figure A.13, and Figure A.14. In these plots, the initial and final states of the CRN are shown, which were obtained using the current solver. The initial state is the state of the CRN after the CRN generation, with the species concentrations stemming from the CFD results. The final state is the state of the CRN at the lowest achieved residual norm, ε, which was $\varepsilon < 10^{-11}$. In addition, intermediate states of the CRN are shown at the specified residual norm. Finally, the solution obtained by Sutar [21] is also shown. Next to the mass fraction distribution in the radial direction, a volume integral of the individual graphs is presented. Additional plots at different axial locations can be found in Appendix A.

As is visible in all the major species plots, the current solver finds a very similar solution to the one found by the previous iteration of AGNES. They also show that the CRN state changes significantly between the initial and final state. This verifies that the solution data available from Sutar [21] is indeed the solution to the same objective function. It would be very unlikely for the current solver to converge towards an arbitrary state of a previous solver. They also show that the current and previous solver do not have the exact same solution, as is visible in Figure A.11. There, the volume integral of the current solution is marginally larger than the volume integral of the old solution. The major species plots show a similar level of agreement at all the inspected axial locations.

Since the solver's ability to simulate NO emissions is of most interest, a comparison of the predicted NO mass fractions is shown in Figure A.15. As for the major species, the current solver clearly converges to a very similar state as the previous solver. Again, a slight difference can be observed between the two solutions in the volume integral plot. The NO volume integral plots at different axial locations, not shown here for brevity, do not show such a discrepancy.

To conclude, the current solver predicts virtually the same radial concentrations of the major species and NO as the previous solver at various axial locations. While small differences can be observed in some of the volume integrals, they are of negligible magnitude. It can also clearly be observed that the current solver converges to the same final state from a substantially different initial state. Therefore, it can be said that the current CRN generation and solver work as intended.

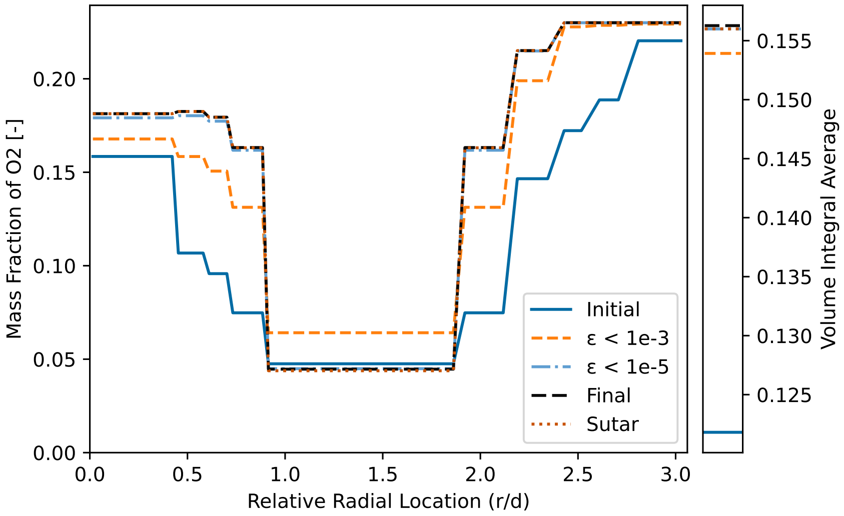

Figure 4.3: Radial plot of Y_{O_2} at axial location x/d = 15 for a 1000 reactor CRN, with the initial CRN state (the solid blue line), CRN state at $\varepsilon < 10^{-3}$ (short orange dashes), CRN state at $\varepsilon < 10^{-5}$ (light blue dash-dotted line), final CRN state (long black dashes), and final result from Sutar [21] (dotted red line).

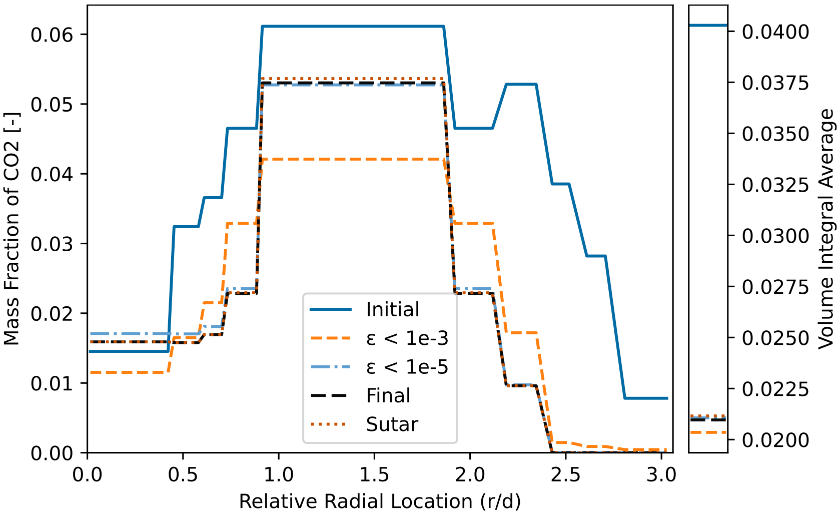

Figure 4.4: Radial plot of Y_{CO_2} at axial location x/d = 15 for a 1000 reactor CRN, with the initial CRN state (the solid blue line), CRN state at $\varepsilon < 10^{-3}$ (short orange dashes), CRN state at $\varepsilon < 10^{-5}$ (light blue dash-dotted line), final CRN state (long black dashes), and final result from Sutar [21] (dotted red line).

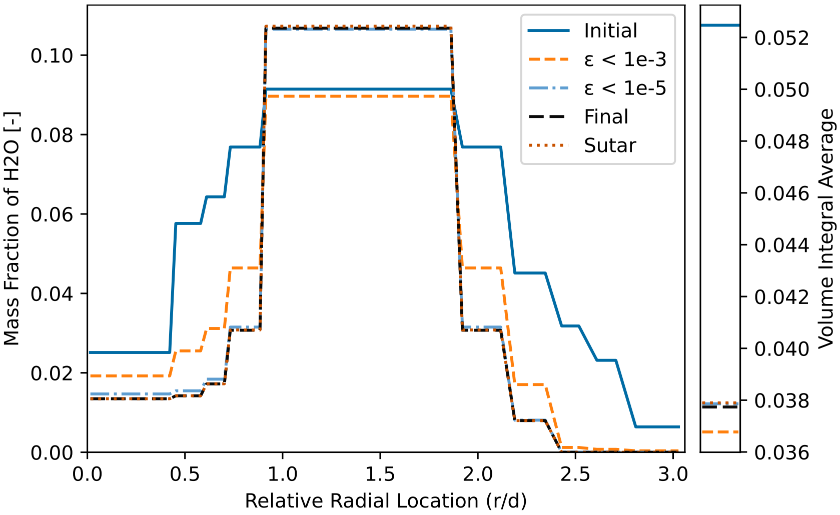

Figure 4.5: Radial plot of Y_{H_2O} at axial location x/d = 15 for a 1000 reactor CRN, with the initial CRN state (the solid blue line), CRN state at $\varepsilon < 10^{-3}$ (short orange dashes), CRN state at $\varepsilon < 10^{-5}$ (light blue dash-dotted line), final CRN state (long black dashes), and final result from Sutar [21] (dotted red line).

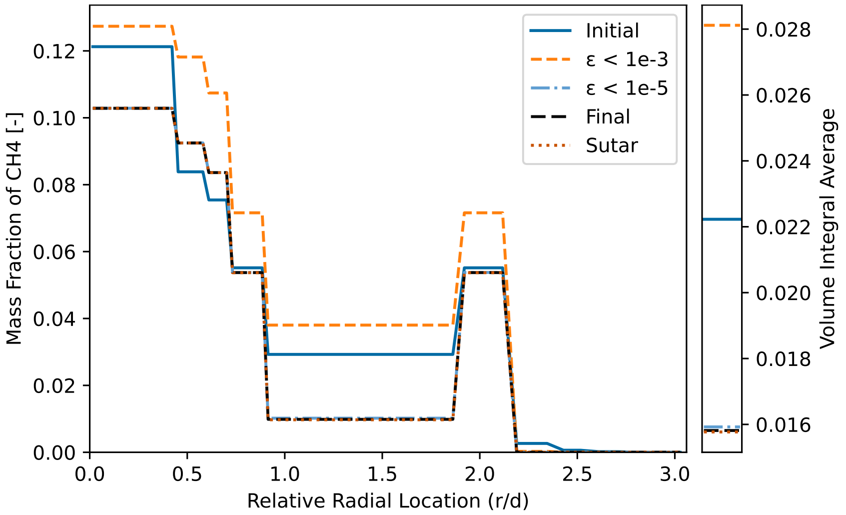

Figure 4.6: Radial plot of Y_{CH_4} at axial location x/d = 15 for a 1000 reactor CRN, with the initial CRN state (the solid blue line), CRN state at $\varepsilon < 10^{-3}$ (short orange dashes), CRN state at $\varepsilon < 10^{-5}$ (light blue dash-dotted line), final CRN state (long black dashes), and final result from Sutar [21] (dotted red line).

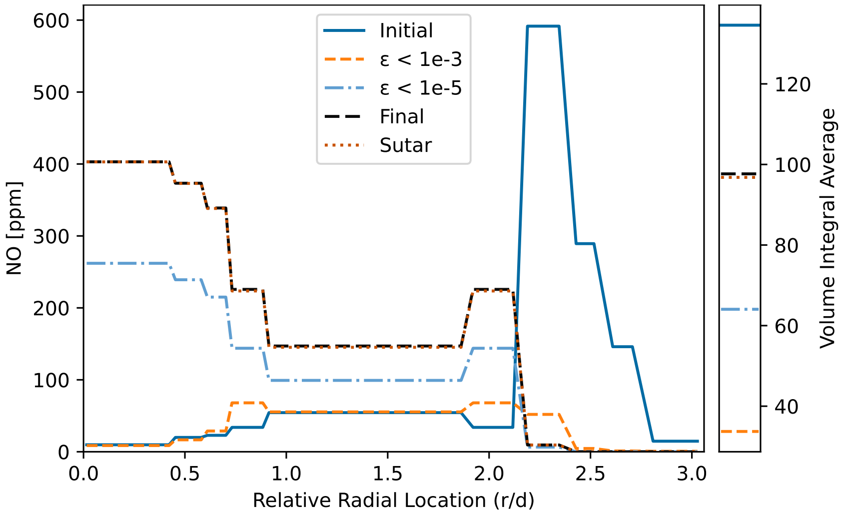

Figure 4.7: Radial plot of Y_{NO} at axial location x/d = 15 for a 1000 reactor CRN, with the initial CRN state (the solid blue line), CRN state at $\varepsilon < 10^{-3}$ (short orange dashes), CRN state at $\varepsilon < 10^{-5}$ (light blue dash-dotted line), final CRN state (long black dashes), and final result from Sutar [21] (dotted red line).

5

APPU Burner Methodology & Assessment

This chapter presents the methodology employed to create the CRN for the APPU burner and assesses its performance under the operating conditions used in the CFD simulations. The employed methodology is discussed in Section 5.1. The assessment of the performance of the CRN can be found in Section 5.2.

5.1. APPU CRN Methodology

This section describes how the CRN used to study the APPU burner were generated and set up to study the effect of the operating conditions. Subsection 5.1.1 discusses the CFD simulation that is used to generate the CRN. The approach used to cluster the CFD cells is explained in Subsection 5.1.2. The setup of the baseline CRN and the CRN under different operating conditions is described in Subsection 5.1.3.

5.1.1. CFD Simulation

The CRN for the APPU burner are also based on an *ANSYS Fluent* RANS CFD simulation. The simulation was performed by V. De Lauso. The CFD mesh is significantly more complex than the *Sandia* case. The mesh is three-dimensional, contains 1478882 cells, has periodicity, and two cell zones. The turbulence is modelled using the *shear stress transport k-*ω model, and the TCI is modelled using an FGM model with 20 species, excluding NO. Unlike the Sandia flame D simulation, this simulation does not employ a heat radiation model. The CFD simulation was run for only one operating condition. Namely, P=$5.66\,\mathrm{kW}$, AAI=0%, X_{CH_4}=1, $\dot{m}_{air}$=$2.69\,\mathrm{g\,s^{-1}}$, and φ=0.72. These operating conditions are slightly different to the operating conditions of the experiments discussed in Section 1.1.

A visualisation of the CFD simulation can be seen in Subsection 5.1.3. The CFD simulation only captures half of the geometry of the combustor, thus also only using half the inlet mass flows and half the power. A view of the symmetry plane is given in Figure 5.1a, truncated at $0.2\,\mathrm{m}$ for clarity. It shows the periodic zones that are used to simulate the full geometry of the combustor. A periodic face exchanges flow with its shadow-periodic counterpart as if the two cells were adjacent. The periodic zones and their respective shadow zones are shown in the same colour, with the shadow zones being hatched. The small face zones of 1996, 1997, 1998, 1999, and their shadow zones simulate the swirler. Likewise, zone 223 simulates the air inlet for the swirler. The rest of the domain, including the AAI, is simulated using zone 215.

Figure 5.1a also gives an idea of the meshing. The inlet tube is quite finely meshed to capture the mixing of methane and air. Similarly, the swirler is also finely meshed to capture the development of the swirl. The finest meshing can be seen close to the exit of the inlet tube. This is where the combustion occurs. The ”w”-shaped area with fine meshing is used to capture the effect of the inner and outer recirculation zones. The recirculation zones occur due to the swirl of the flow, recirculating hot gases that ignite the fuel mixture entering the combustor. The radial plane shown in Figure 5.1b is located $25\,\mathrm{mm}$ above the exit of the inlet tube. A clear flame boundary can be seen at the outer radius of the inlet tube, but also in the centre. Here the partially premixed gases are ignited by the recirculation zones. Finally, the mesh also coarsens with increasing streamwise coordinate. The mesh size in the radial plane is also coarser further from the centre. It also coarsens, in general, with increasing streamwise coordinate.

5.1.2. Clustering

The majority of the CFD mesh was clustered using a relative tolerance approach. In this approach, every variable in the clustering criteria is subjected to Equation 5.1 in the fitness check. Here, q refers

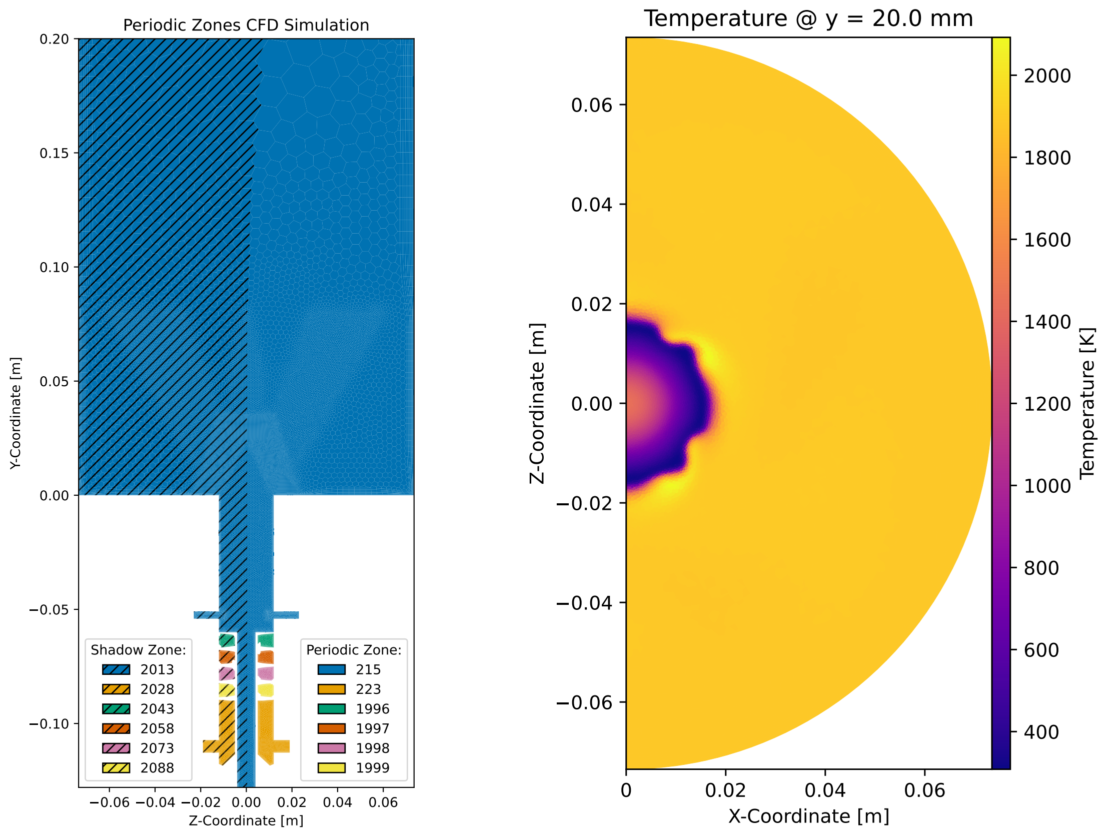

(a) Side view of the APPU CFD simulation excluding Y-coordinates above $0.2\,\mathrm{m}$. The depicted YZ-plane is located at x = $0.1\,\mathrm{mm}$.

(b) Top-down view of the APPU CFD simulation. The depicted XZ-plane is located at y = $20\,\mathrm{mm}$.

Figure 5.1: Visualisation of the APPU CFD simulation using cell temperature as colour map.

to the value of the variable for the inspected and active cluster, and σ is the relative tolerance. The clustering starts with a tight relative tolerance, such as $\sigma = 0.01$. When the clustering stagnates, the relative tolerance is relaxed. This procedure is repeated until the desired number of clusters is reached.

$$\frac{|q_{act} - q_{ins}|}{q_{act}} \leq \sigma \tag{5.1}$$

The areas represented by zones 2028, 2043, 2058, 2073, 2088, and 223 in Figure 5.1a are not clustered as described above. The cells in those areas are in a different cell zone than the rest of the cells in the mesh. As a result, they don't share any faces with the rest of the mesh, making clustering them together difficult. Therefore, it was decided to cluster the approximately 200,000 cells into one large cluster. This is an acceptable compromise since the cell zone in question only captures the inlet air. Since flow properties such as swirl are not of interest for the CRN and no chemical reactions are occurring in that region, no valuable information is lost. The air mass flow through the cluster is shared with the other clusters through the periodic boundary condition.

For the rest of the cells, two different clustering criteria were used. Initially, the clustering function shown Equation 5.2 was used, referred to as *clustering I*. This was based on the clustering criteria shown in Table 4.1. The intention being that by restricting the y-coordinate, the clustering algorithm would be forced to create more clusters in the radial direction. Thus, increasing the radial resolution. For $y \leq -5.5\,\mathrm{cm}$, the restriction is dropped, because it resulted in a significant number of reactors in the swirler, which was not desired. The limit of $-5.5\,\mathrm{cm}$ coincides with the bottom of the fuel inlet.

The mean mixture fraction was mainly chosen for the mixing tube above the methane inlet. It describes how much of the mass in a cell stems from the fuel inlet and how much originates from the air inlet. Since the combustion is only partially premixed, it was thought to be important to retain some resolution of the mixing in the mixing tube. The temperature is used because it is a very important factor in the production rate of species. Therefore, an accurate representation of the temperature field is essential for good results.

$$\left.\begin{aligned}|\bar{f}_{act}-\bar{f}_{ins}| &= \sigma\cdot\bar{f}_{act}\\ |T_{act}-T_{ins}| &= \sigma\cdot T_{act}\end{aligned}\right\} y \leq -5.5\,\mathrm{cm} \qquad \left.\begin{aligned}|\bar{f}_{act}-\bar{f}_{ins}| &= \sigma\cdot\bar{f}_{act}\\ |T_{act}-T_{ins}| &= \sigma\cdot T_{act}\\ |y_{act}-y_{ins}| &= 2\sigma\cdot y_{act}\end{aligned}\right\} y > -5.5\,\mathrm{cm} \tag{5.2}$$

Initial results indicated that restricting the streamwise length of the clusters had an adverse effect on the capture of the flame profile. Therefore, a second clustering function was used that removed the restriction on the y-coordinate entirely. The *clustering II* function is shown in Equation 5.3.

$$\begin{aligned}|\bar{f}_{act}-\bar{f}_{ins}| &= \sigma\cdot\bar{f}_{act}\\ |T_{act}-T_{ins}| &= \sigma\cdot T_{act}\end{aligned} \tag{5.3}$$

5.1.3. CRN Set-Up

The chemical mechanism used is again the *GRI-Mech 3.0* [25]. The boundary conditions that need to be defined for this CRN are only the main air inlet and the fuel inlet. The axial air inlet is not used and does not need to be defined. The compositions of the boundary conditions are taken from the CFD simulation and can be found in Table 5.1.

In order to perform the sensitivity studies, changes had to be made in the generation of the CRN. For the temperature sensitivity studies, the temperature assigned to a reactor during CRN generation was simply multiplied by the desired factor. The change in temperature is localised to each reactor because the reactors only share mass flow with each other. This means that the increased temperature of a reactor does not affect the temperature of neighbouring reactors. This approach also increases the temperature in non-reacting areas, such as the mixing tube, which is not an issue for small factors because the temperatures are not high enough for relevant reactions to occur. The same approach as for temperature was also used for the density sensitivity study. In both cases, the mass flow of the boundary conditions was not changed and thus the mass flow between reactors also stays the same.

Table 5.1: Boundary condition mass fraction for the baseline case.

Species	Fuel Inlet	Air Inlet
CH_4	1	–
O_2	–	0.23
N_2	–	0.77
H_2	–	–

For the equivalence ratio sensitivity study, it was decided to keep the fuel mass flow constant and to vary the inlet air mass flow. This keeps the power of the combustion constant. The required air mass flow for a given equivalence ratio can be found using Equation 5.4[8]. The air mass flow is then changed during the CRN generation when the cell faces relevant to the air inlet boundary condition are read. The found mass flux across the cell faces is then multiplied by desired mass flow divided by the original mass flow. Since this correction occurs before the mass flow correction of the CRN, it also affects the mass flow of the reactors and between the reactors. The required air mass flow for the equivalence ratio study can be found in Table 5.2.

$$\begin{aligned}\varphi &= s\,\frac{\dot{m}_{CH_4}+\dot{m}_{H_2}}{\dot{m}_{air}}\\ s &= \frac{(2-1.5X_{\mathrm{H_2}})\,(MW_{\mathrm{O_2}}+3.76MW_{\mathrm{N_2}})}{X_{\mathrm{CH_4}}MW_{\mathrm{CH_4}}+X_{\mathrm{H_2}}MW_{\mathrm{H_2}}}\end{aligned} \tag{5.4}$$

A similar approach is also used for the introduction of hydrogen. In this case, the fuel mass flow is changed to keep the power constant and the air mass flow is kept constant. Again, the mass flux from the relevant cell faces is changed proportionally to achieve the desired fuel mass flow. As before, this results in altered reactor mass flows. The required fuel mass flow is found from Equation 5.5. The lower heating values for hydrogen and methane were taken to be $120\,\mathrm{kJ\,g^{-1}}$ and $50\,\mathrm{kJ\,g^{-1}}$, respectively. The required fuel mass flows and the corresponding equivalence ratios can be found in Table 5.3. In addition to changing the fuel mass flow, obviously the compositions of the fuel inlet boundary condition have to be changed.

$$P = \dot{m}_{fuel} \cdot (Y_{CH_4} \cdot LHV_{CH_4} + Y_{H_2} \cdot LHV_{H_2}) \tag{5.5}$$

Table 5.2: Fuel mass flows for equivalence ratio study.

φ	0.68	.70	0.72	0.74	0.76
$\dot{m}_{air}$ $[\mathrm{g\,s^{-1}}]$	2.85	2.77	2.69	2.62	2.55

Table 5.3: Fuel mass flows for hydrogen study.

X_{H_2}	0	0.25	0.40	0.60	0.80
$\dot{m}_{fuel}$ $[\mathrm{g\,s^{-1}}]$	.113	.107	0.102	0.093	0.077
φ	0.72	.71	0.70	0.68	0.65

5.2. Results of the Baseline Case

In this section, the results of the baseline case are presented and discussed. The baseline case refers to the operating conditions that were used for the CFD simulation, which serves as the basis for the CRN generation. In Subsection 5.2.1, a qualitative assessment of the ability of the CRN to capture the temperature field is made.

5.2.1. Resolution of the Clustered Temperature Field

It is important for a CRN to capture the temperature field well since temperature has a large influence on the production rates of species. However, it is in the nature of clustering cells that some accuracy is lost. In general, the smaller the ratio of reactors in the CRN to cells in the CFD mesh, the worse the accuracy. The three-dimensional nature of the domain makes it difficult to verify the temperature field at every location. Instead, the temperature field is inspected parallel to the symmetry plane of the domain.

The difference in temperature resolution for a 500 reactor and a 2000 reactor CRN using *clustering I* is shown in Figure 5.2. For both CRN, the loss of detail in the flame region is obvious. However, for the 500 reactor CRN, the locally elevated temperature at the flame tips has completely disappeared. It was clustered with the combustion gases outside of the flame structure, slightly increasing the temperature there compared to the CFD results. In the centre of the flame, the resolution of the temperature has also decreased. There, intermediate temperatures were clustered together, losing the temperature gradient from the CFD. The colder regions of the flame are less affected by the clustering because the temperature gradient is steeper, requiring a larger relative tolerance, which was evidently not reached.

The 2000 reactor CRN captures the temperature more accurately. The temperature in the centre of the flame has gained some resolution. A more representative vertical gradient has appeared compared to the 500 reactors. The influence of the y-coordinate in the clustering criteria is evident. The gradient from the cold gas to the hot centre is still mostly lost. The aforementioned elevated temperatures are captured more accurately. As a result, the temperature of the flue gases is now also closer to the CFD results. With the temperature being quite homogeneous above y = $0.1\,\mathrm{m}$, the number of clusters does not significantly affect the resolution in that region.

A similar relationship between temperature resolution and the number of reactors can also be observed for *clustering II* in Figure 5.3. The temperature profile in the centre of the flame is almost entirely lost with 500 reactors. The centre of the flame has the same temperature as the gas outside the flame structure. With 2000 reactors, the temperature in the centre of the flame is more similar to the temperature in the CFD results. Again, the locally elevated temperatures are captured by the 2000 reactors, whilst being lost for the 500 reactors. Since the y-coordinate is not part of the clustering criteria, some non-uniformity can be observed in the flue gas above y=$0.1\,\mathrm{m}$. This is especially apparent for the 500 reactors.

5.2.2. Major Species Emissions

Major combustion species concentrations are usually not of interest in CRN simulations. CFD simulations are more than capable of predicting the production and transportation of major species accurately. In fact, it is required for the simulation of reacting flows. Therefore, for CFD-CRN approaches, the information on the major species is already available. However, the major species can be used to verify that combustion is being simulated properly by the CRN, with the expected mole fractions coming from the stoichiometric equation for methane combustion.

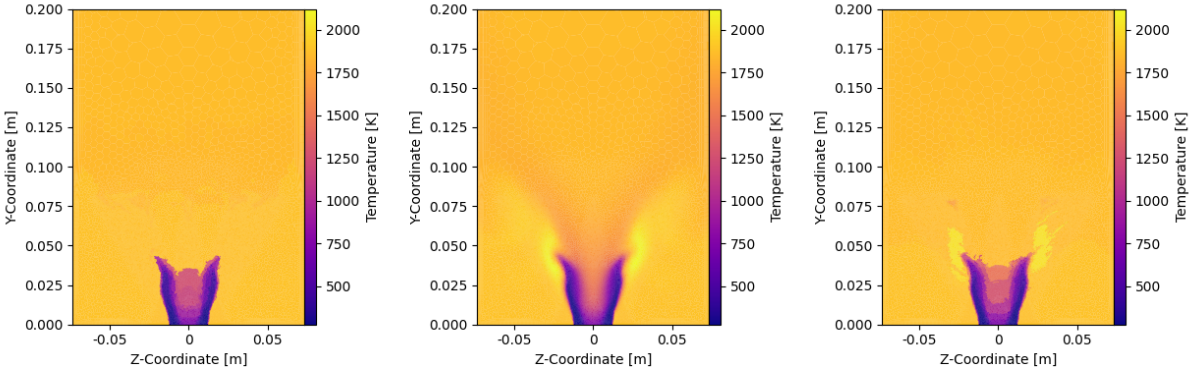

(a) 500 reactors, clustering I **(b)** CFD **(c)** 2000 reactors, clustering I

Figure 5.2: A comparison in temperature resolution parallel to the symmetry plane at x = $1\,\mathrm{mm}$ between a 500 and 2000 reactor using *clustering I*.

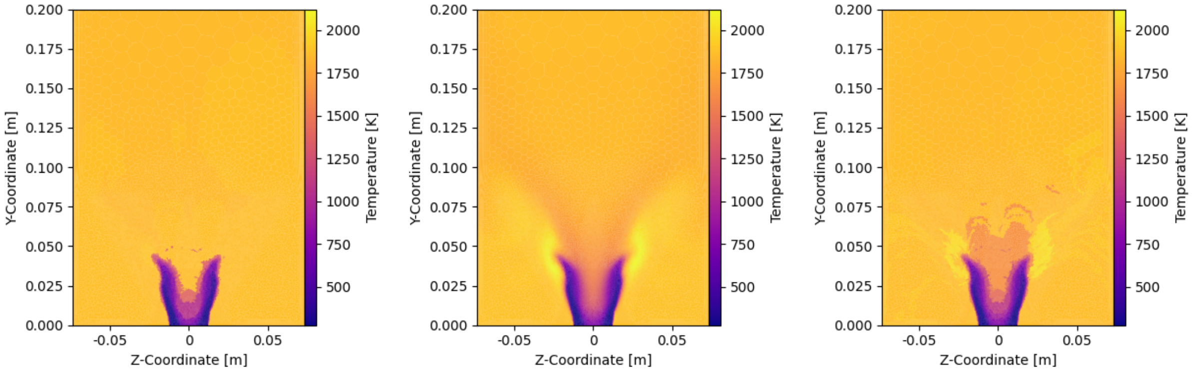

(a) 500 reactors, clustering II **(b)** CFD **(c)** 2000 reactors, clustering II

Figure 5.3: A comparison in temperature resolution parallel to the symmetry plane at x = $1\,\mathrm{mm}$ between a 500 and 2000 reactor using *clustering II*.

Mole Fraction plots for H_2O, O_2, and CO_2 can be found in Figure 5.4,Figure 5.5, and Figure 5.6, respectively. The expected mole fractions are $\mathrm{X}_{\mathrm{H_2O}} \approx 0.14$, $\mathrm{X}_{\mathrm{O_2}} \approx 0.06$, and $\mathrm{X}_{\mathrm{CO_2}} \approx 0.07$. As can be seen in the plots, both the CRN and the CFD results predict the mole fraction accurately in the flue gas. However, there are significant differences in the predicted mole fractions in the flame area. In the CFD results, the area with locally elevated temperatures discussed in Subsection 5.2.1 reappears. It appears through high concentrations of H_2O and CO_2 and low concentrations of O_2. This corresponds to locally elevated equivalence ratios, which can occur due to the partially pre-mixed nature of the combustor. Indeed, in the CFD simulation, said area has a mean mixture fraction of $\bar{f} \approx 0.05$ which translates to an equivalence ratio of $\varphi \approx 0.9$.

While the CRN capture the areas of locally elevated temperatures, as discussed in Subsection 5.2.1, they are not as apparent in the mole fraction plots of the major species. They are most noticeable in Figure 5.6. Looking at the production rate of methane in Figure 5.7, the CRN actually predict that almost no methane reaches the areas of elevated temperature. Instead, the methane combusts where the partially premixed gas interacts with the recirculation zones. The production rates also show the effect of the clustering criteria. For *clustering I*, the combustion of methane occurs in a concentrated area in the centre of the flame, whereas it occurs at a lower rate over a larger area for *clustering II*. In conclusion, the CRN capture locally elevated temperatures predicted by the CFD due to local variations in equivalence ratio, but do not predict the same phenomenon. This leads to a discrepancy between the chemistry and the temperature.

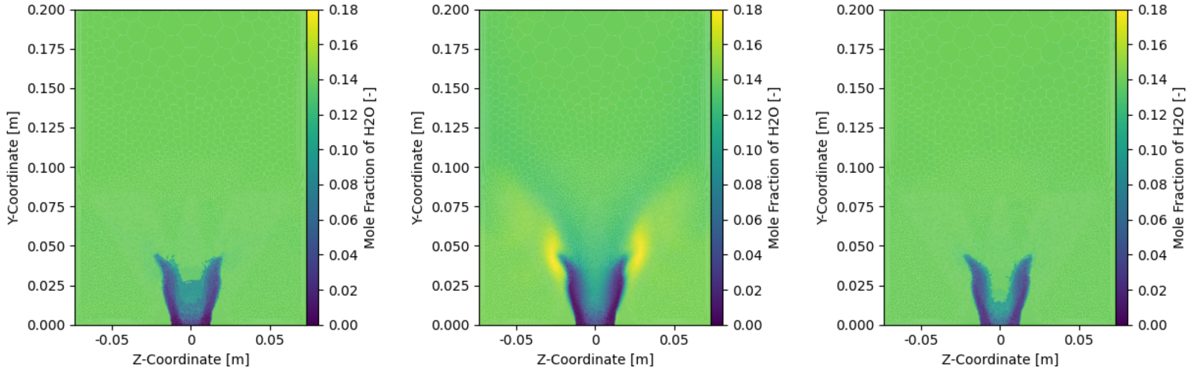

(a) Clustering I **(b)** CFD **(c)** Clustering II

Figure 5.4: Mole Fractions of H_2O parallel to the symmetry plane at x=$1\,\mathrm{mm}$ for 2000 reactor CRN and the CFD simulation.

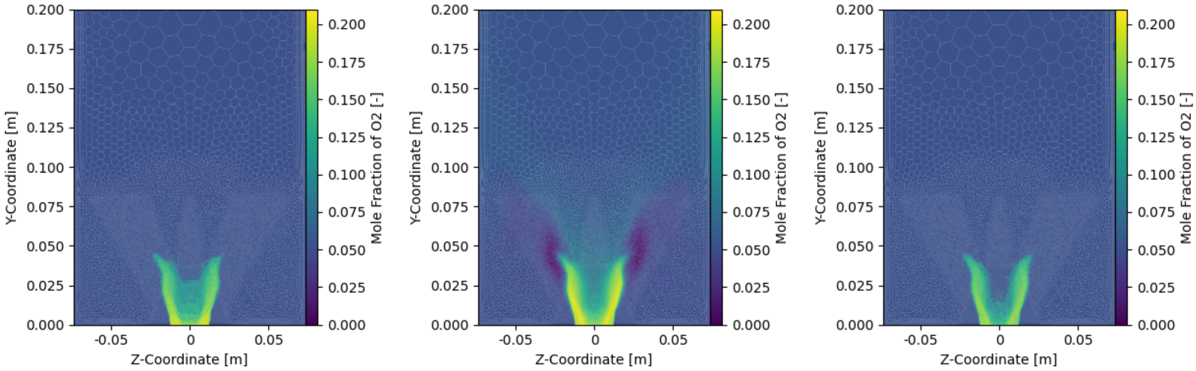

(a) Clustering I **(b)** CFD **(c)** Clustering II

Figure 5.5: Mole Fractions of O_2 parallel to the symmetry plane at x=$1\,\mathrm{mm}$ for 2000 reactor CRN and the CFD simulation.

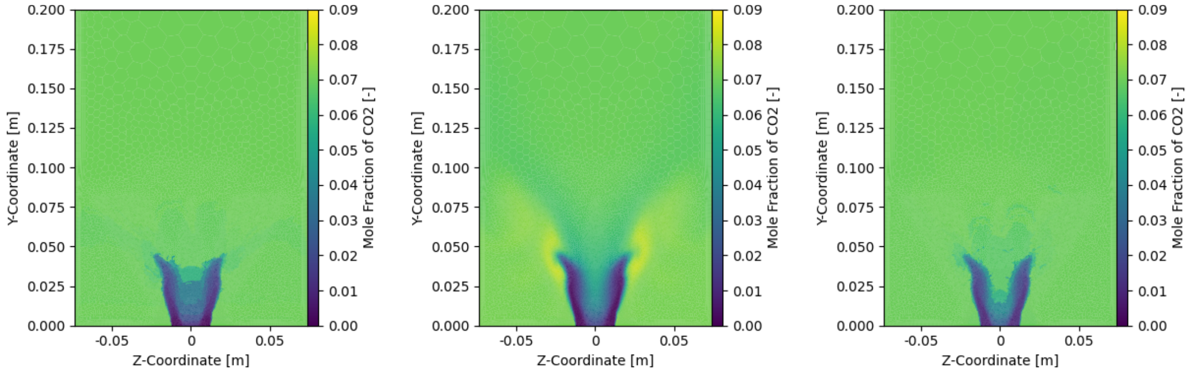

(a) Clustering I **(b)** CFD **(c)** Clustering II

Figure 5.6: Mole Fractions of CO_2 parallel to the symmetry plane at x=$1\,\mathrm{mm}$ for 2000 reactor CRN and the CFD simulation.

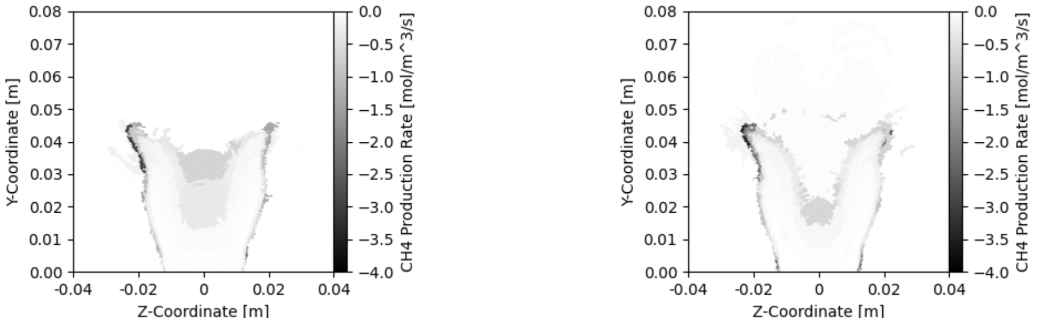

(a) Clustering I **(b)** Clustering II

Figure 5.7: Net production rate of CH_4 parallel to the symmetry plane at x=$1\,\mathrm{mm}$ for 2000 reactor CRN.

5.2.3. NO Emissions

The predicted NO concentrations in the domain can be seen in Figure 5.8. It is clearly visible that the CFD simulation predicts much higher NO emissions than the CRN approach. At the outlet, the CFD simulation estimates NO concentrations of $2668\,\mathrm{ppm}$. The CRN models predict a total NO production of $51\,\mathrm{ppm}$ and $45\,\mathrm{ppm}$ for *clustering I* and *clustering II*, respectively. Since NO is not part of the reaction mechanism of the CFD simulation, a post-processing function [37] is used to estimate NO based on the final state of the simulation.

Experimental values obtained by Link et al. [8] found NO concentrations on the order of $5\,\mathrm{ppm}$, corrected for 15% oxygen (wet). Applying the same correction, the NO concentrations of *clustering I*, *clustering II*, and the CFD simulation are $19.2\,\mathrm{ppm}$, $17.1\,\mathrm{ppm}$, and $1011\,\mathrm{ppm}$, respectively. It should be noted that the experimental values were obtained under slightly different operating conditions, with AAI=20% compared to AAI=0% in the CFD simulation and thus also in the CRN. Increasing the AAI, generally increases the NO emissions, likely due to poorer mixing [8]. Still, it can be concluded that the NO concentrations predicted by the CRN are significantly more realistic than the CFD results.

Looking at Figure 5.8a and Figure 5.8c, once again the effect of the clustering criteria is visible. However, both clustering approaches do show a similar pattern. As expected, the NO concentrations in the gas entering the combustion chamber is essentially zero. In the reactive layer and in the centre of the flame, small NO concentrations appear, which are transported to the flue gas. This creates a type of baseline NO emission, which propagates through the domain. Since the flue gas is relatively hot, additional NO is formed as the gas moves through the combustion chamber towards the outlet.

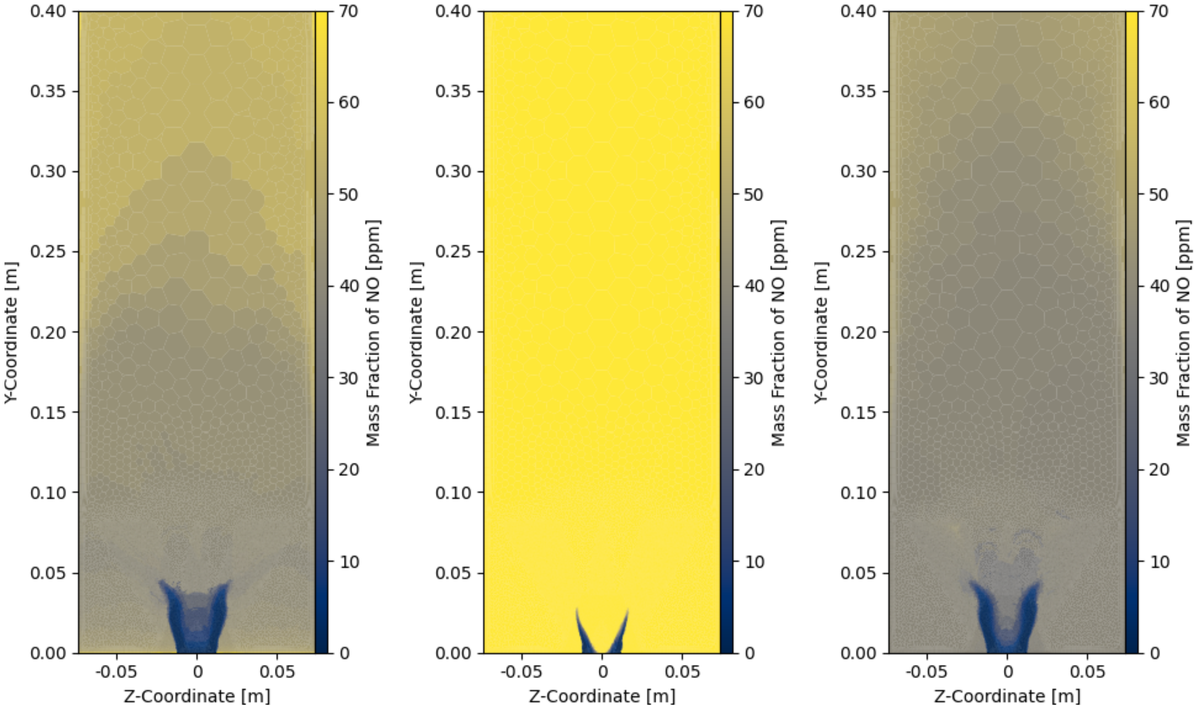

(a) Clustering I **(b)** CFD **(c)** Clustering II

Figure 5.8: Mass Fractions of NO parallel to the symmetry plane at x=$1\,\mathrm{mm}$ for 2000 reactor CRN and the CFD simulation.

The total net production rate and the net production rates of the individual pathways for *clustering I* can be seen in Figure 5.9. Since both clustering criteria show very similar patterns, the production rate plots for *clustering II* are found in Appendix B. Figure 5.9a shows that the highest production rate is found close to the flame region. The NO production in the centre of the flame is dominated by the prompt mechanism, which is responsible for around 55% of the NO production. This is due to the abundance of intermediate species of methane combustion in this region, which are required for prompt NO. The thermal and N_2O pathways account for approximately 30% and 10%, respectively. The remaining contribution is from the NNH pathway.

Figure 5.9a shows that the production rate is still significant downstream, as was evident in Figure 5.8. Looking at Figure 5.9b, it can be concluded that the majority of the downstream NO production is due to thermal NO. While the prompt and N_2O pathways also contribute, their production rates are substantially smaller. The decrease in the prompt pathway in the streamwise direction is simply due to the depletion of the aforementioned intermediate species. For $y \geq 0.1\mathrm{m}$, the thermal pathway accounts for more than 70% of the net NO production, increasing to 90% close to the outlet. Finally, it can be seen that the NNH mechanism does not contribute significantly to NO production outside of the flame region. In fact, it does not seem to meaningfully affect NO emissions in general.

Whilst production rates close to the flame are an order of magnitude larger than those downstream, one should take into account that the region is relatively small. Thus, the volume is relatively small, limiting the moles of NO produced. As a result, the small production rates downstream are still a relevant source of NO due to the large volume of the region. To quantify this, the contributions of the individual pathways to the total NO production are shown in Table 5.4. It is evident that the thermal pathway dominates the NO production. Despite relatively high peak production rates, the prompt and N_2O pathways are relatively small contributors. It also confirms that the downstream NO production is relevant to the total NO emissions. Since the downstream NO is mainly produced by the thermal pathway, the temperature of the flue gases has a significant influence on the predicted NO concentration at the outlet. The lack of a radiative heat model in the CFD simulation could result in overestimated temperatures in the flue gas. If that is indeed the case, it could partially explain the discrepancy between the CRN and experimental results.

Table 5.4 also shows that *clustering I* has higher production rates for all pathways. This is likely due to a difference in temperature distribution between the clustering criteria. It can also be seen that the NNH pathway is indeed not a significant contributor to the overall NO production. Interestingly, the N_2O pathway produces more NO than the prompt pathway, despite lower peak production rates. This is due to the slightly higher production rates downstream.

Table 5.4: Contribution of individual pathways to the total NO production in mass fractions ppm.

	Thermal	**Prompt**	**N_2O**	**NNH**
Clustering I	39.4	4.29	6.63	0.817
Clustering II	37.0	2.81	5.16	0.525

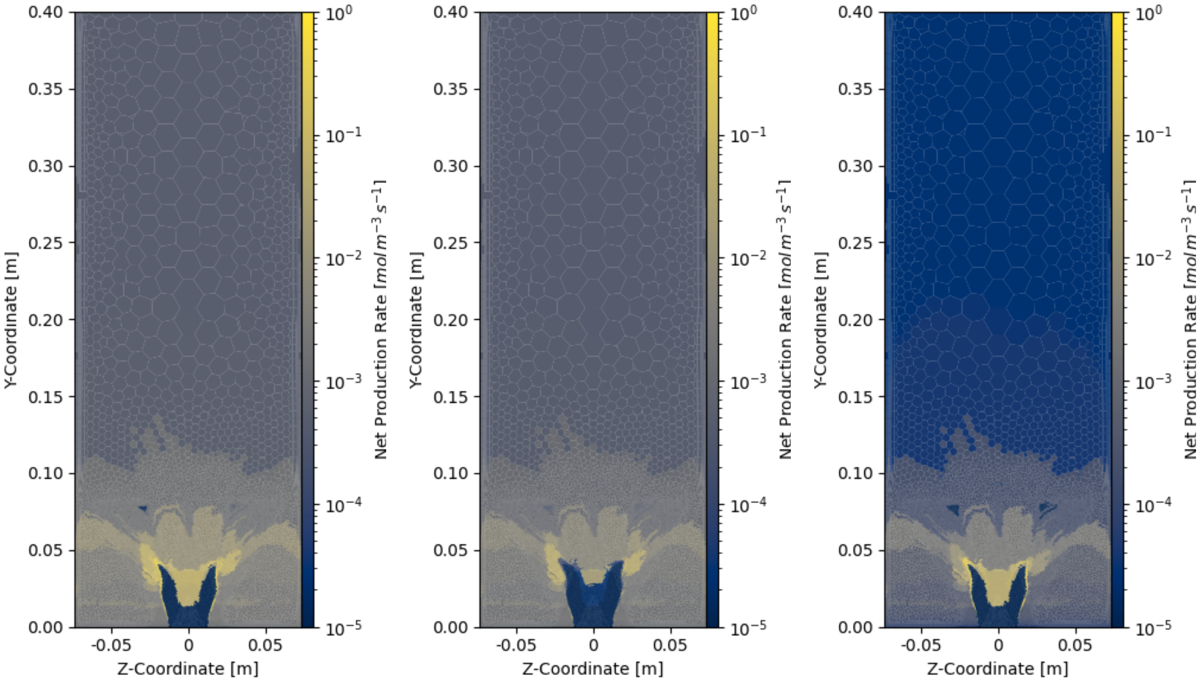

(a) Total **(b)** Thermal **(c)** Prompt

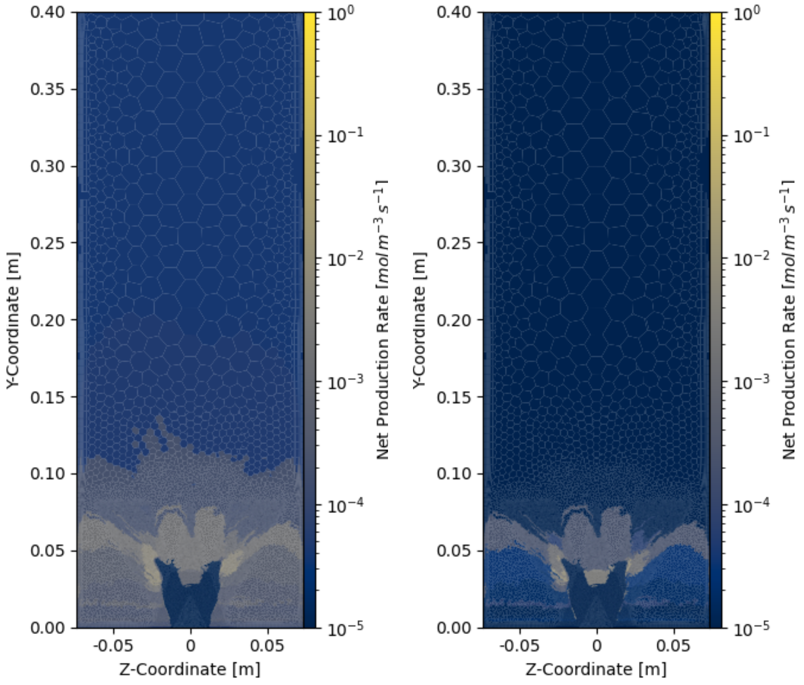

(d) N_2O **(e)** NNH

Figure 5.9: Net production rates of total NO and its various pathways parallel to the symmetry plane at x=$1\,\mathrm{mm}$ for a 2000 reactor CRN using *clustering I*.

5.2.4. Simulation Convergence Behaviour

Since the solver uses the L_1 norm of the objective function to determine convergence, it is important to find a suitable target residual. This is done by investigating the convergence behaviour of species of interest. In Figure 5.10, the relative changes in mass fractions are plotted against the residual norm. Here, the relative change compares the concentration of a species at the outlet for decade i and i-1. As such, it can be seen that the NO concentration at the outlet is continuously decreasing for a decreasing residual norm until the residual reaches a value of 10^{-7}. In general, it can be observed that the relative change in species mass fraction converges for all simulations when the residual norm is smaller than 10^{-8}, irrespective of CRN size or clustering criteria. While small changes in concentration can be achieved by decreasing the objective function further, this also results in longer simulation times. To be certain of convergence, in this work all presented simulations have a residual norm of at most 10^{-9}.

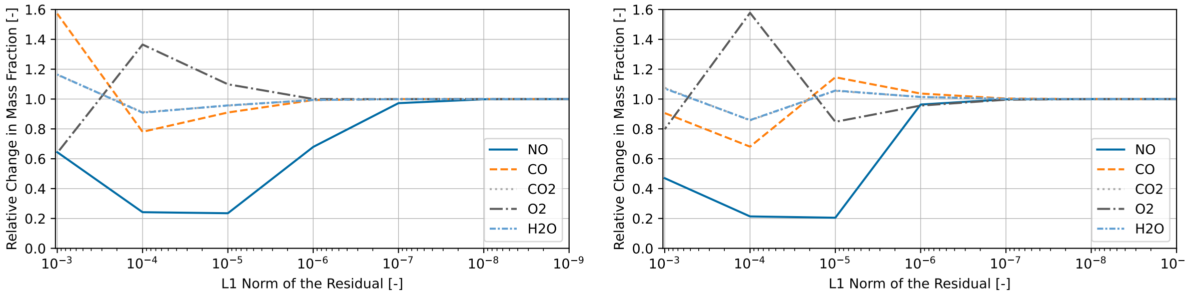

(a) 500 Reactors, Clustering I

(b) 2000 Reactors, Clustering I

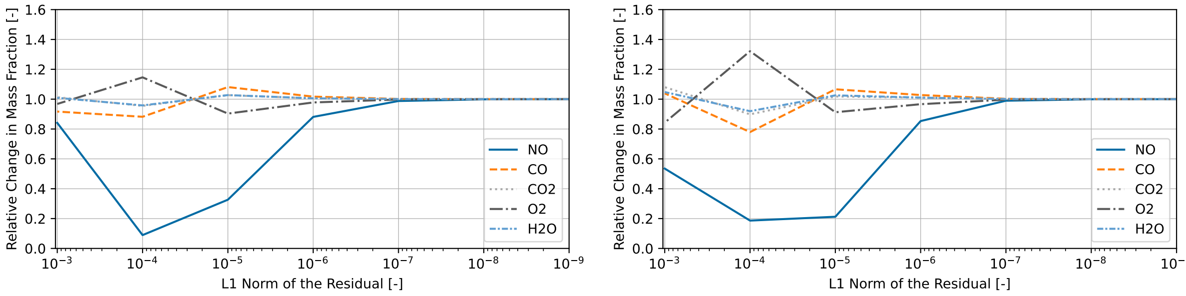

(c) 500 Reactors, Clustering II

(d) 2000 Reactors, Clustering II

Figure 5.10: Convergence behaviour of relevant species for 500 and 2000 reactor CRN at the outlet.

The simulation time is also strongly affected by the number of reactors in the CRN. The number of reactors chosen for a simulation is therefore a compromise between accuracy and simulation time. Figure 5.11 shows that the major species concentrations at the outlet are not strongly affected by the number of reactors. For CRN with 500 reactors or fewer, slight variations in species mass fractions are visible. Small CRN seem to adversely affect *clustering I* more. This could be due to the clustering criteria ”wasting” reactors downstream, resulting in poorer resolution where it is required. However, for CRN with 1000 reactors or more, the predicted major species emissions are virtually identical for both clustering criteria. Finally, variations in major species mass fractions on the order of parts per million are not of great interest. Therefore, CRN sizes of 1000 reactors or more should be adequate.

Small variations in mass fraction are of interest for NO emissions. As shown in Figure 5.12, the predicted NO emissions at the outlet are strongly affected, relatively speaking, by the number of reactors. In general, both clustering criteria show the same trend of decreasing NO emissions with increasing CRN size. This is mainly due to the thermal NO emissions decreasing with increasing CRN size. The higher NO emissions observed for *clustering I* cannot be solely attributed to the thermal pathway, but are also due to increased N_2O and prompt NO contributions.

Increasing the number of reactors beyond 2000 affects *clustering II* significantly less than *clustering I*. This is true for the thermal, prompt, and N_2O pathway. The latter two remain virtually constant for *clustering II* beyond 2000 reactors. The thermal pathway still decreases for both clustering criteria, but significantly less for *clustering II*. Finally, it seems that both clustering criteria converge for around 4000 reactors across all pathways. To be sure, additional simulations with larger CRN will have to

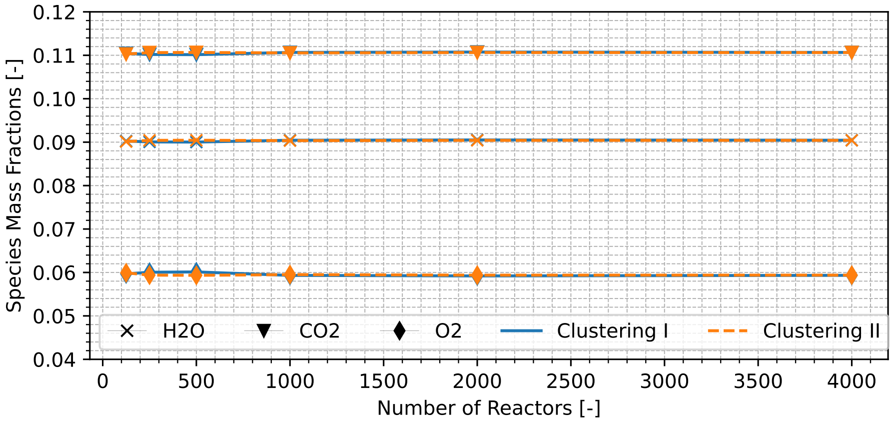

Figure 5.11: Effect of the number of reactors on major species concentrations at the outlet.

be performed in future work. The total simulation times of the different CRN sizes can be seen in

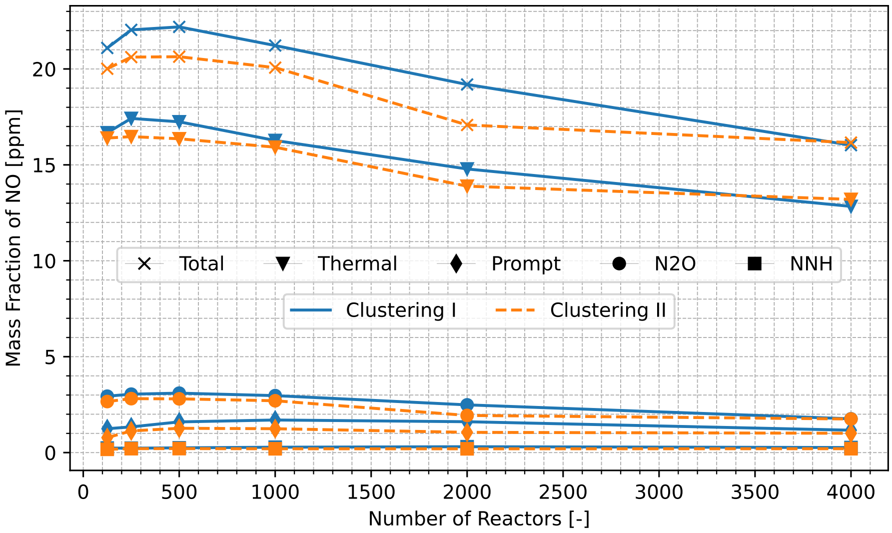

Figure 5.12: Effect of the number of reactors on total NO production in mass fraction (ppm) corrected for 15% oxygen.

Figure 5.13. It can be seen that the simulation time is strongly correlated to the size of the CRN. Increasing the number of reactors not only increases the computational time because more reactors need to be simulated, but it also increases the stiffness of the CRN. Interestingly, *clustering I* is less stiff for smaller CRN than *clustering II*. However, at 2000 reactors it seems to have become stiffer, taking slightly longer to simulate and significantly longer with 4000 reactors. Due to the long simulation time of the 4000 reactor CRN, it was decided not to use CRN larger than 2000 reactors in this work. CRN with a larger number of reactors are not a viable option with the current solver.

The reason for this can be seen in Figure 5.14, which shows the progression of the residual with respect to time. Typically, the initial residual of a CRN is on the order of 10^{-1}. As can be seen, the first decades progress relatively quickly. This is where the initial state of the reactors is flushed out of the system and replaced by a more appropriate state corresponding to the boundary conditions. With a more accurate state, the progression mainly slows down due to solely using a substitution solver. Integrating the now small residuals of the objective function only progresses reactors slowly. Ideally, this is when a line search method would be applied, as was done by *Cuoci et al.*[17].

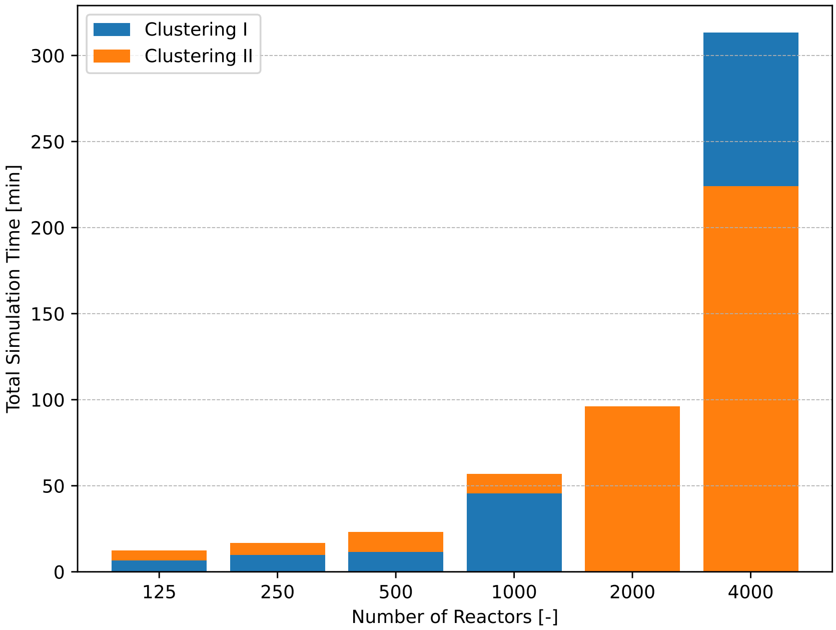

Figure 5.13: Effect of the number of reactors on the total computational time.

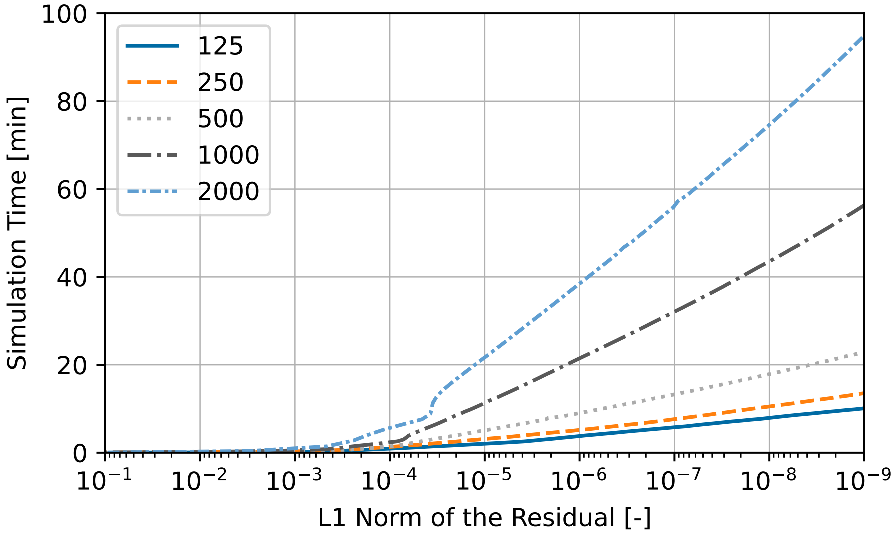

Figure 5.14: Decrease in residual vs time for a 125 reactors (solid blue line), 250 reactors (dashed orange line), 500 reactors (dotted grey line), 1000 reactors (dark dash dotted line), and 2000 reactors (short dash dotted light blue line)

6

NO Emissions Sensitivity Studies

This chapter presents and discusses the results of the performed sensitivity studies. The sensitivity of the NO emissions to the variations in temperature and density are discussed in Section 6.1 and Section 6.2, respectively. The effect of the equivalence ratio on the NO emissions is discussed in Section 6.3. Finally, the effect of hydrogen introduction on the NO emissions is investigated in Section 6.4. Supplementary plots for the sensitivity studies can be found in Appendix C. The sensitivity studies performed for temperature and density used CRN with 1,000 reactors due to time considerations at that time. As discussed in Subsection 5.2.4, this will result in slightly higher NO emissions compared to a 2000 reactor CRN otherwise used in this work.

6.1. Change in Temperature

The relationship between NO emissions and temperature is relatively trivial. An increase in temperature increases the production rate of any reaction, if reactants are available. Therefore, an increase in temperature should result in an increase in NO emissions, which can be seen in Figure 6.1. Yet, performing a temperature sensitivity study can indicate how susceptible the CRN emissions are to variations in temperature due to clustering or simplifications in the CFD simulation.

As shown in Figure 6.1, both clustering criteria show the same trend of exponential growth in NO emissions. Both clustering approaches also show the same trends for the relevant NO pathways. The increase in total NO emissions is driven by the thermal pathway. When the temperature decreases, the prompt pathway becomes a more prominent contributor. The prompt and N_2O pathways show a similar temperature sensitivity to each other, with both pathways being significantly less sensitive to temperature than the thermal pathway.

It can also be seen that for the NO emissions predicted by the CRN to reach the experimentally determined emissions on the order of 5 ppm, the overall temperature in the CRN would have to decrease by 10%. This is a rather large change in overall temperature, especially considering that the CRN should already have lower temperatures compared to the experimental setup, due to the lower equivalence ratio in the CFD simulation. While the aforementioned lack of a radiative heat loss model in the CFD simulation does result in higher temperatures, especially as the flow progresses downstream, it seems unlikely that it can solely explain the discrepancies between the CRN predictions and the experimentally determined emissions.

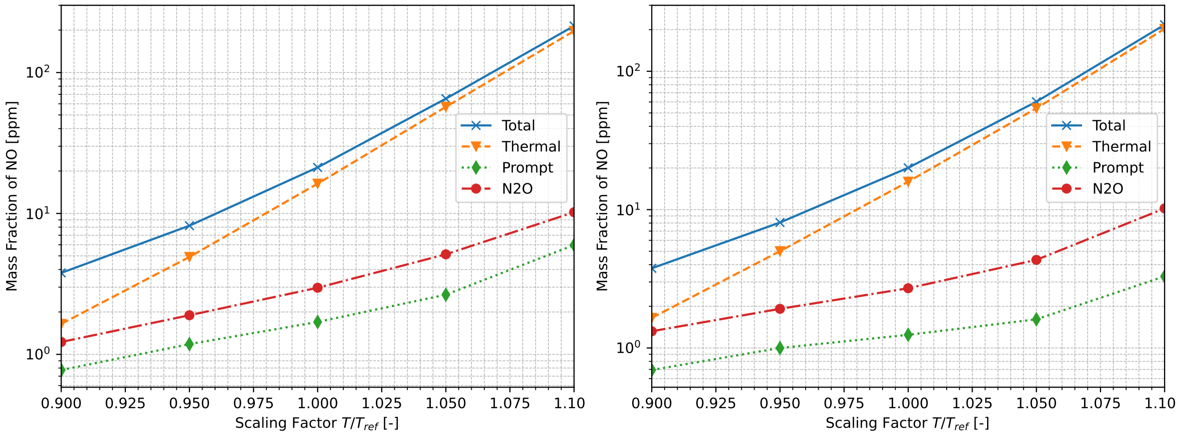

(a) Clustering I

(b) Clustering II

Figure 6.1: Change in NO concentration, corrected for 15% oxygen, due to temperature variation for 1000 reactor CRN.

Figure 6.2 shows the change in NO production of the relevant pathways throughout the domain. Interestingly, the increase in the production rate close to $y = 0.15\mathrm{m}$ is about an order of magnitude smaller than it is further downstream for the prompt and N_2O pathways. However, the temperature increase in those regions is virtually the same due to the lack of a radiation model. The reason for the limited increase in production rates is that the N_2O and prompt pathways are simply constrained by the availability of N_2O and the intermediate species of methane oxidation, respectively. This also means that for increasing temperatures, the contributions of both pathways are limited in the regions where they are most relevant, explaining the reduced temperature sensitivity observed in Figure 6.1.

A similar reasoning applies to the region around $y = 0.05\mathrm{m}$. Here, the thermal and prompt NO formation are limited by the concentrations of oxygen and OH. The restricted thermal and prompt NO productions affect the NO production through the N_2O pathway. The reason for this being that the CRN actually predicts that the vast majority of N_2O is formed through the dissociation of NO. Therefore, the limited NO production also limits the formation of N_2O.

Above $y = 0.2\mathrm{m}$, the three pathways show a similar change in production. However, here the prompt and N_2O pathways are only minor contributors. The thermal pathway shows the largest increase throughout the domain. The opposite is also true for a decrease in temperature. Here, the thermal pathway shows the largest decrease throughout the domain. The prompt and N_2O pathways show a smaller decrease in the same regions as discussed above.

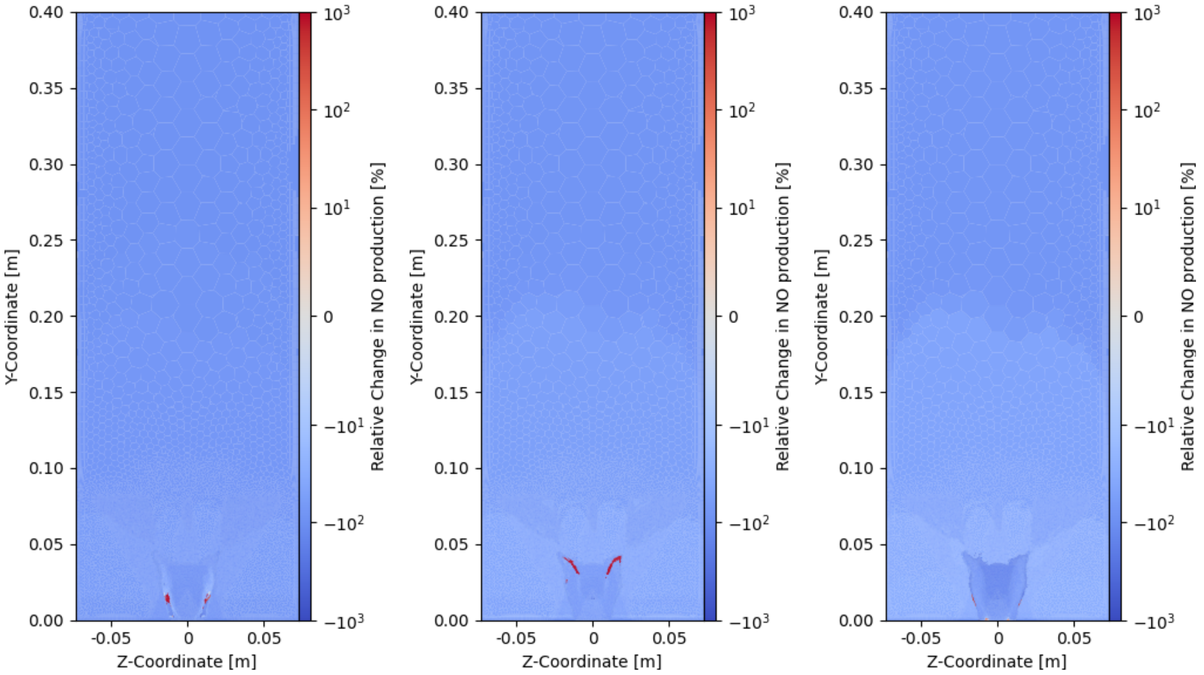

(a) Thermal, T = 95% **(b)** Prompt, T = 95% **(c)** N_2O, T = 95%

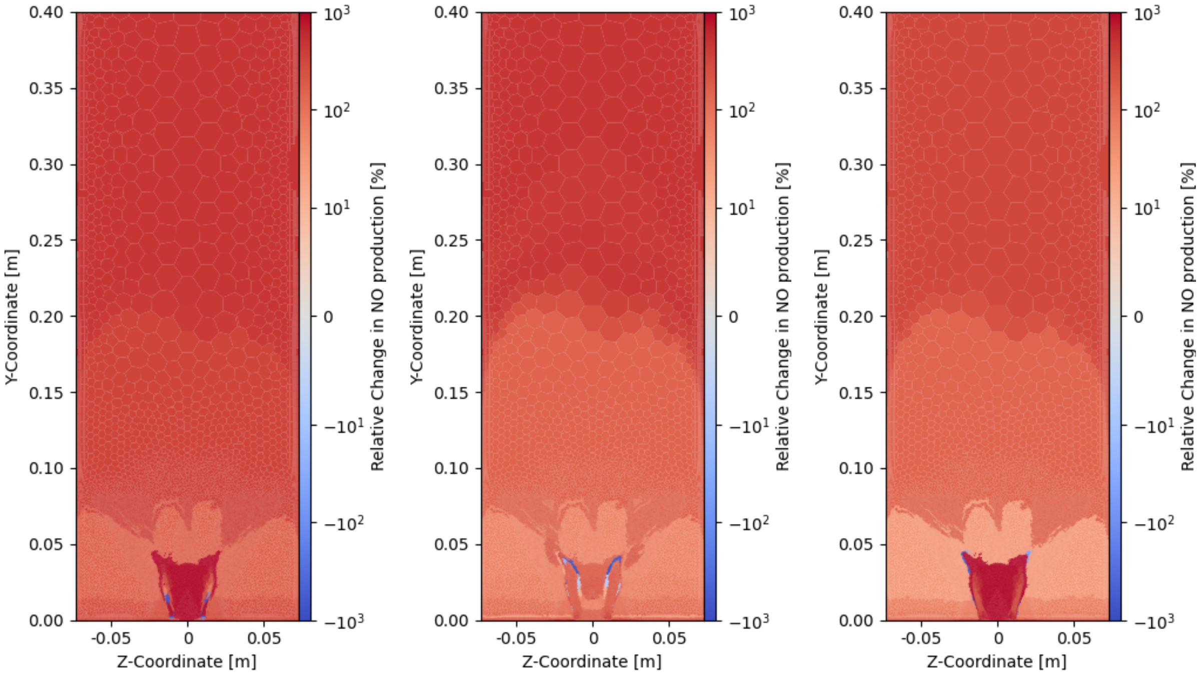

(d) Thermal, T = 105% **(e)** Prompt, T = 105% **(f)** N_2O, T = 105%

Figure 6.2: Relative change in the NO production of the relevant pathways for changing temperature parallel to the symmetry plane at x=$1\ \mathrm{mm}$ for a *clustering I*, 1000 reactor CRN.

6.2. Change in Density

The main mechanism through which density affects NO emissions is through molar concentrations. By increasing the density in a CV, the molar concentration of species also increases. Physically speaking, this increases the likelihood of collisions between particles. In the context of a numerical simulation, increasing the molar concentrations increases the reaction rates, as discussed in Section 2.1. Thus, one would expect increased NO production rates with increasing density.

With the thermal pathway being dominant, one might also want to consider how the residence time is affected by the change in density. Since the initial step in the thermal pathway is relatively slow, a larger residence time typically leads to higher emissions. In the case of the CRN, both the mass flows and the geometry of the reactors remain the same. Therefore, an increase in density must result in a decreased flow velocity. This, in turn, results in an increased residence time, making the residence time proportional to the density, $t_{res} \propto \rho$.

The effect of a change in density on the overall NO emissions can be seen in Figure 6.3. It shows that both clustering criteria exhibit the expected trend of increasing NO emissions with increasing density. However, *clustering I* does show a higher sensitivity to changes in density. This is mainly due to *clustering I* predicting higher thermal NO production in general, which shows the largest sensitivity to variations in density. Overall, the sensitivity to density is relatively low and shows linear behaviour in the selected range. A 10% variation results in a 4% and a 1.5% variation in NO for *clustering I* and *clustering II*, respectively.

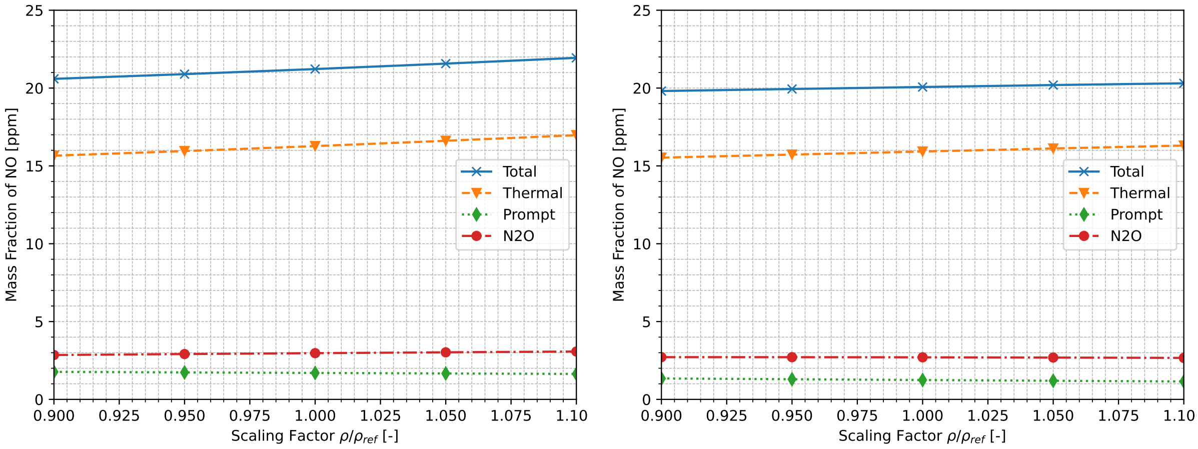

(a) Clustering I

(b) Clustering II

Figure 6.3: Change in NO concentration, corrected for 15% oxygen, due to variation in density for 1000 reactor CRN.

The effect on the NO pathways is shown in Figure 6.4 and Figure C.4. Looking at the three pathways, they mostly show the same behaviour for a change in density, barring the flame structure. It is also evident that the observed behaviour for a decrease in density is reversed for an increase in density. It should be noted that the regions affected the most are dominated by thermal NO, as discussed in Subsection 5.2.3. While the prompt and N_2O pathways show similar changes in production, their overall contribution in that region is minor.

The large relative changes in the flame structure are a numerical artifact. The NO production in those regions is essentially zero in the baseline case. The reason for the relative increase in thermal and N_2O production with decreasing density is due the baseline NO production be negligibly negative. Aside from the flame structure, the prompt and thermal pathway show very similar behaviour throughout the domain. The N_2O also shows similar behaviour, except for a region of increasing production with decreasing density and vice versa.

In the lower half ($y \approx 0.1\mathrm{m}$) of the domain, the prompt and thermal pathways show only a slight decrease in NO production for a decrease in density. In the top half of the domain, the NO decreases more sharply. This is likely due to the lower progression rates of reactions in the flame region at lower density. This results in a higher availability of intermediate species, such as O, OH, and H, downstream of the flame. This increased availability counteracts the effect of decreasing density in that region. Near the outlet, the majority of the intermediate species have reacted. As a result, the effect of the density is not counteracted to the same extent, resulting in a significant decrease in production.

The reason for the increased production of the N_2O pathway for a lower density is due to an increase in OH concentration. The increase in OH concentration is also due to the overall slower progression of combustion. The OH species forms N_2O through a collision with nitrogen, resulting in increased N_2O concentrations. In turn, this leads to an increased production of NO through the N_2O pathway. It can also be seen that the relative change in the N_2O pathway near the outlet is more significant than it is for the thermal and prompt pathways. This is due to the dissociation of NO in the region, as discussed in Section 6.1.

Comparing Figure 6.4 to Figure C.4, one can conclude that the same overall trends can be observed for *clustering I* and *clustering II*. It is notable that the region where the NO pathways are affected the most is significantly smaller for *Clustering II*. This is also the region where the thermal pathway is dominant, likely the reason for the increased sensitivity of *clustering I* observed in Figure 6.3.

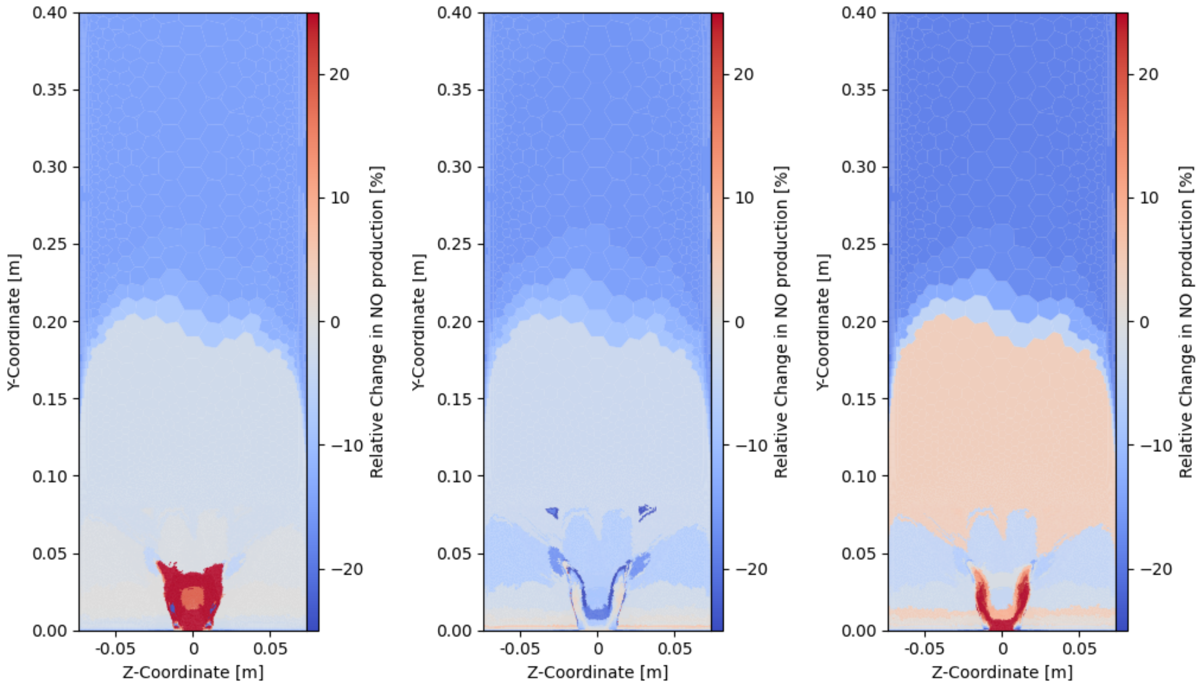

(a) Thermal, ρ = 90% **(b)** Prompt, ρ = 90% **(c)** N_2O, ρ = 90%

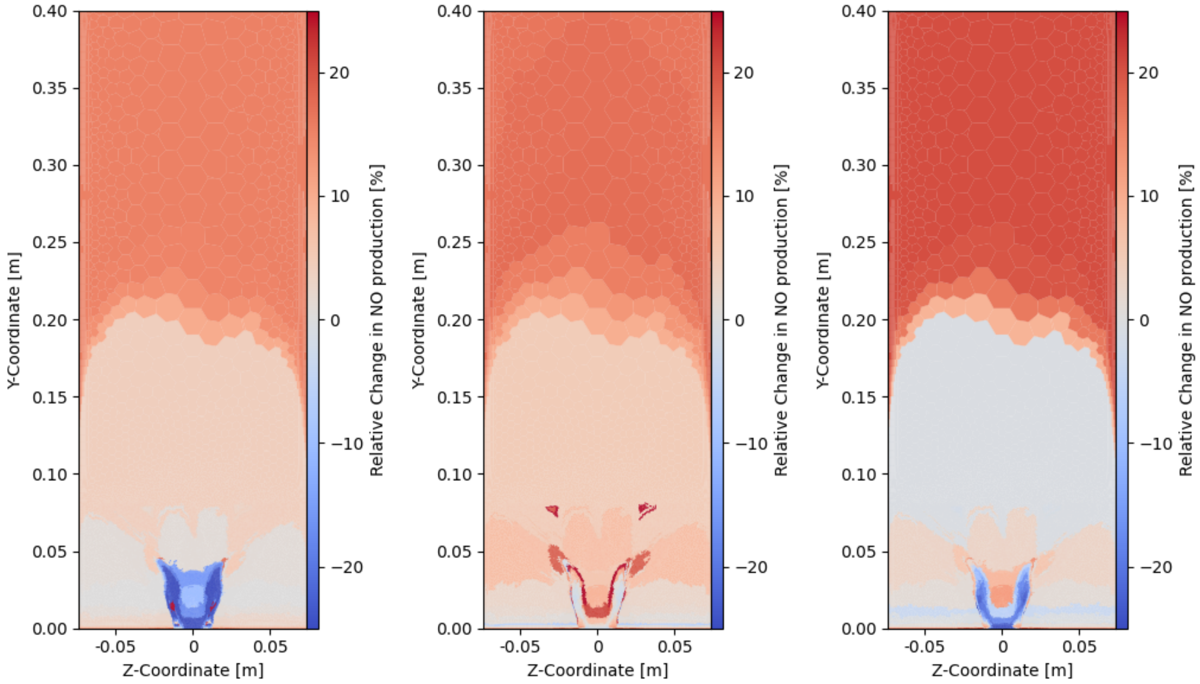

(d) Thermal, ρ = 110% **(e)** Prompt, ρ = 110% **(f)** N_2O, ρ = 110%

Figure 6.4: Relative change of the NO pathways for changing density parallel to the symmetry plane at x=$1\,\mathrm{mm}$ for a *clustering I*, 1000 reactor CRN.

6.3. Change in Equivalence Ratio

The effect of the equivalence ratio on the overall NO emissions can be seen in Figure 6.5. Both clustering criteria exhibit the same trends for the different NO pathways. The thermal pathway is mostly responsible for the observed trend for the total NO concentrations. However, the prompt and N_2O pathway also show a slight increase with increasing equivalence ratio. This is also visible through the slight divergence between the thermal and total NO curves. It should be noted that the temperature was kept constant for this sensitivity study. Normally, a change in equivalence ratio results in a change in adiabatic flame temperature, which affects emissions more strongly.

In general, the trends observed in Figure 6.5 show similarities to the trends observed for the density sensitivity in Section 6.2. Varying the equivalence ratio also affects the density of the reactors due to the change in mean molecular weight, which increases with a decreasing equivalence ratio. This is due to the higher molecular weight of oxygen and nitrogen. Thus, lowering the equivalence ratio increases the density. This means that density cannot explain the observed trend since it would predict increasing NO emissions with a decreasing equivalence ratio. Furthermore, the maximum observed difference in density between the largest and smallest equivalence ratios was $\approx 0.5\%$ with most reactors showing a difference closer to $\approx 0.1\%$. As shown in Figure 6.3, this should have a negligible impact on the NO emissions.

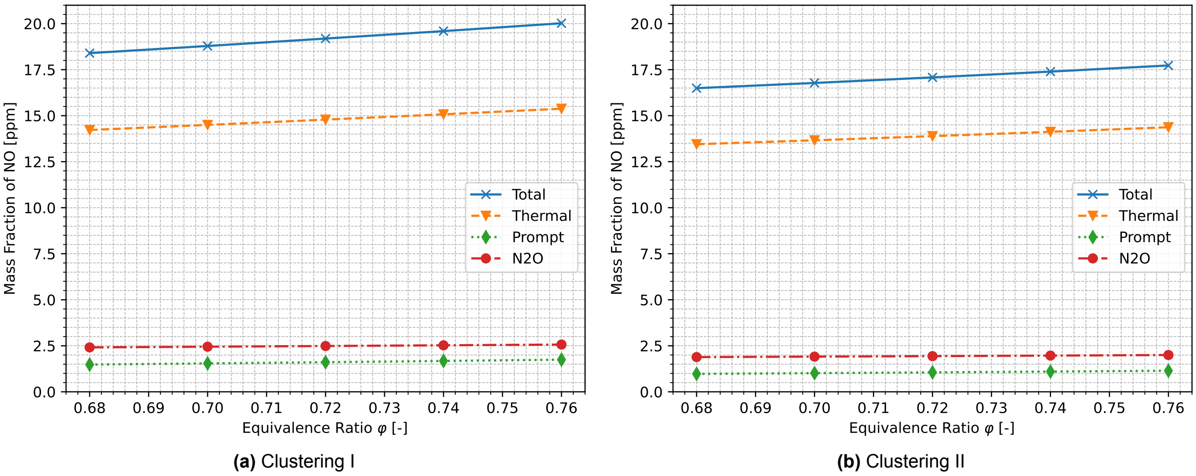

(a) Clustering I

(b) Clustering II

Figure 6.5: Change in NO concentration, corrected for 15% oxygen, due to variation in equivalence ratio for 2000 reactor CRN.

The effect on the pathways throughout the domain can be seen in Figure 6.6 and Figure C.7. It is evident that the thermal and N_2O pathway show a very similar behaviour. Looking at $\varphi = 0.68$ both pathways show increased NO production downstream of the flame with respect to the baseline simulation. They also show a region where the NO production remains almost constant. They do show a different behaviour close to the flame, where the thermal pathway predicts a decrease in NO production, which is not present for the N_2O pathway. This region of decrease for $\varphi = 0.68$ and increase $\varphi = 0.76$ is significant, as it dictates the trend for thermal NO shown in Figure 6.5.

Investigating the species important to thermal NO, it was found that the concentration of OH stays constant for a lower equivalence ratio. However, the concentration of atomic oxygen increases, specifically in the downstream region, see Figure C.8. In the region that shows constant thermal NO, the atomic oxygen also remains constant with equivalence ratio. Finally, in the region where the thermal pathway production decreases for $\varphi = 0.68$, the only relevant species that shows a decrease in concentration in that region is atomic nitrogen. The downstream increase in production of the N_2O pathway was found to be due to increased N_2O production through nitrogen related pathways.

Both the decrease in atomic nitrogen and atomic oxygen is caused by the faster oxidation of carbon species. The most important production of atomic nitrogen in that region stems from the reaction between CH and NO. There is less CH available due to faster oxidation and less NO available due to a decrease in prompt NO, as is visible in Figure 6.6b and Figure C.7b. As previously discussed, the prompt pathway is the largest source of NO in that region. The decrease in prompt NO is also due to faster oxidation.

Both *clustering I* and *clustering II* show the same trends for the individual pathways, as is evident from Figure 6.6 and Figure C.7. However, it is the case that the affected downstream area for N_2O and thermal NO is larger for *clustering I* than for *clustering II*. Conversely, the region that affects the prompt pathway is larger for *clustering II*.

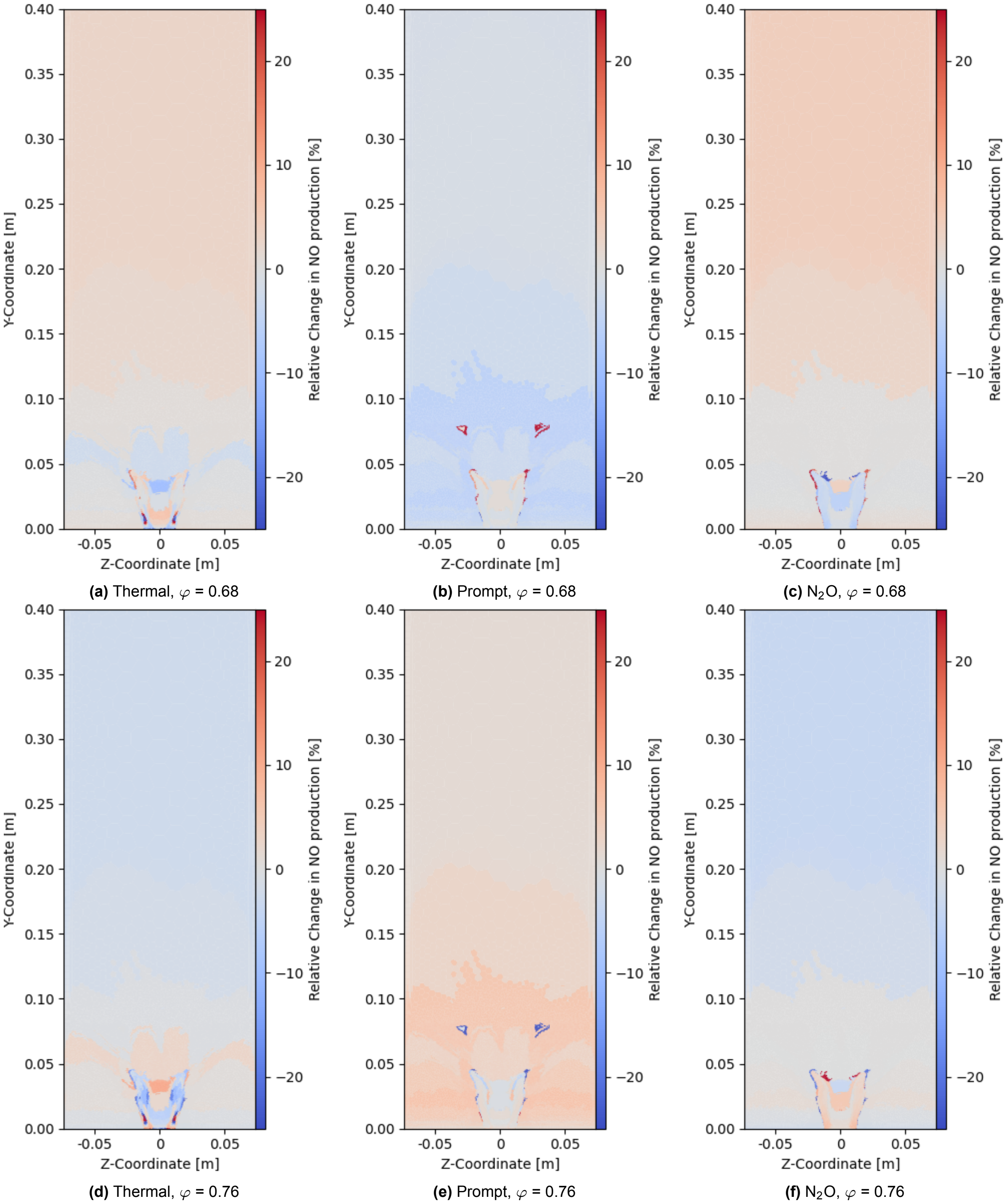

(a) Thermal, φ = 0.68 **(b)** Prompt, φ = 0.68 **(c)** N_2O, φ = 0.68

(d) Thermal, φ = 0.76 **(e)** Prompt, φ = 0.76 **(f)** N_2O, φ = 0.76

Figure 6.6: Relative change of the NO pathways for changing equivalence ratio, parallel to the symmetry plane at x=$1\,\mathrm{mm}$ for a *clustering I*, 2000 reactor CRN.

6.4. Effect of H_2 Addition to the Fuel Stream

The change in NO emissions as a result of introducing hydrogen in the fuel mixture can be seen in Figure 6.7. It shows that the NO concentration decreases substantially with increasing hydrogen mole fraction. It can also be seen that all pathways decrease in production with increasing hydrogen mole fraction, with the decrease in thermal pathway being dominant. Again, both clustering criteria show the same trends. However, it can also be seen that *clustering I* shows a significantly larger decrease in NO emissions compared to *clustering II*. This is true for all the NO pathways.

Introducing hydrogen at constant power decreases both the equivalence ratio and the density in the CRN. For $X_{H_2} = 0.8$, the equivalence ratio is $\varphi = 0.65$, which should lead to a slight decrease in NO production, as can be extrapolated from Figure 6.5. At the same mole fraction, the largest observed decrease in density is $\approx 10\%$ at the inlet of the combustion chamber. The decrease is $\approx 5\%$ in the rest of the domain. This should also result in a modest decrease in NO emissions, as visible in Figure 6.3. Since both a decrease in equivalence ratio and a decrease in density reduce NO production mainly through the thermal pathway, they might be partially responsible for the observed reduction in the thermal pathway in Figure 6.7

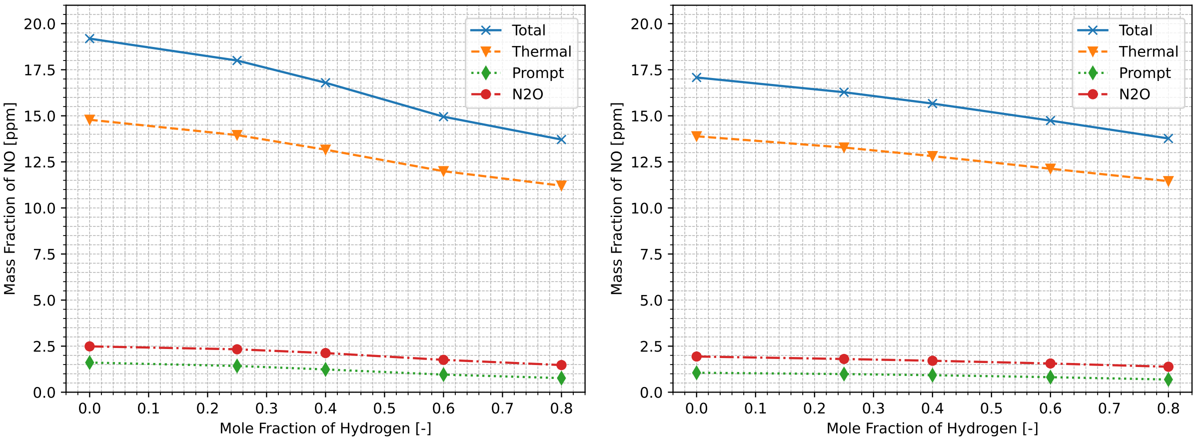

(a) Clustering I **(b)** Clustering II

Figure 6.7: Change in NO concentration, corrected for 15% oxygen, due to the introduction of hydrogen 2000 reactor CRN.

The effect of a hydrogen mole fraction of 0.25 on the NO pathways can be seen in Figure 6.8 and Figure C.9. As one would expect, the prompt pathway shows a sharp decrease in production in the region where it is also most relevant to the overall NO production, see Subsection 5.2.3. This is simply due to the introduction of hydrogen decreasing the amount of available methane, which strongly affects the prompt pathway.

The thermal and N_2O pathways show a very similar pattern to the $\varphi = 0.68$ plots in Section 6.3, aside from the flame structure. As was the case for a decreasing equivalence ratio, the top half of the domain shows an increase in NO production that tapers off into a decrease in NO production toward the inlet of the domain. However, the magnitudes of the changes in NO production are different, especially considering that $X_{H_2} = 0.25$ corresponds to an equivalence ratio of $\varphi = 0.71$. Specifically, the decrease in NO production in the lower half is much larger than can be explained by the slight decrease in equivalence ratio. Furthermore, the N_2O shows a substantial area of decreased production, which was not the case for $\varphi = 0.68$ in Section 6.3

The more severe decrease in thermal NO production coincides again with an area that experiences lower atomic nitrogen concentrations. The most relevant source of atomic nitrogen in that region is the aforementioned reaction between (prompt) NO and CH. Both the decrease in NO and CH concentrations in that region are due to the lower methane mole fraction in the fuel. The less severe decrease in thermal NO coincides with a region of lower atomic oxygen concentrations compared to the baseline case. The decrease in atomic oxygen is likely due to the higher reactivity of hydrogen combustion, which increases the consumption of the available atomic oxygen.

For the N_2O pathway, the decrease in production near the inlet can be attributed to lower concentrations of atomic hydrogen and intermediate species of methane combustion. This results in lower

N_2O production rates through pathways with NCO and NH. The slight increase near the outlet can be attributed to nitrogen related pathways, as was the case in Section 6.3.

Comparing Figure 6.8 to Figure C.9, it can again be concluded that both clustering criteria predict the same overall behaviour of the individual NO pathways. It is notable that *clustering II* exhibits a substantial decrease in prompt NO in a larger area than *clustering I*. Comparing Figure 5.9c and Figure B.1c, one can see that *clustering II* predicts larger areas of lower prompt NO production in general. However, *clustering II* does predict the largest prompt NO production in the centre of the flame. Since the most notable prompt production is very localised, this also localises the most substantial reduction in thermal NO for *clustering II*. This could be the reason for the smaller decrease in thermal NO observed in Figure 6.7.

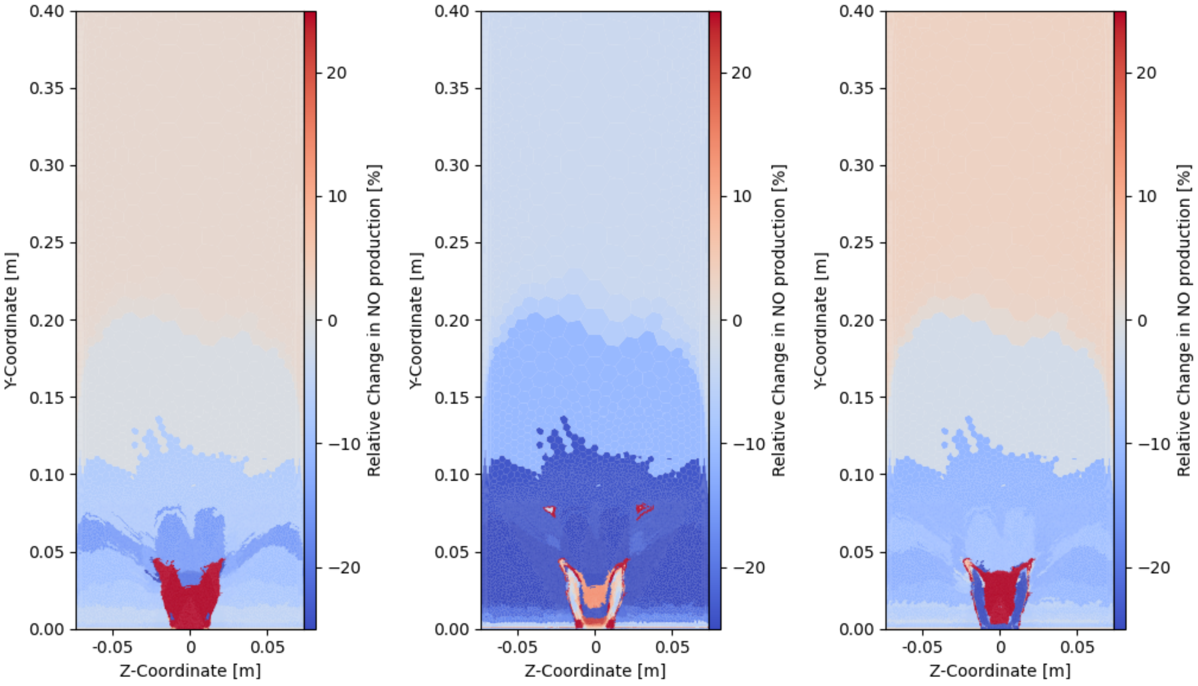

(a) Thermal **(b)** Prompt **(c)** N_2O

Figure 6.8: Relative change of the NO pathways for $X_{H_2} = 0.25$ parallel to the symmetry plane at x=$1\ \mathrm{mm}$ for a *clustering I*, 2000 reactor CRN.

6.5. Comparing Sensitivity Studies to Experimental Results

The trends observed in the performed sensitivity studies do not align with experimental observations. Link et al. [8]. found that increasing the hydrogen mole fraction leads to an increase in NO emissions. As discussed, increasing the hydrogen mole fraction at constant power decreases the density and the equivalence ratio. The used CRN methodology predicts that both changes result in lower NO emissions. For the equivalence ratio, this does not take into account that the adiabatic temperature would decrease as well in reality, which would further decrease NO emissions.

The CRN also predicts that introducing hydrogen into the fuel stream decreases NO emissions. While the decrease in the thermal pathway might partially be due to the decrease in density and equivalence ratio, it mostly decreases due to a reduction in intermediate species of methane oxidation. Furthermore, the prompt and N_2O pathways also decrease with increasing hydrogen mole fraction. Thus, the CRN predicts that the introduction of hydrogen decreases NO emissions, regardless of density and equivalence ratio changes.

The only sensitivity study that can explain the experimentally observed trend, according to the CRN, is a change in temperature. Introducing hydrogen could lead to more locally elevated equivalence ratios, as also visible in Section 5.2, due to the increased diffusivity of hydrogen. These elevated equivalence ratios would lead to locally elevated temperatures, compared to the adiabatic temperature. Since thermal NO was found to be extremely sensitive to small changes in temperature, its increase due to locally elevated temperatures could negate the observed decrease in overall NO discussed above. The simplified approach of using a single CFD simulation for pure methane combustion does not capture this phenomenon, since it does not capture the change in the flow field.

7

Conclusions and Recommendations

7.1. Conclusions

The aim of this work was to investigate the NO emissions of the APPU burner under varying operating conditions using an automatic CFD-CRN approach. To do so, a new solver architecture was implemented. The new solver was verified using available simulations of the previously investigated Sandia Flame D. The CRNs used to investigate the APPU burner were based on a single RANS CFD simulation, which simulated pure methane combustion at slightly different operating conditions than those of the physical experiments. The CRNs used were generated using two different clustering approaches. The main difference between the clustering being that *clustering I* constrained the height of the reactors in an attempt to obtain radial resolutions. Both *clustering I* and *clustering II* used the temperature and mean mixture fraction as clustering constraints.

In order to answer the research questions, the baseline case was investigated first. For this, the CRN used the same operating conditions as the CFD simulation. The baseline case showed that, for the current clustering approach, a high number of reactors is required to resolve the temperature field near the flame with acceptable resolution. It also showed that the CRNs predict the concentrations of the major species at the outlet well. However, it also showed that local variations in equivalence ratio, present in the CFD simulation, were not predicted by the CRN. It could also be concluded that the NO emissions predicted by the CRN, were much closer to the experimental values than the NO emissions estimated by the post-processing function applied to the CFD simulation results. Finally, it was found that the thermal pathway is the most relevant NO producer, with the prompt and N_2O pathways also being non-negligible. The NNH pathway was found to be mostly irrelevant. It was also discovered that thermal NO production is still relevant in the flue gas.

Next, the effect of the number of reactors and the clustering criteria on the results of the baseline case were investigated. It was found that the concentration of the major species at the outlet was not strongly affected by the number of reactors or the clustering criteria. However, the NO emissions at the outlet were found to be significantly affected by both the number of reactors and the clustering criteria. It was found that *clustering I* predicted higher NO emissions for every CRN size. Both clustering criteria showed the same trend of decreasing NO emissions with increasing CRN size. However, it was decided to limit the CRN size to 2000 reactors due to the stark increase in computational time for larger CRN.

Finally, the operating conditions were varied. In this work, the equivalence ratio, the temperature, the density, and the fuel composition were changed. For the temperature and density, the relevant parameter was multiplied by a scaling factor for each reactor. This was done without changing the mass flows. For the equivalence ratio, the fuel flow was kept constant and the air mass flow was modified, also affecting the mass flows of the reactors. Similarly, for the fuel composition, the fuel flow was decreased to maintain the original combustion power of the CFD simulation, whilst increasing the hydrogen mole fraction.

The density sensitivity analysis showed that NO emissions increased linearly with increasing density. This was evident for both clustering criteria. However, *clustering I* showed larger changes in NO emissions than *clustering II*. While the prompt, thermal, and N_2O pathways showed the same pattern of the largest variation in NO production being found in the upper half of the domain, the thermal pathway was found to be responsible for the observed increase in NO production. This is due to the thermal pathway being dominant in the upper region. For *clustering I* this upper region was significantly larger, likely explaining the increased sensitivity. Since the density also affects the residence time proportionally, one could say that in the CRN an increase in residence time results in increased NO emissions.

The equivalence ratio sensitivity analysis also showed a linear increase in NO emissions with increasing equivalence ratio. Both clustering criteria showed very similar relative trends in NO emissions, with the thermal pathway being the trendsetter. The production of the thermal and N_2O pathways were inversely proportional in the vast majority of the domain. This was due to the concentrations of atomic oxygen and nitrogen in the domain. The production of prompt NO was proportional to the equivalence ratio due to the increased concentration of species related to incomplete combustion. Both clustering criteria showed very similar patterns for the pathways.

The investigation of hydrogen introduction revealed a trend of decreasing NO emissions with increasing mole fractions of hydrogen. The decrease in NO was significant and observable for both clustering criteria. It was also evident that *clustering I* showed a more significant decrease in NO emissions than *clustering II*. The main reason for the decrease in NO was the effect of hydrogen introduction on the thermal pathway. The decrease in methane concentration affected atomic nitrogen pathways, which, in turn, affected the thermal pathway. The prompt pathway also showed a decrease in production, which was simply due to the decrease in methane concentration. Finally, the N_2O pathway showed a decrease in production due to decreased N_2O production through intermediate species of methane combustion.

The temperature sensitivity study showed that NO emissions are very sensitive to temperature. Both clustering criteria showed a very similar exponential trend. Interestingly, the increase in temperature affected the pathways to different extents. The thermal pathway was affected the most across the entire domain. The prompt and N_2O pathways showed the highest increase in production in the region where they are less relevant. In the areas where they are relevant contributors to the overall NO production, they showed a substantially smaller increase in production with temperature. The reason for the reduced production increase is thought to be due to a bottleneck in species availability. The same pattern can be observed for both clustering criteria.

The current CRN methodology cannot reproduce the experimental observations, which show a clear trend of increasing NO emissions with increasing hydrogen mole fraction. The performed sensitivity studies for equivalence ratio, density, and introduction of hydrogen all predict a decrease in NO production. The reason for the increased NO emission could be due to locally elevated temperatures as a result of the increased diffusivity of hydrogen. This phenomenon is not captured in the current CRN approach.

7.2. Recommendations

While the used CRN methodology predicted reasonable NO emissions compared to experimental results for the baseline case, it did not manage to predict the experimentally observed behaviour of the NO emissions as a result of hydrogen introduction. As such, the following recommendations are made for similar research in the future.

Mean Mixture Fraction

In this work, the mean mixture fraction was used as a clustering criterion. This was done to capture the mixing behaviour in the mixing tube. However, this adversely affects the resolution in the combustion chamber. It was found that the clustering approach caused a substantial number of reactors to be in the mixing tube. This means that for a set number of reactors, fewer reactors are available to be placed in the combustion chamber. It is therefore recommended to remove the mean mixture fraction from the clustering criteria. It would be of interest to investigate the effect this has on the sensitivity of the NO emission to the CRN size.

Line Solver

The current solver architecture employs only a substitution solver. As was discussed, it works well when the residual is large. When the residual is smaller, the convergence speed of the substitution solver decreases substantially. It is therefore recommended to develop a line search solver, as was used in previous iterations of AGNES. During this research, the implementation of a line search solver was not successful, which leads to longer simulation times. This restricts the number of reactors that can be used and the number of simulations that can be run.

Energy Equation

The current solver is not capable of solving the energy equation. As a result, the temperature of the reactors is purely derived from the CFD results. The temperature of the reactors can be changed manually, as was done in the temperature sensitivity study, but it is not affected by the chemical state of the reactor. By solving the energy equation, the effect of a change in equivalence ratio, density, and hydrogen mass fraction on the temperature can be modelled. This could lead to more realistic results for varying operating conditions when using a single CFD simulation.

CFD Simulation

In this study, the CRN, under various operating conditions, were all based on a single CFD simulation. This approach is tempting, since it reduces the need for multiple CFD simulations. However, this approach does not capture the effect of the operating conditions on the flow. In the future, to improve the results, it could be of interest to use CFD results at different operating conditions and interpolate between them using CRNs. This approach still limits the number of CFD simulations required, but would result in fewer simplifications. This approach is also preferable to only solving the energy equation, as discussed above, since the CFD simulations would model both the flow and the temperature.

Bibliography

[1] N. Marszałek and T. Lis. “The future of sustainable aviation fuels”. In: *Combustion Engines* (Mar. 2022). ISSN: 2300-9896, 2658-1442. DOI: `10.19206/CE-146696`.

[2] Airbus. *Global Market Forecast 2023-2042*. URL: `https://www.airbus.com/en/products-services/commercial-aircraft/market/global-market-forecast` (visited on 26/03/2024).

[3] V. Grewe et al. “Evaluating the climate impact of aviation emission scenarios towards the Paris agreement including COVID-19 effects”. en. In: *Nature Communications* 12.1 (June 2021), p. 3841. ISSN: 2041-1723. DOI: `10.1038/s41467-021-24091-y`.

[4] *The Paris Agreement - Publication*. `https://unfccc.int/documents/184656`. Accessed: 2024-03-26. Nov. 2018.

[5] *Annex 16 - Environmental Protection. Volume IV - Carbon Offsetting and Reduction Scheme for International Aviation (CORSIA)*. 2nd edition. Montréal, Québec, Canada: ICAO, 2023. ISBN: 978-92-9275-117-3.

[6] D. European Commission and Directorate-General for Mobility and Transport. “Flightpath 2050 – Europe’s vision for aviation – Maintaining global leadership and serving society’s needs”. In: (2011). `http://dx.doi.org/doi:10.2777/50266`.

[7] A. Baroutaji et al. “Comprehensive investigation on hydrogen and fuel cell technology in the aviation and aerospace sectors”. In: *Renewable and Sustainable Energy Reviews* 106 (2019), pp. 31–40. ISSN: 1364-0321. DOI: `https://doi.org/10.1016/j.rser.2019.02.022`.

[8] S. Link et al. “Experimental analysis of dual-fuel (CH4/H2) capability in a partially-premixed swirl stabilized combustor”. In: *International Journal of Hydrogen Energy* 101 (2025), pp. 427–437. ISSN: 0360-3199. DOI: `https://doi.org/10.1016/j.ijhydene.2024.12.286`.

[9] S. Link et al. “Experimental investigation of the NO emission characteristics in swirl-stabilized technically premixed CH4/H2 flames”. In: *Proceedings of the Combustion Institute* 41 (2025), p. 105964. ISSN: 1540-7489. DOI: `https://doi.org/10.1016/j.proci.2025.105964`.

[10] Q. Yang, P. Zhao and H. Ge. “reactingFoam-SCI: An open source CFD platform for reacting flow simulation”. In: *Computers and Fluids* 190 (Aug. 2019), pp. 114–127. ISSN: 00457930. DOI: `10.1016/j.compfluid.2019.06.008`.

[11] H. Khodayari, F. Ommi and Z. Saboohi. “A review on the applications of the chemical reactor network approach on the prediction of pollutant emissions”. In: *Aircraft Engineering and Aerospace Technology* 92 (4 Apr. 2020), pp. 551–570. ISSN: 17488842. DOI: `10.1108/AEAT-08-2019-0178`.

[12] S. Trespi et al. “Development and application of an efficient chemical reactor network model for oxy-fuel combustion”. In: *Energy and Fuels* 35 (9 May 2021), pp. 7121–7132. ISSN: 15205029. DOI: `10.1021/acs.energyfuels.0c03560`.

[13] G. Babazzi et al. “NOX emissions predictions for a hydrogen micromix combustion system”. In: *Proceedings of the ASME Turbo Expo*. Vol. 3. American Society of Mechanical Engineers (ASME), 2019. ISBN: 9780791858608. DOI: `10.1115/GT2019-90532`.

[14] S. Chaturvedi et al. “Prediction of NOx emissions and pathways in premixed ammonia-hydrogen-air combustion using CFD-CRN methodology”. In: *Journal of the Energy Institute* 111 (Dec. 2023). ISSN: 17460220. DOI: `10.1016/j.joei.2023.101406`.

[15] R. F. Monaghan et al. “Detailed multi-dimensional study of pollutant formation in a methane diffusion flame”. In: *Energy and Fuels* 26 (3 Mar. 2012), pp. 1598–1611. ISSN: 15205029. DOI: `10.1021/ef201853k`.

[16] I. ANSYS. *ANSYS Fluent*. Version 2023 R2. Computational Fluid Dynamics (CFD) software. ANSYS, Inc. 2023.

[17] A. Cuoci et al. “Numerical modeling of NOx formation in turbulent flames using a kinetic post-processing technique”. In: *Energy and Fuels* 27 (2 Feb. 2013), pp. 1104–1122. ISSN: 08870624. DOI: `10.1021/ef3016987`.

[18] R. Sampat. “Automatic generation of Chemical Reactor Networks for Combustion Simulations”. MA thesis. Delft University of Technology, 2018.

[19] A. Stagni et al. “A fully coupled, parallel approach for the post-processing of CFD data through reactor network analysis”. In: *Computers and Chemical Engineering* 60 (Jan. 2014), pp. 197–212. ISSN: 00981354. DOI: `10.1016/j.compchemeng.2013.09.002`.

[20] M. D. de Wit. “The Effect of Solving the Energy Equation on Combustion Simulation using Automatically Generated Chemical Reactor Networks”. MA thesis. Delft University of Technology, 2019.

[21] P. Sutar. “Coupled Time Integration and Globalized Newton’s Method for Faster Solution of Chemical Reactor Networks”. MA thesis. Delft University of Technology, 2021.

[22] R. Barlow and J. Frank. “Effects of turbulence on species mass fractions in methane/air jet flames”. In: *Symposium (International) on Combustion* 27.1 (1998). Twenty-Seventh Sysposium (International) on Combustion Volume One, pp. 1087–1095. ISSN: 0082-0784. DOI: `https://doi.org/10.1016/S0082-0784(98)80510-9`.

[23] R. S. Barlow and J. H. Frank. *Sandia/TUD Piloted CH4/Air Jet Flames*. International Workshop on Measurement and Computation of Turbulent Flames (TNF). 2003. URL: `https://tnfworkshop.org/data-archives/pilotedjet/ch4-air/` (visited on 17/03/2026).

[24] S. R. Turns. *An introduction to combustion: concepts and applications*. 3rd ed. OCLC: ocn660161844. New York: McGraw-Hill, 2012. ISBN: 9780073380193.

[25] G. P. Smith et al. `http://www.me.berkeley.edu/gri_mech/`. Accessed: 2024-08-04.

[26] U. of California. *Chemical-Kinetic Mechanisms for Combustion Applications*. San Diego Mechanism web page, Mechanical and Aerospace Engineering (Combustion Research). Accessed: 2025-03-18. 2016.

[27] G. Smith, Y. Tao and H. Wang. *Foundational Fuel Chemistry Model Version 1.0 (FFCM-1)*. Accessed: 2025-03-19. 2016.

[28] P. Glarborg et al. “Modeling nitrogen chemistry in combustion”. In: *Progress in Energy and Combustion Science* 67 (July 2018), pp. 31–68. ISSN: 03601285. DOI: `10.1016/j.pecs.2018.01.002`.

[29] ”. Rezvani”. “”A Conceptual Methodology for the Prediction of Engine Emissions””. PhD thesis. ”Atlanta, GA, USA”: ”Georgia Institute of Technology”, ”2010”.

[30] M. Nozari et al. “Emission and performance of a micro gas turbine combustor fueled with ammonia-natural gas”. In: *International Journal of Engine Research* (2022). ISSN: 20413149. DOI: `10.1177/14680874211005052`.

[31] ANSYS, Inc. *ANSYS Fluent User’s Guide*. 2009. URL: `https://www.afs.enea.it/project/neptunius/docs/fluent/html/ug/node1461.htm` (visited on 22/03/2026).

[32] E. F. Moore. “The Shortest Path Through a Maze”. In: *Proceedings of the International Symposium on the Theory of Switching*. Harvard University Press, 1959, pp. 285–292.

[33] D. G. Goodwin et al. *”Cantera: An Object-oriented Software Toolkit for Chemical Kinetics, Thermodynamics, and Transport Processes”*. ”`https://www.cantera.org`”. ”Version 3.0.0”. 2023. DOI: `10.5281/zenodo.8137090`.

[34] P. Virtanen et al. “SciPy 1.0: fundamental algorithms for scientific computing in Python”. In: *Nature Methods* 17 (3 Mar. 2020), pp. 261–272. ISSN: 15487105. DOI: `10.1038/s41592-019-0686-2`.

[35] G. D. Byrne and A. C. Hindmarsh. “A Polyalgorithm for the Numerical Solution of Ordinary Differential Equations”. In: *ACM Transactions on Mathematical Software (TOMS)* 1 (1 Mar. 1975), pp. 71–96. ISSN: 15577295. DOI: `10.1145/355626.355636`.

[36] A. A. V. Perpignan. “Emission Modelling from a Multi-Fuel Dual Combustor Gas Turbine”. In: *Research Repository (Delft University of Technology)* (Feb. 2020). DOI: `10.4233/uuid:094af2d0-3fb0-4067-9706-888592d15760`.

[37] ANSYS, Inc. *ANSYS Fluent Documentation. NOx Modeling in ANSYS FLUENT*. URL: `https://www.afs.enea.it/project/neptunius/docs/fluent/html/th/node210.htm` (visited on 16/06/2026).

A

Supplemental Plots Solver Verification

A.1. Axial location x/d = 30

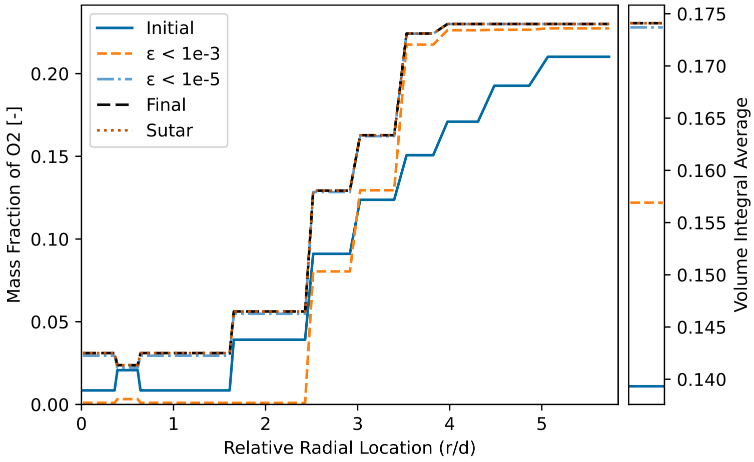

Figure A.1: Radial plot of Y_{O_2} at axial location x/d = 30 for a 1000 reactor CRN, with the initial CRN state (the solid blue line), CRN state at $\varepsilon < 10^{-3}$ (short orange dashes), CRN state at $\varepsilon < 10^{-5}$ (light blue dash-dotted line), final CRN state (long black dashes), and final result from Sutar [21] (dotted red line).

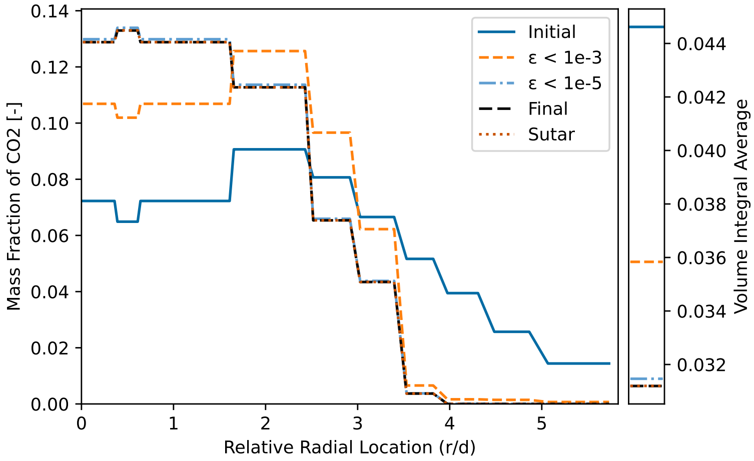

Figure A.2: Radial plot of Y_{CO_2} at axial location x/d = 30 for a 1000 reactor CRN, with the initial CRN state (the solid blue line), CRN state at $\varepsilon < 10^{-3}$ (short orange dashes), CRN state at $\varepsilon < 10^{-5}$ (light blue dash-dotted line), final CRN state (long black dashes), and final result from Sutar [21] (dotted red line).

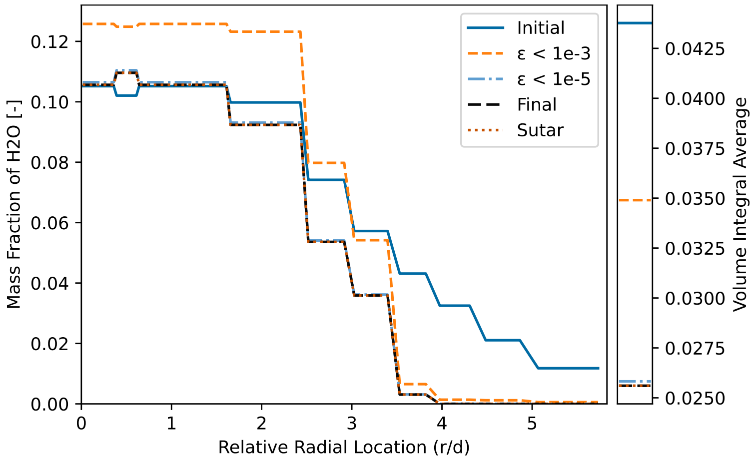

Figure A.3: Radial plot of Y_{H_2O} at axial location x/d = 30 for a 1000 reactor CRN, with the initial CRN state (the solid blue line), CRN state at $\varepsilon < 10^{-3}$ (short orange dashes), CRN state at $\varepsilon < 10^{-5}$ (light blue dash-dotted line), final CRN state (long black dashes), and final result from Sutar [21] (dotted red line).

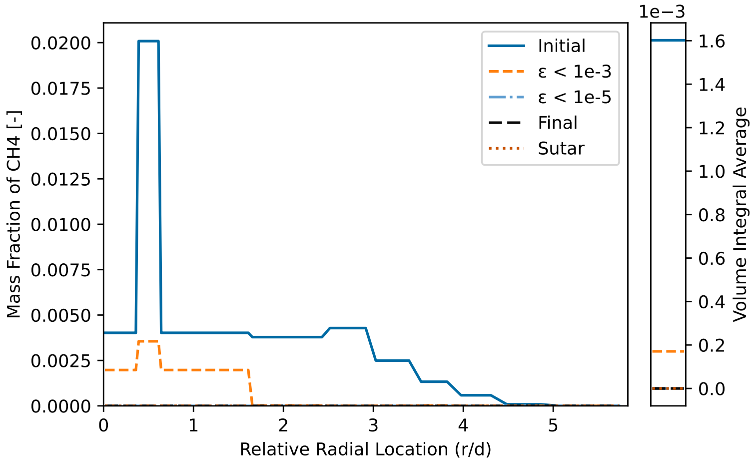

Figure A.4: Radial plot of Y_{CH_4} at axial location x/d = 30 for a 1000 reactor CRN, with the initial CRN state (the solid blue line), CRN state at $\varepsilon < 10^{-3}$ (short orange dashes), CRN state at $\varepsilon < 10^{-5}$ (light blue dash-dotted line), final CRN state (long black dashes), and final result from Sutar [21] (dotted red line).

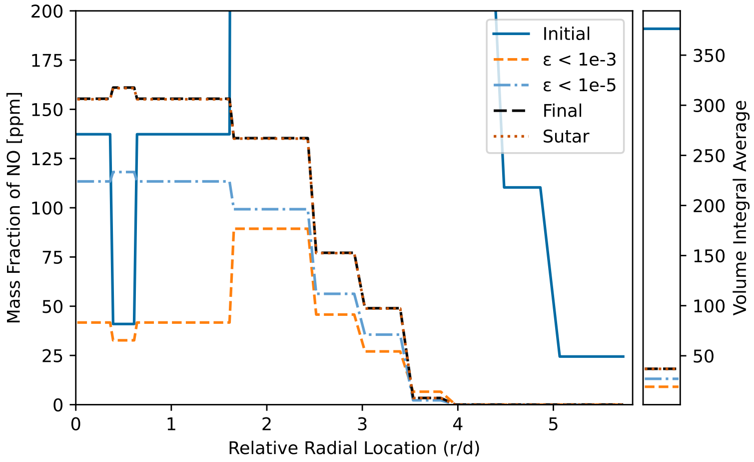

Figure A.5: Radial plot of Y_{NO} at axial location x/d = 30 for a 1000 reactor CRN, with the initial CRN state (the solid blue line), CRN state at $\varepsilon < 10^{-3}$ (short orange dashes), CRN state at $\varepsilon < 10^{-5}$ (light blue dash-dotted line), final CRN state (long black dashes), and final result from Sutar [21] (dotted red line).

A.2. Axial location x/d = 45

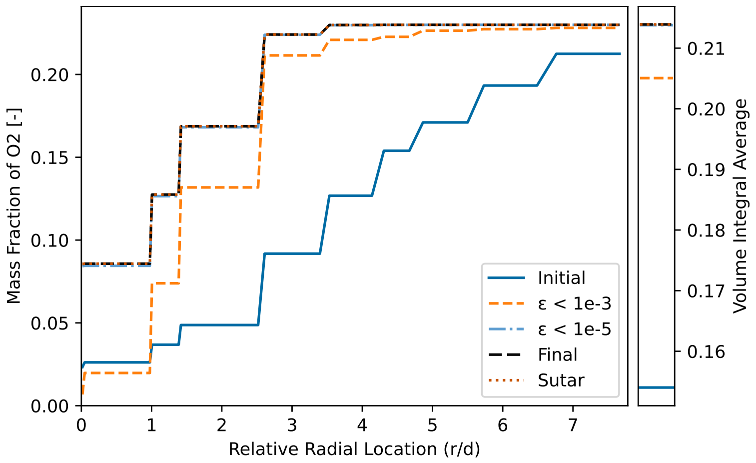

Figure A.6: Radial plot of Y_{O_2} at axial location x/d = 45 for a 1000 reactor CRN, with the initial CRN state (the solid blue line), CRN state at $\varepsilon < 10^{-3}$ (short orange dashes), CRN state at $\varepsilon < 10^{-5}$ (light blue dash-dotted line), final CRN state (long black dashes), and final result from Sutar [21] (dotted red line).

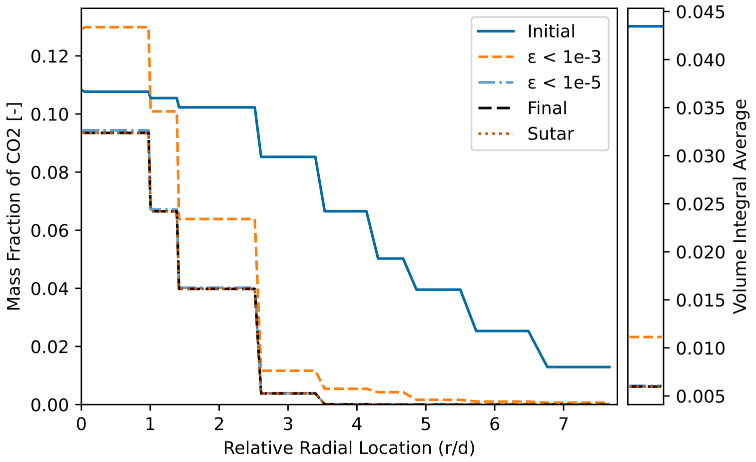

Figure A.7: Radial plot of Y_{CO_2} at axial location x/d = 45 for a 1000 reactor CRN, with the initial CRN state (the solid blue line), CRN state at $\varepsilon < 10^{-3}$ (short orange dashes), CRN state at $\varepsilon < 10^{-5}$ (light blue dash-dotted line), final CRN state (long black dashes), and final result from Sutar [21] (dotted red line).

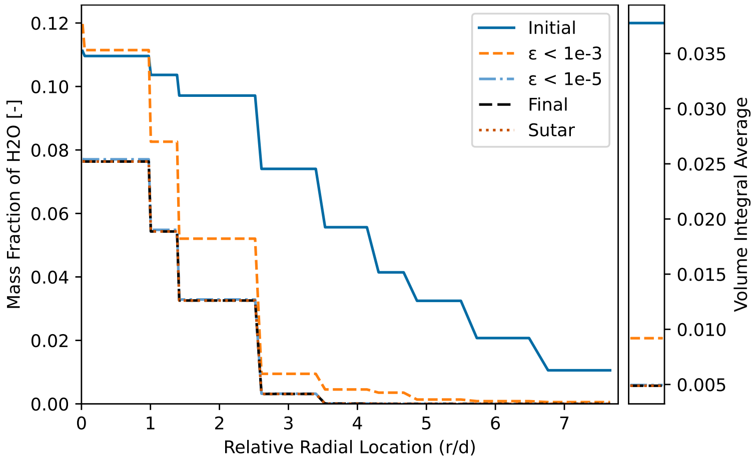

Figure A.8: Radial plot of Y_{H_2O} at axial location x/d = 45 for a 1000 reactor CRN, with the initial CRN state (the solid blue line), CRN state at $\varepsilon < 10^{-3}$ (short orange dashes), CRN state at $\varepsilon < 10^{-5}$ (light blue dash-dotted line), final CRN state (long black dashes), and final result from Sutar [21] (dotted red line).

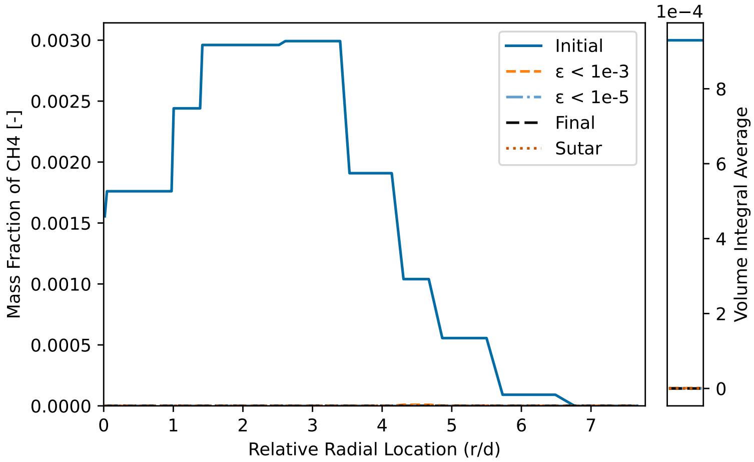

Figure A.9: Radial plot of Y_{CH_4} at axial location x/d = 45 for a 1000 reactor CRN, with the initial CRN state (the solid blue line), CRN state at $\varepsilon < 10^{-3}$ (short orange dashes), CRN state at $\varepsilon < 10^{-5}$ (light blue dash-dotted line), final CRN state (long black dashes), and final result from Sutar [21] (dotted red line).

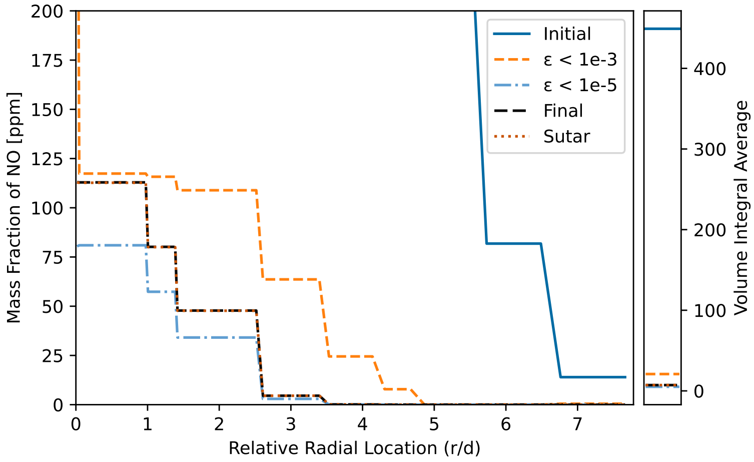

Figure A.10: Radial plot of Y_{NO} at axial location x/d = 45 for a 1000 reactor CRN, with the initial CRN state (the solid blue line), CRN state at $\varepsilon < 10^{-3}$ (short orange dashes), CRN state at $\varepsilon < 10^{-5}$ (light blue dash-dotted line), final CRN state (long black dashes), and final result from Sutar [21] (dotted red line).

A.3. Axial location x/d = 60

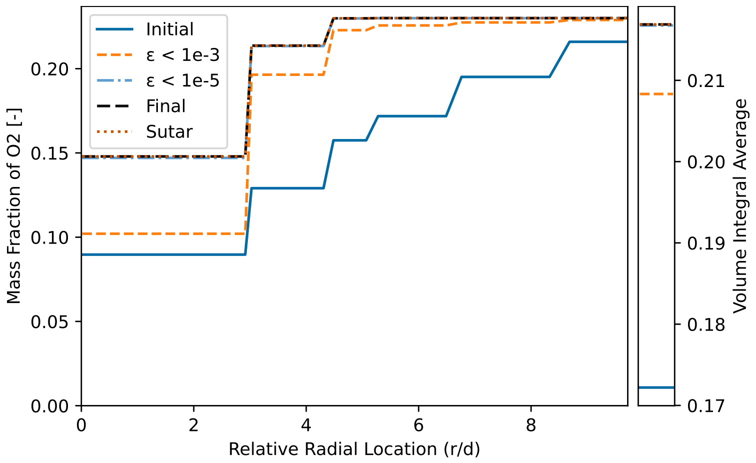

Figure A.11: Radial plot of Y_{O_2} at axial location x/d = 60 for a 1000 reactor CRN, with the initial CRN state (the solid blue line), CRN state at $\varepsilon < 10^{-3}$ (short orange dashes), CRN state at $\varepsilon < 10^{-5}$ (light blue dash-dotted line), final CRN state (long black dashes), and final result from Sutar [21] (dotted red line).

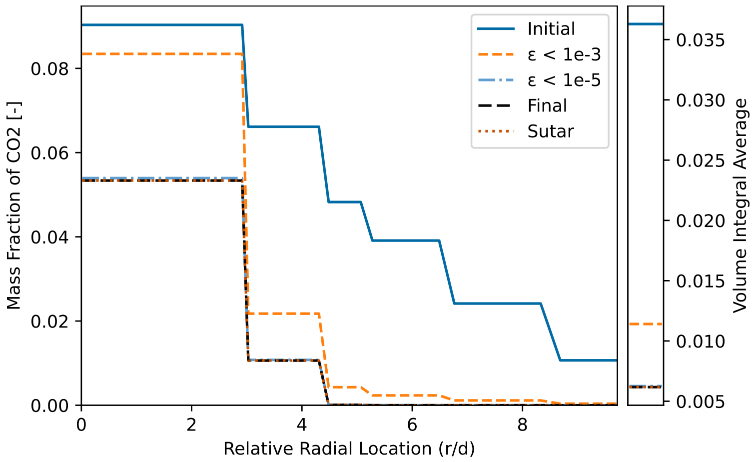

Figure A.12: Radial plot of Y_{CO_2} at axial location x/d = 60 for a 1000 reactor CRN, with the initial CRN state (the solid blue line), CRN state at $\varepsilon < 10^{-3}$ (short orange dashes), CRN state at $\varepsilon < 10^{-5}$ (light blue dash-dotted line), final CRN state (long black dashes), and final result from Sutar [21] (dotted red line).

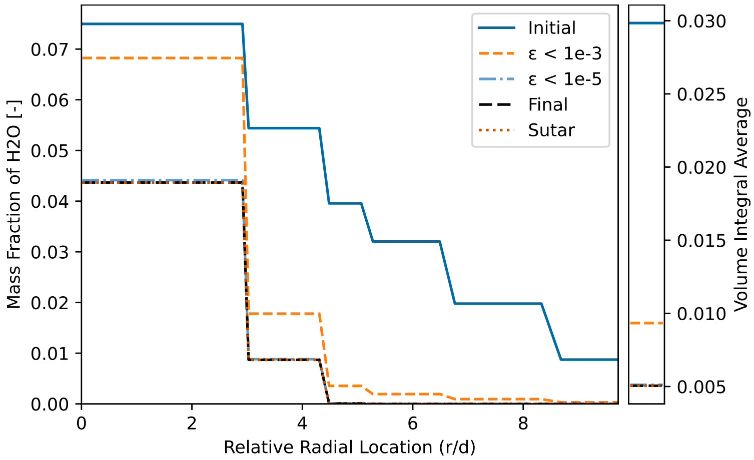

Figure A.13: Radial plot of Y_{H_2O} at axial location x/d = 60 for a 1000 reactor CRN, with the initial CRN state (the solid blue line), CRN state at $\varepsilon < 10^{-3}$ (short orange dashes), CRN state at $\varepsilon < 10^{-5}$ (light blue dash-dotted line), final CRN state (long black dashes), and final result from Sutar [21] (dotted red line).

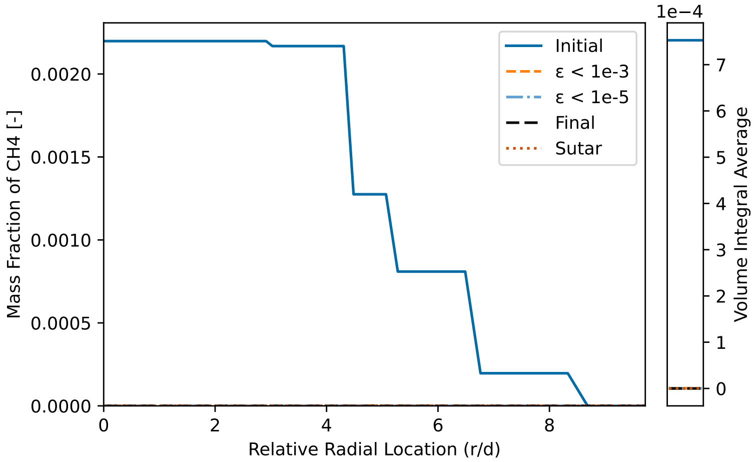

Figure A.14: Radial plot of Y_{CH_4} at axial location x/d = 60 for a 1000 reactor CRN, with the initial CRN state (the solid blue line), CRN state at $\varepsilon < 10^{-3}$ (short orange dashes), CRN state at $\varepsilon < 10^{-5}$ (light blue dash-dotted line), final CRN state (long black dashes), and final result from Sutar [21] (dotted red line).

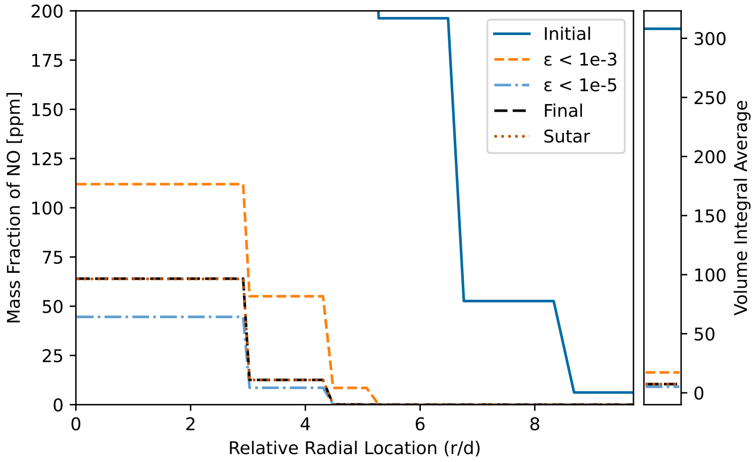

Figure A.15: Radial plot of Y_{NO} at axial location x/d = 60 for a 1000 reactor CRN, with the initial CRN state (the solid blue line), CRN state at $\varepsilon < 10^{-3}$ (short orange dashes), CRN state at $\varepsilon < 10^{-5}$ (light blue dash-dotted line), final CRN state (long black dashes), and final result from Sutar [21] (dotted red line).

B

Supplemental Plots Baseline Case

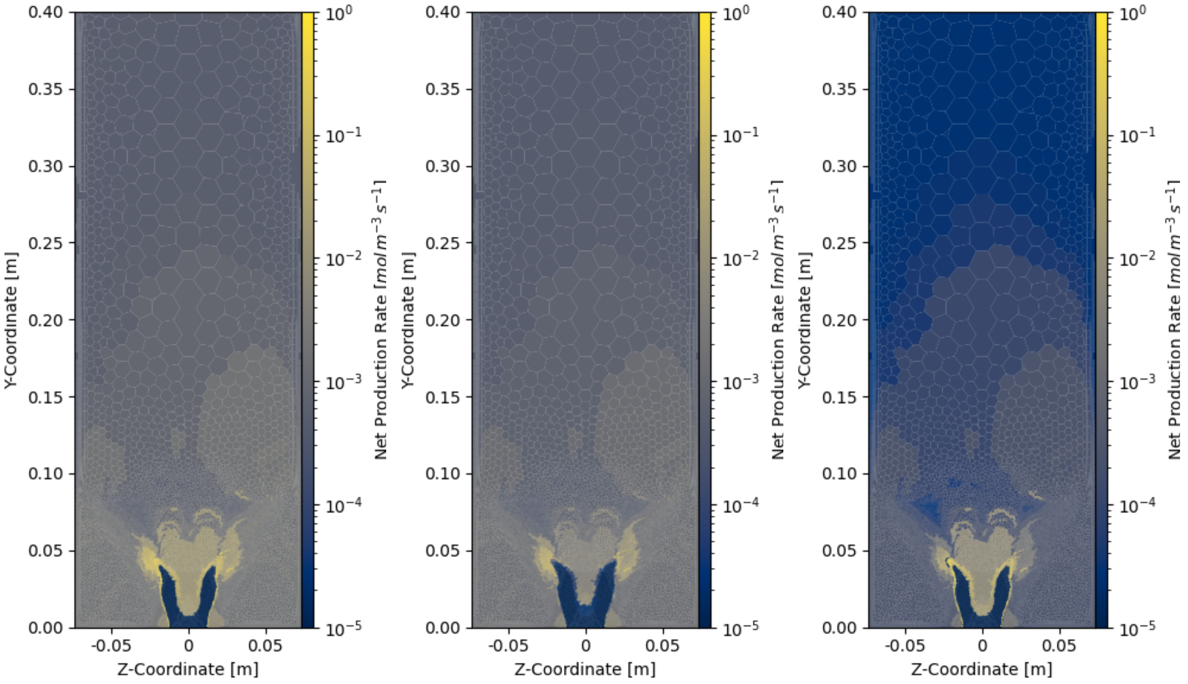

(a) Total **(b)** Thermal **(c)** Prompt

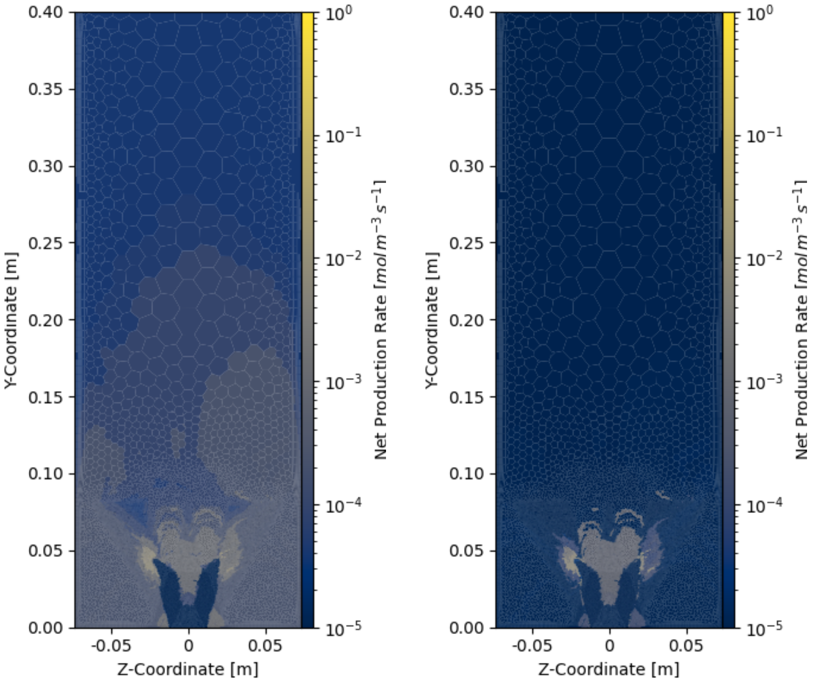

(d) N_2O **(e)** NNH

Figure B.1: Net production rates of total NO and its various pathways parallel to the symmetry plane at x=$1\ \mathrm{mm}$ for a 2000 reactor CRN using *clustering II*.

C

Supplemental Plots Sensitivity Study

C.1. Temperature Sensitivity

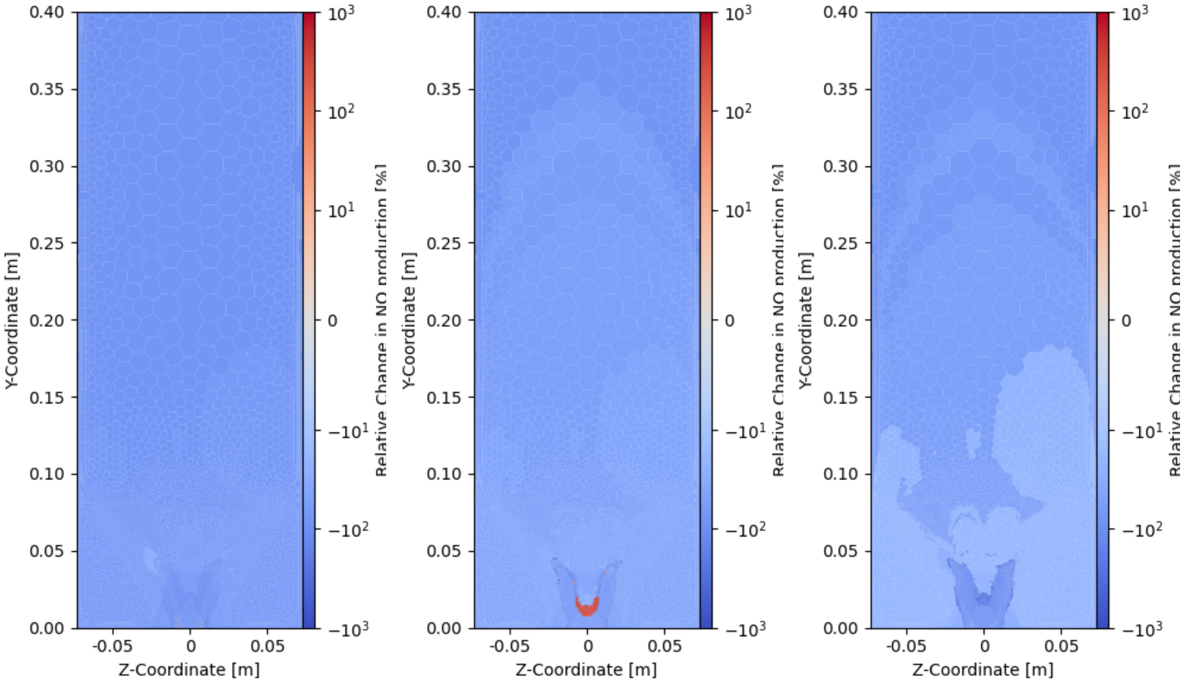

(a) Thermal, T = 95% **(b)** Prompt, T = 95% **(c)** N_2O, T = 95%

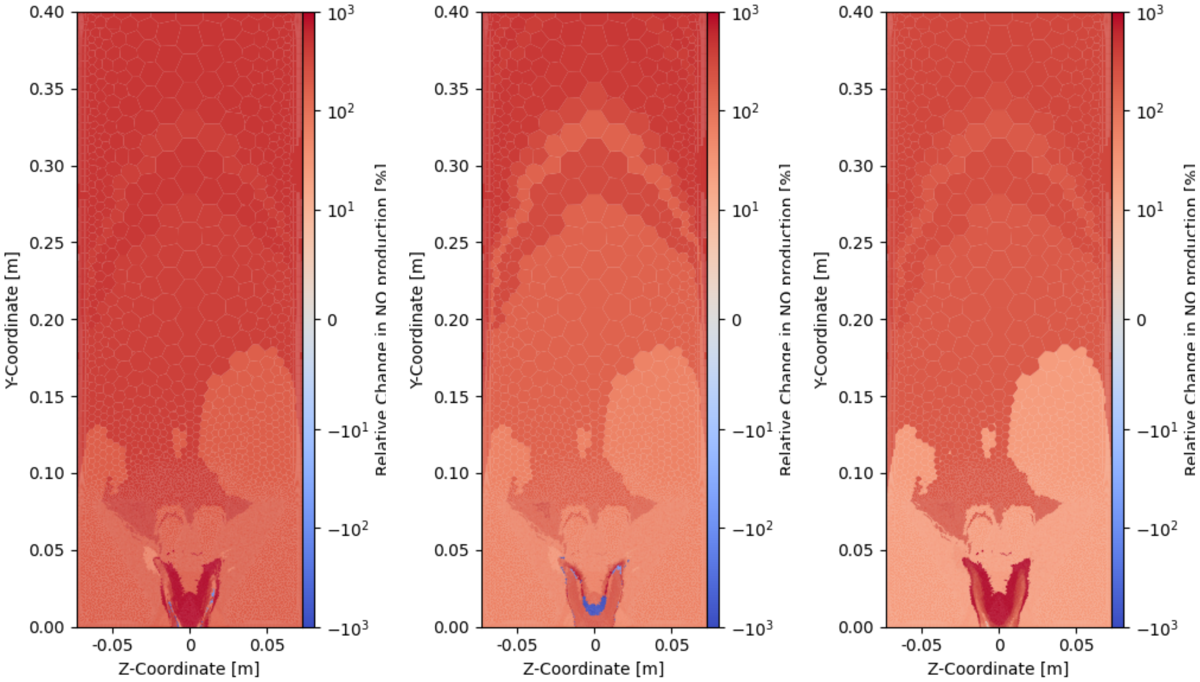

(d) Thermal, T = 105% **(e)** Prompt, T = 105% **(f)** N_2O, T = 105%

Figure C.1: Relative change of the NO pathways for changing temperature parallel to the symmetry plane at x=$1\,\mathrm{mm}$ for a *clustering II*, 1000 reactor CRN.

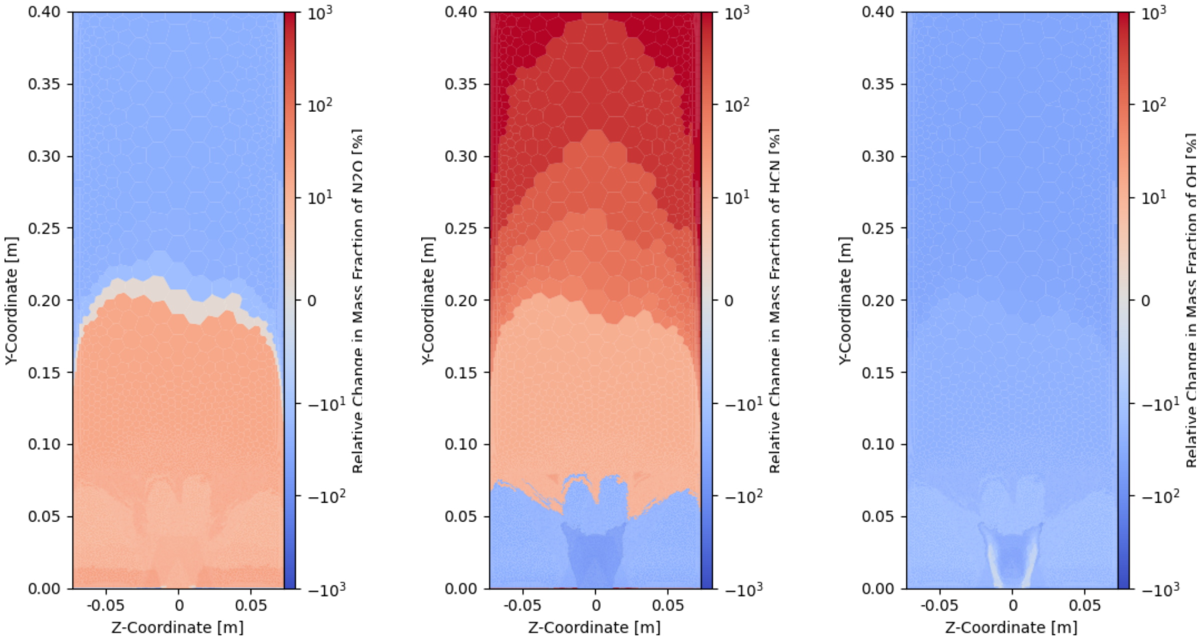

(a) 95% Temperature **(c)** 95% Temperature **(e)** 95% Temperature

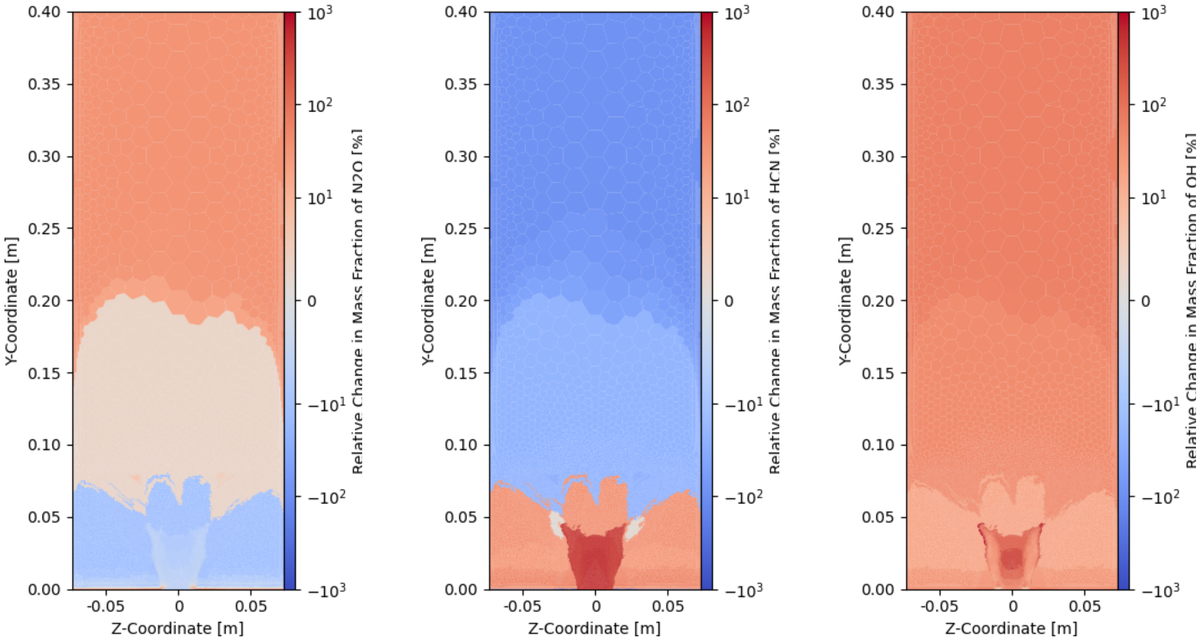

(b) 105% Temperature **(d)** 105% Temperature **(f)** 105% Temperature

Figure C.2: Figures (a) and (b) show the relative change in Y_{N_2O}. Figures (c) and (d) show the relative change in Y_{HCN}. Figures (e) and (f) show the relative change in Y_{OH}.

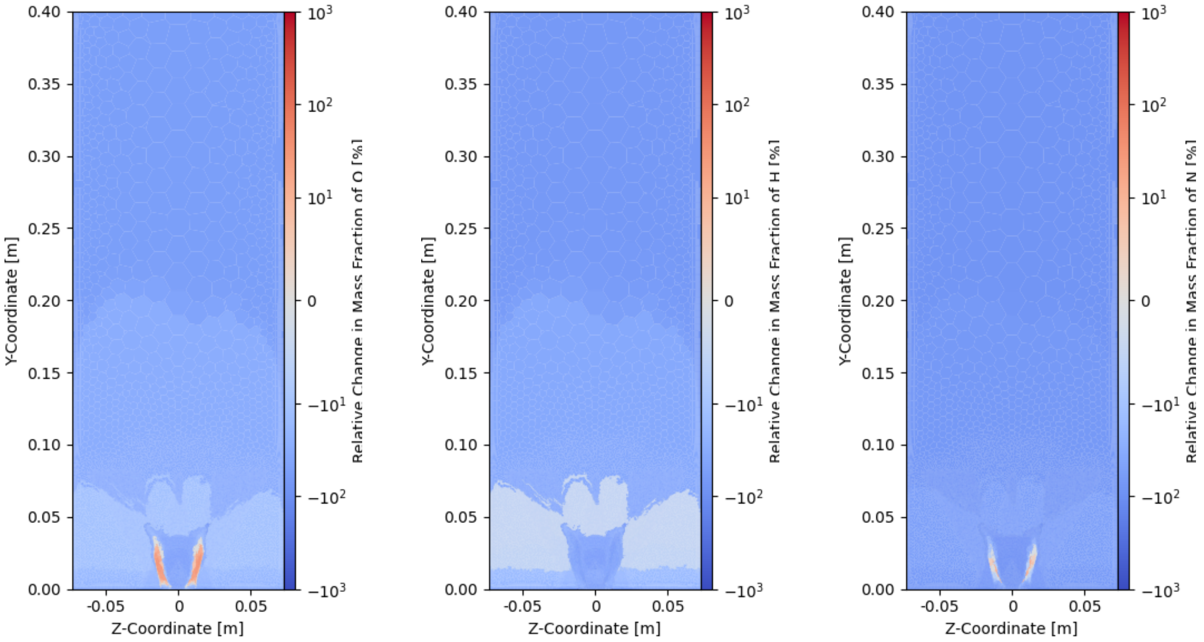

(a) 95% Temperature **(c)** 95% Temperature **(e)** 95% Temperature

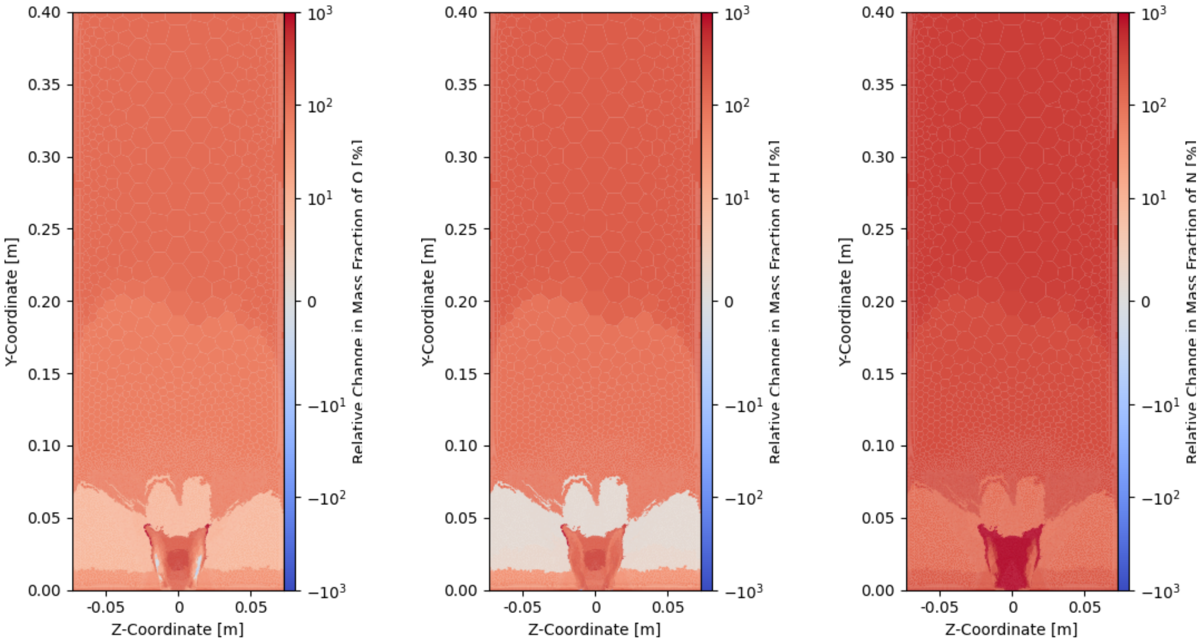

(b) 105% Temperature **(d)** 105% Temperature **(f)** 105% Temperature

Figure C.3: Figures (a) and (b) show the relative change in Y_O. Figures (c) and (d) show the relative change in Y_H. Figures (e) and (f) show the relative change in Y_N.

C.2. Density Sensitivity

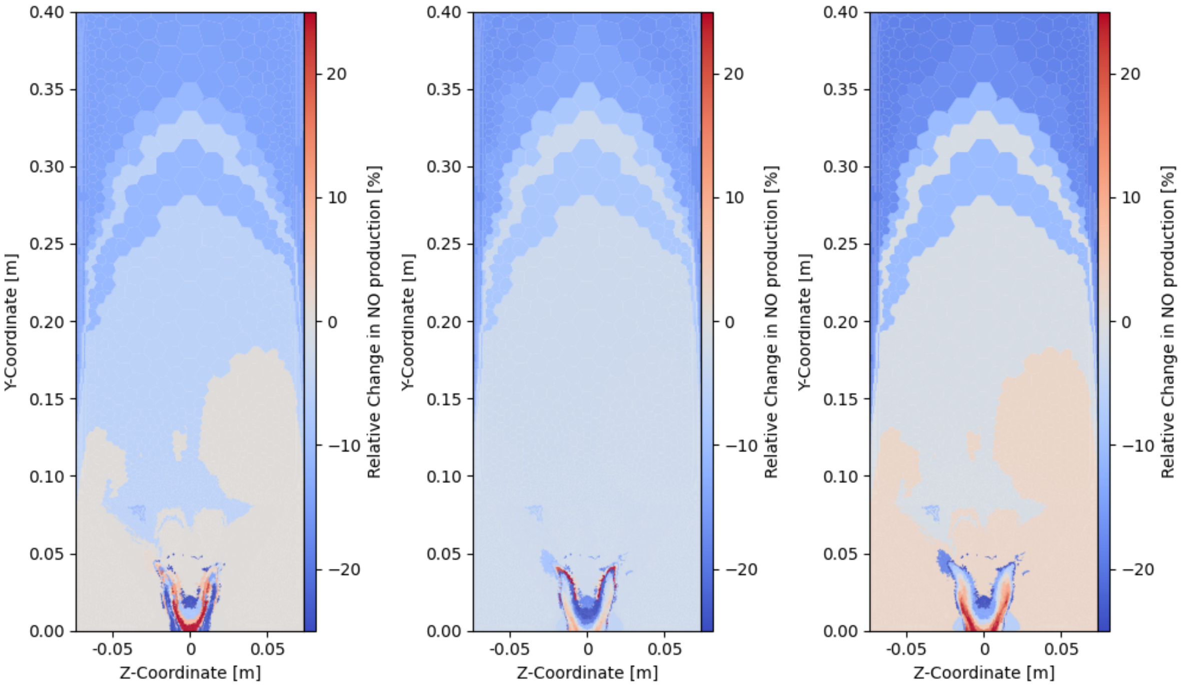

(a) Thermal, ρ = 90% **(b)** Prompt, ρ = 90% **(c)** N_2O, ρ = 90%

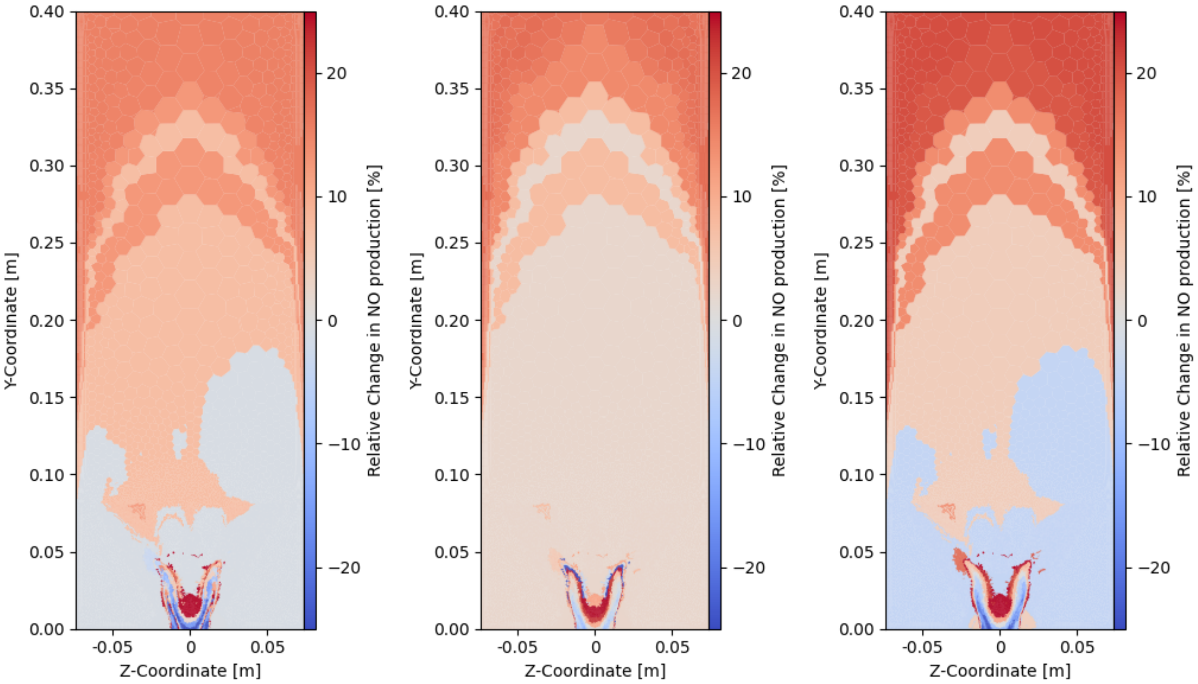

(d) Thermal, ρ = 110% **(e)** Prompt, ρ = 110% **(f)** N_2O, ρ = 110%

Figure C.4: Relative change of the NO pathways for changing density parallel to the symmetry plane at x=$1\,\mathrm{mm}$ for a *clustering II*, 1000 reactor CRN.

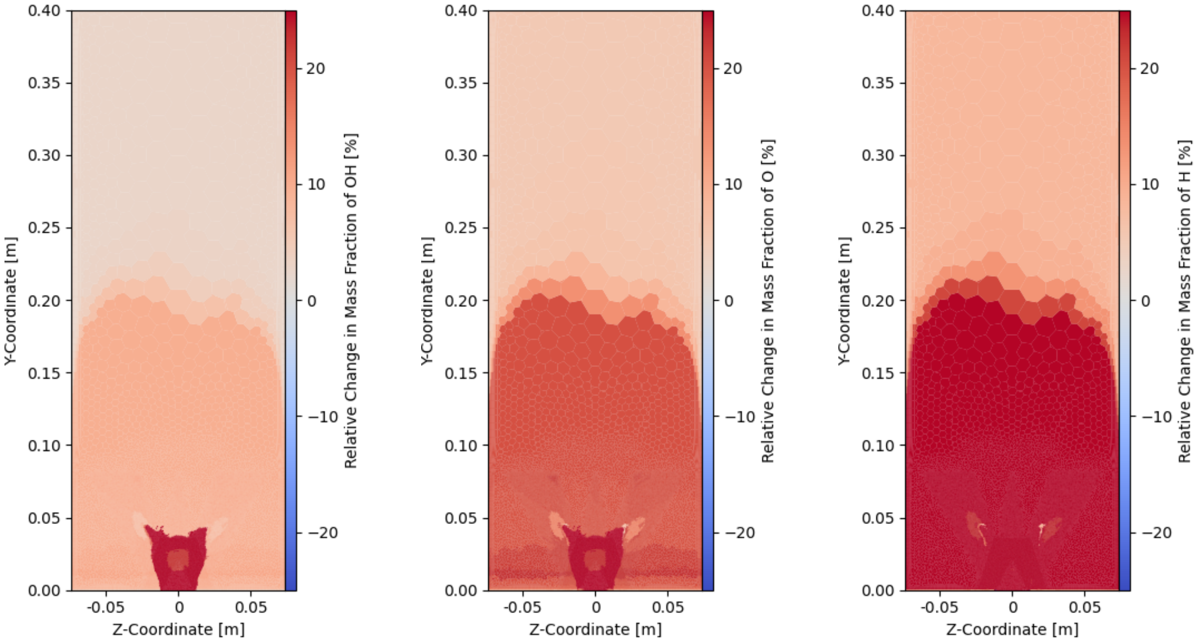

(a) 90% Density **(c)** 90% Density **(e)** 90% Density

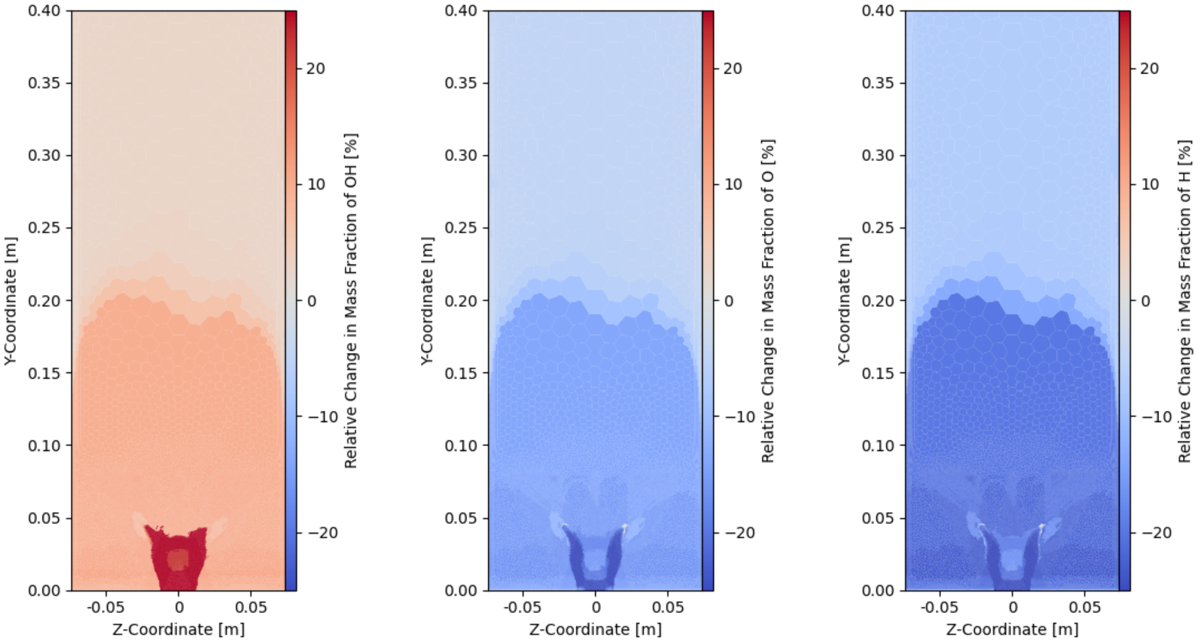

(b) 110% Density **(d)** 110% Density **(f)** 110% Density

Figure C.5: Figures (a) and (b) show the relative change in Y_{OH}. Figures (c) and (d) show the relative change in Y_O. Figures (e) and (f) show the relative change in Y_H.

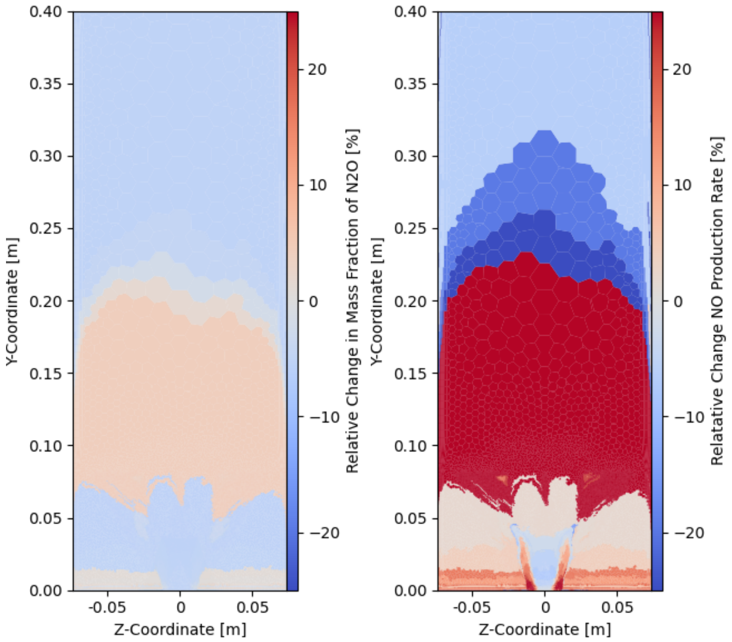

(a) 90% Density **(c)** 90% Density

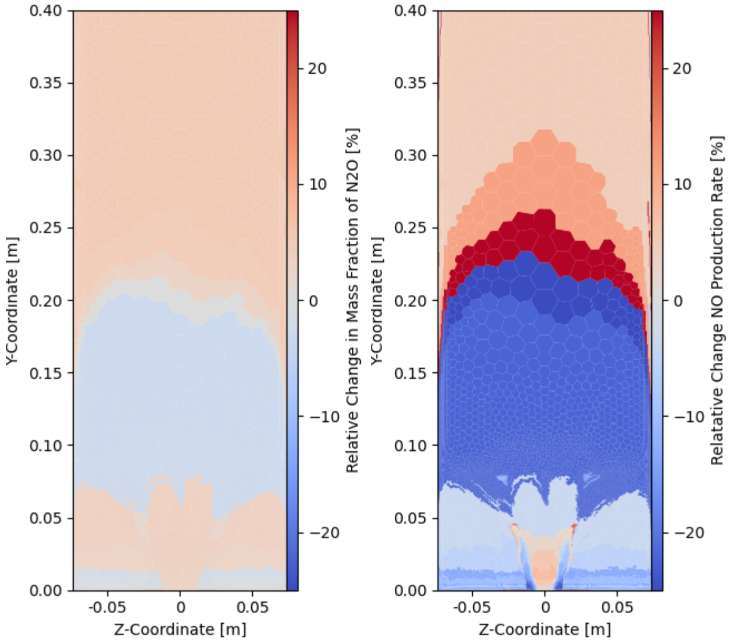

(b) 110% Density **(d)** 110% Density

Figure C.6: Figures (a) and (b) show the relative change in Y_{N_2O}. Figures (c) and (d) show the relative change in the production rate of H + N2O ↔ N2 + OH.

C.3. Equivalence Sensitivity

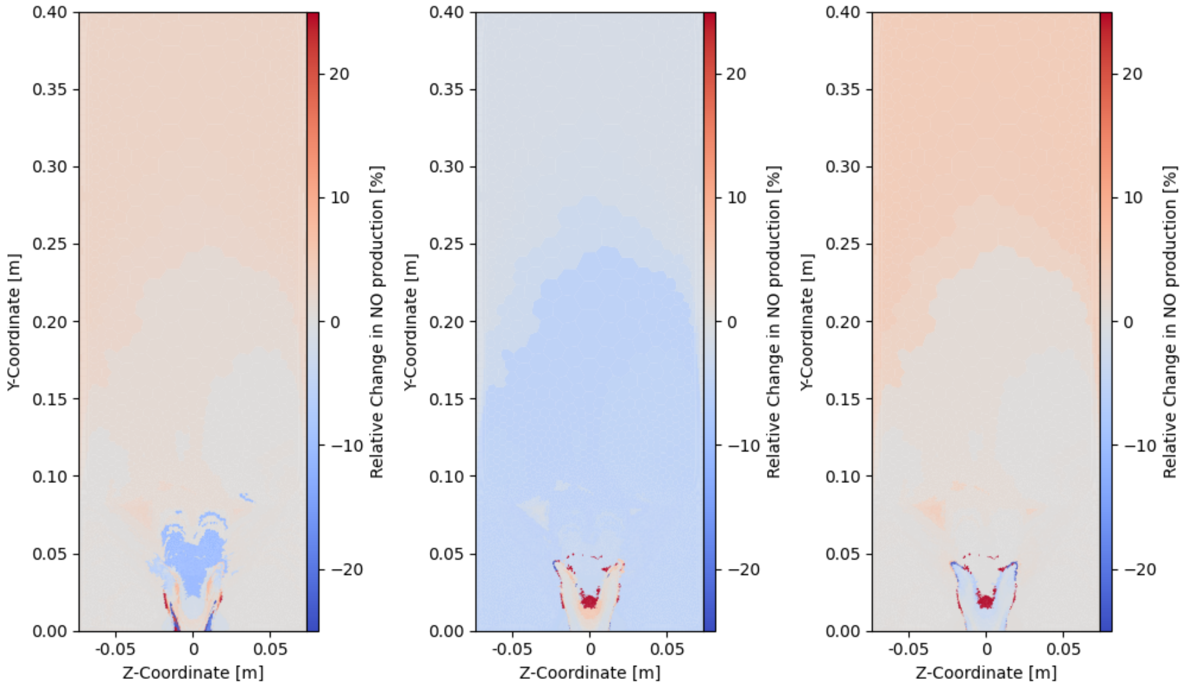

(a) Thermal, φ = 0.68 **(b)** Prompt, φ = 0.68 **(c)** N_2O, φ = 0.68

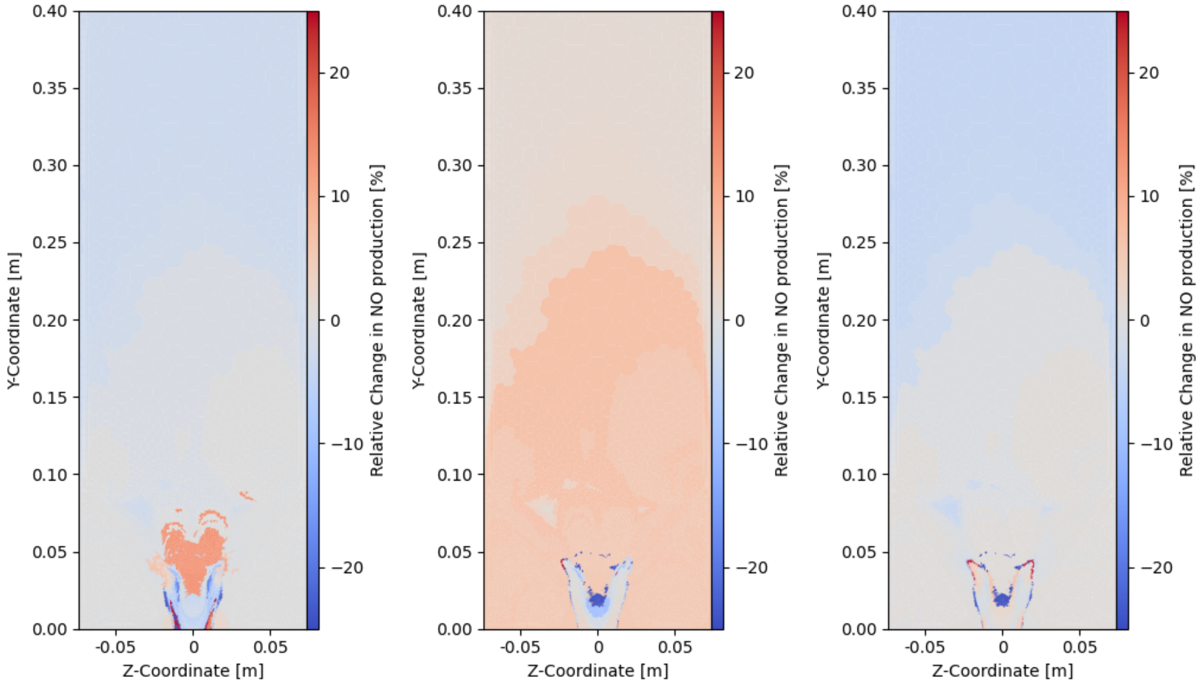

(d) Thermal, φ = 0.76 **(e)** Prompt, φ = 0.76 **(f)** N_2O, φ = 0.76

Figure C.7: Relative change of the NO pathways for changing equivalence ratio, parallel to the symmetry plane at x=$1\,\mathrm{mm}$ for a *clustering II*, 2000 reactor CRN.

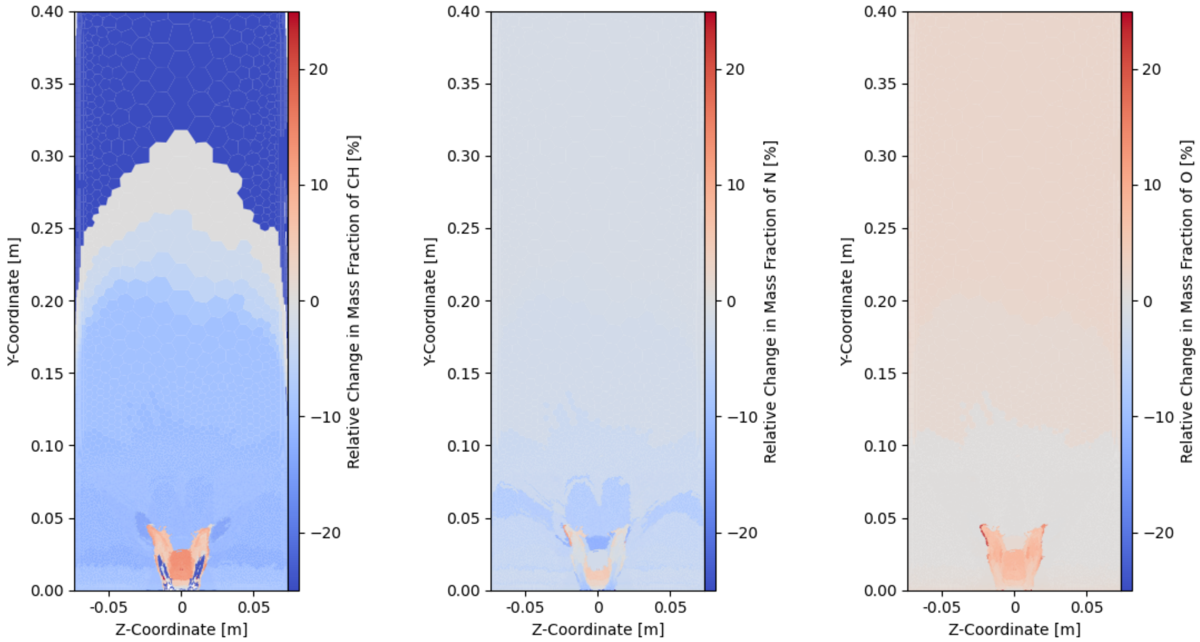

(a) $\varphi = 0.68$ **(c)** $\varphi = 0.68$ **(e)** $\varphi = 0.68$

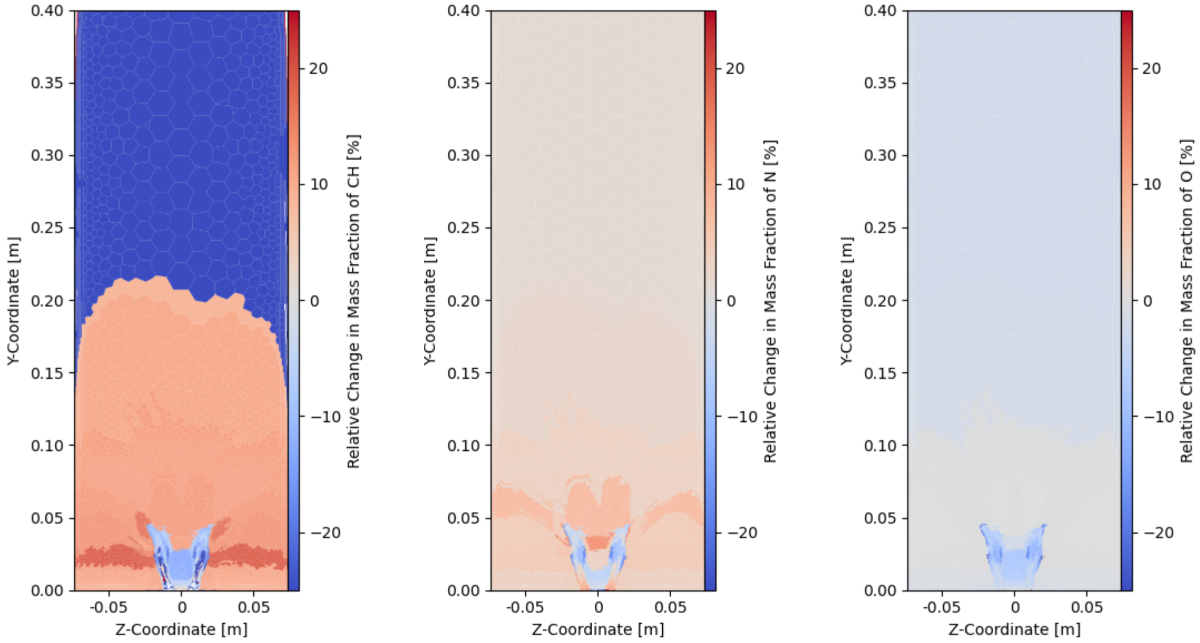

(b) $\varphi = 0.76$ **(d)** $\varphi = 0.76$ **(f)** $\varphi = 0.76$

Figure C.8: Figures (a) and (b) show the relative change in Y_{CH}. Figures (c) and (d) show the relative change in Y_N. Figures (e) and (f) show the relative change in Y_O.

C.4. Introduction of Hydrogen

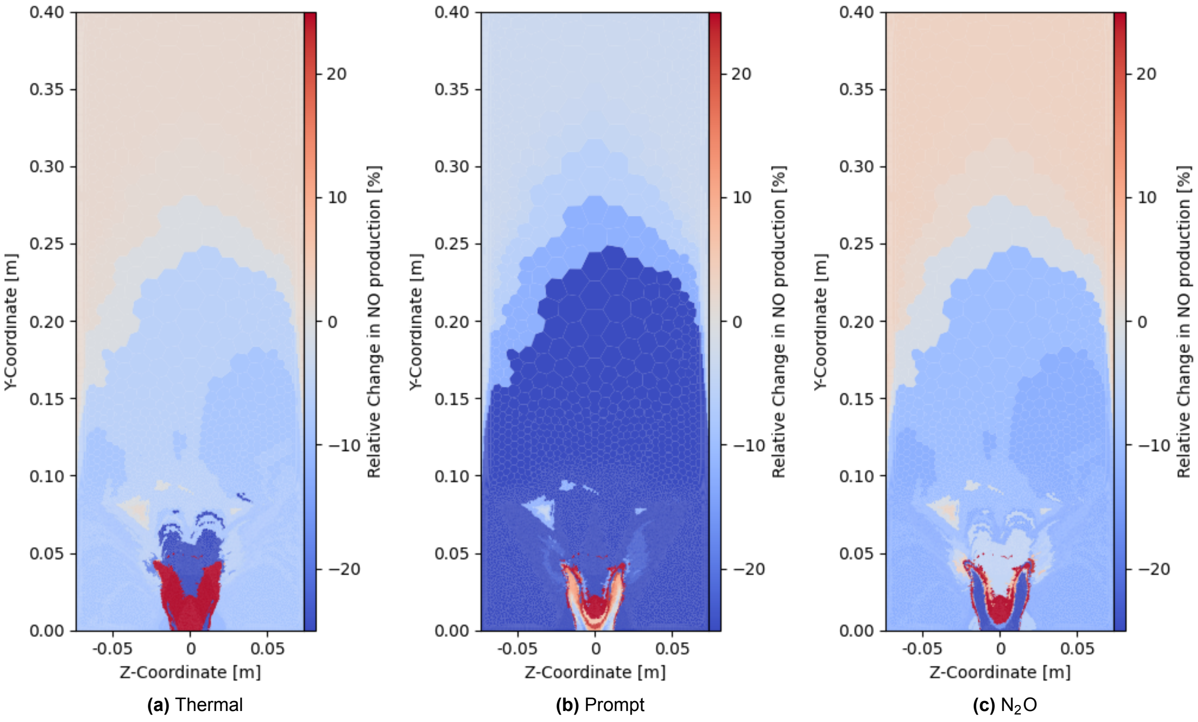

(a) Thermal **(b)** Prompt **(c)** N_2O

Figure C.9: Relative change of the NO pathways for $X_{H_2} = 0.25$ parallel to the symmetry plane at x=$1\,\mathrm{mm}$ for a *clustering II*, 2000 reactor CRN.

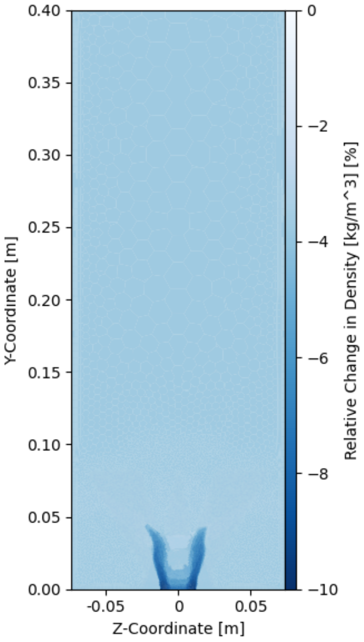

Figure C.10: Decrease in density for $X_{H_2} = 0.8$

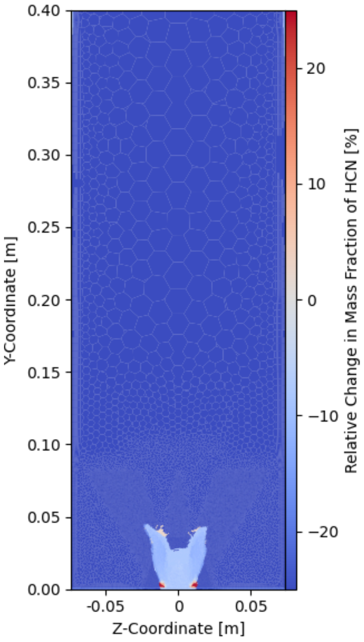

Figure C.11: Change in Y_{HCN} $X_{H_2} = 0.25$

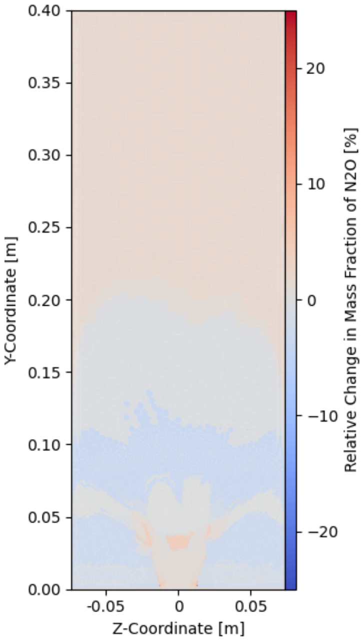

Figure C.12: Change in Y_{N_2O} $X_{H_2} = 0.25$

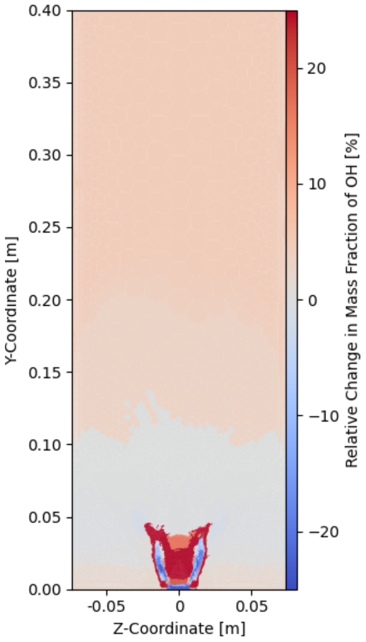

Figure C.13: Change in Y_{OH} $X_{H_2} = 0.25$

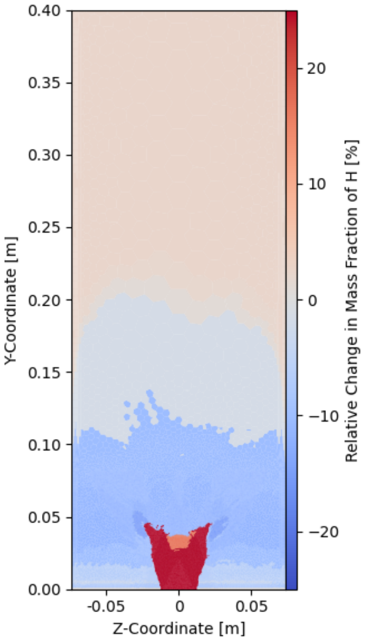

Figure C.14: Change in Y_H $X_{H_2} = 0.25$

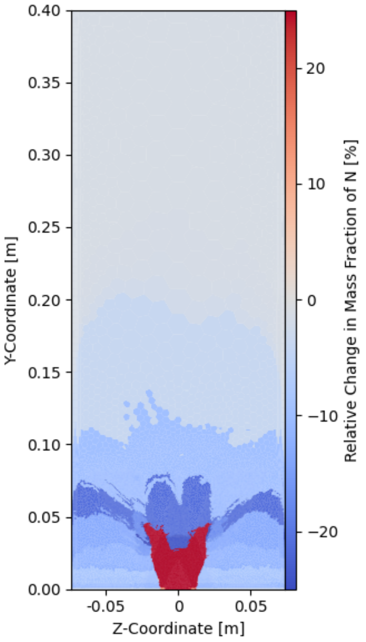

Figure C.15: Change in Y_N $X_{H_2} = 0.25$

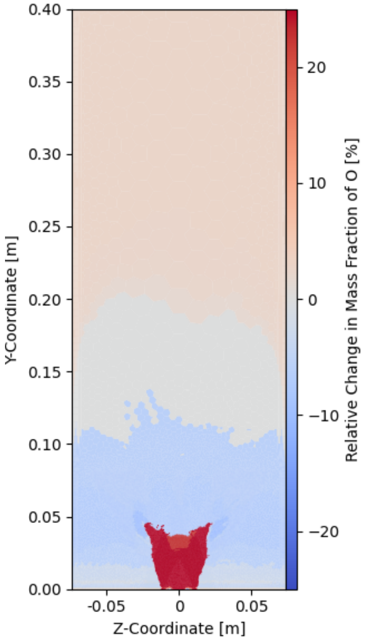

Figure C.16: Change in Y_O $X_{H_2} = 0.25$